NTNU

Norwegian University of
Science and Technology

Nonlinear Adaptive Motion Controllers for Ships: Model-Scale Experiments in an Ocean Basin

Tore Egil Sæterdal

Master of Science in Cybernetics and Robotics
Submission date: June 2018
Supervisor: Morten Breivik, ITK
Co-supervisor: Mikkel Eske Nørgaard Sørensen, ITK

Norwegian University of Science and Technology
Department of Engineering Cybernetics

"Top-heavy was the ship as a dinnerless student with all Aristotle in his head."
-Herman Melville,
Moby-Dick; or, The Whale,
1851.

Preface

This thesis is written as part of a M.Sc degree in Cybernetics and Robotics at the Norwegian University of Science and Technology (NTNU). I would like to thank my supervisor Morten Breivik for inspiration in understanding the considered problem, and for giving valuable feedback on my work. I also extend much gratitude to my co-supervisor Mikkel Eske Nørgaard Sørensen for all the provided help in understanding the concepts, as well as intuition in debugging the many unintelligible errors I encountered during implementation of the systems. Gratitude is also expressed toward Senior Engineer Torgeir Wahl with NTNU's Department of Marine Technology for valuable knowledge and help regarding the Marine Cybernetics Laboratory (MC-lab) and quirks in the equipment when doing the laboratory experiments. I also thank Ole Nikolai Lyngstadaas for great cooperation the last year, in long days in the lab and analyzing experiment data, as well as publishing a research paper, the latter I did not expect I would do when I started my education. I thank Omega Loftet for providing much needed refuge when my studies proved to be difficult and cumbersome. Lastly, I would like to thank my parents for support and encouragement during my education.

The thesis is inspired by an ongoing effort to investigate adaptive methods for autonomous control of ships, a topic that has gained interest in recent years. The considered problem is a continuation of research by my supervisors. Throughout the progress of the work in this thesis, my supervisors have provided feedback on results, thoughts and ideas on structure, problem scope, results and implementations, through bi-weekly meetings. Mikkel also assisted in the laboratory experiments at the MC-lab.

Furthermore, this thesis is a continuation of the project work done in the Fall of 2017, where I investigated a series of adaptive methods, in order to gain a better understanding of the concept and to find promising methods to develop further in this master thesis. The first 4 weeks of the thesis period was spent co-authoring a research paper with Ole Nikolai Lyngstadaas and my supervisors based on the results from the project work, which was approved for submission to CCTA 2018, the 2nd IEEE Conference on Control Technology and Applications in Copenhagen, August 2018 [1]. Final updates to the paper were done in May 2018 before final submission. The research paper investigates effects of using a magnitude-rate saturation model on a ship, which later was used as an actuator handling method in this thesis.

Two laboratory weeks were booked for the thesis period, for validation of implementations through testing in an ocean basin. The numerical model of the considered scale ship was provided from an earlier master thesis by Jon Bjørnø [2]. However, as discovered early in the progress, this model was not as accurate as desired for the control purposes in this thesis. Together with Ole [3], further model identification was done in order to achieve

optimal conditions, both before the first lab session and further updates after, thus going beyond the initial scope of the project. One of the key goals was to identify the thrust capabilities of the scale model, to which the earlier documentation fell short. Furthermore, together with Ole and my supervisors, redesigning, rewriting and testing of the velocity estimator provided was done between the two lab sessions, in April. These findings are discussed in Chapter 4. The work spent on model identification and velocity estimator redesign and testing outside of the designated lab weeks gave a deeper knowledge of the ship dynamics and lab setup, which I found interesting.

A workstation and equipment for simulation and writing was provided by the Department of Engineering Cybernetics. The Department of Marine Technology provided access to an ocean basin and a scale model ship at the MC-lab.

Summary

This thesis investigates two different methods of adaptive control to be used for ship motion control, namely $\mathcal{L}_1$ adaptive control and Immersion and Invariance adaptive control. The adaptive concepts is used to extend an existing cascaded non-linear feedback control structure. The resulting adaptive control methods are implemented for a 3-DOF ship model and then tested in an purpose-designed simulator and scale model conditions in the ocean basin at Marine Cybernetics lab (MC-lab) at the Norwegian University of Science and Technology (NTNU) in Trondheim. Since adaptive methods tend to be more aggressive in control input, a magnitude-rate saturation model and a command governor, two different methods of actuator handling are used to limit this effect and thus reduce energy consumption and actuator wear & tear.

Due to problems with the positioning system at MC-lab discovered during the thesis work, a modified velocity estimator was designed, tested and implemented to provide better feedback signals in the experiments. This improved the adaptive control greatly, as the control input is less affected by noise. Further, model identification of the scale model ship was performed between the two lab sessions in order to improve performance.

The experiments and simulations of the adaptive controllers are evaluated using a set of performance metrics that give an objective measure of comparison in terms of control error, energy efficiency and wear & tear, and the adaptive controllers are compared with the nominal controller that they are extended from. The yielded results are promising, as the adaptive controllers prove to reduce control errors and improve reference tracking of the ship model, both in simulations and in laboratory experiments. Expecially the $\mathcal{L}_1$ adaptive control provides improvement of performance in both simulations and experiments. The Immersion and Invariance adaptive control showed promising results in simulations, but the performance was not as good in laboratory testing. The drawback of the adaptive methods is increased energy consumption and actuator wear & tear, as there is a trade-off between accurate tracking and low energy consumption.

It is shown that the actuator handling methods manage to increase energy efficiency and reduce actuator wear & tear, without much increase in control errors. Especially the command governor structure greatly improved reference tracking and energy efficiency in model scale experiments, but at the cost of longer run-time.

Sammendrag

Denne masteroppgaven undersøker to forskjellige metoder for adaptiv kontroll som skal brukes til autonom styring av skip, spesifikt $\mathcal{L}_1$ adaptiv kontroll og Immersion og Invariance adaptiv kontroll. De adaptive konseptene brukes til å utvide en eksisterende kaskadet, ulineær tilbakekoblings-kontroller. De resulterende adaptive kontrollmetodene tilpasses for en 3-DOF skipsmodell og testes deretter med en formåls-designet simulator og under skala-forhold i havbassenget ved Marine Cybernetics lab (MC-lab) ved Norges teknisk-naturvitenskapelige universitet (NTNU) i Trondheim. Siden adaptive metoder har en tendens til å være mer aggressive i beregnet kontrollpådrag, brukes to forskjellige metoder for aktuatorhåndtering for å begrense denne effekten og dermed redusere energiforbruket og aktuatorens slitasje. De testede metodene for aktuatorhåndtering er MRS [1] og Command Governor.

På grunn av problemer med posisjoneringssystemet på MC-lab som ble oppdaget underveis i oppgaven, ble en modifisert hastighetsestimator designet, testet og implementert for å gi bedre tilbakekoblingssignaler i forsøkene. Dette forbedret den adaptive kontrollen meget, da kontrollpådragene ble mindre påvirket av støy. Videre utføres modell-identifikasjon av modellskipet mellom laboratorieøktene for å få en med riktig modell og dermed forbedret ytelse.

Forsøkene og simuleringene av de adaptive regulatorene blir evaluert ved hjelp av et sett av ytelsesstatistikker (eng: performance metrics) som gir et objektivt grunnlag for sammenligning med hensyn til kontrollfeil, energieffektivitet og slitasje, og de adaptive regulatorene sammenlignes med den nominelle kontrolleren som de er utvidet fra. Resultatene er lovende, da de adaptive kontrollerne viser seg å redusere kontrollfeil og forbedre referanseføling for skipmodellen, både i simuleringer og i laboratorieeksperimenter. Spesielt $\mathcal{L}_1$ adaptiv kontroll gir forbedring av ytelse i både simuleringer og eksperimenter. Immersion & Invariance-adaptiv kontroll viser lovende resultater i simuleringer, men ytelsen var ikke så god i laboratorietester. Ulempen med de adaptive metodene er økt energiforbruk og aktuatorslitasje, da det er en avveining som må tas mellom nøyaktig følging og lavt energiforbruk.

Det er vist at teknikkene for aktuatorhåndtering klarer å øke energieffektiviteten og redusere slitasjen på aktuatorene, uten mye økning i kontrollfeil. Spesielt Command Governor gir forbedret referanseføling og energieffektivitet i eksperimenter, men på bekostning av lengre kjøretid.

Table of Contents

List of Tables

List of Figures

Abbreviations

CG	=	Command Governor
DOF	=	Degrees Of Freedom
CSAD	=	C/S Inocean Cat I Drillship
NP-NV	=	Nonlinear pose, nonlinear velocity feedback
$\mathcal{L}_1$	=	$\mathcal{L}_1$ adaptive control fitted on a cascaded nonlinear feedback controller (NP-NV)
I&I	=	Immersion and Invariance adaptive control fitted on a cascaded nonlinear feedback controller (NP-NV)
MRS	=	Magnitude-Rate Saturation model for augmenting control input to an autonomous vessel

Chapter 1

Introduction

1.1 Motivation

Automated motion control of ships has been a topic of extensive research for several decades. In moving from simple course-keeping assistant systems on traditional manned vessels, to fully automated unmanned autonomous vessels, the need for more efficient and sophisticated control systems has grown. In recent years, the research has expanded from control of manned vessels to also include unmanned vessels. Challenges include handling uncertain nonlinear hydrodynamics and external disturbances, since the ocean is an unreliable environment with nonlinearities and unpredictable perturbations. Hence, it is important to develop adaptive and robust control algorithms, which can deal with these internal uncertainties and external disturbances in a realistic and energy efficient manner. It is also important to consider physical magnitude and rate saturation constraints for the actuators.

1.2 Problem Formulation

This thesis will focus on two state-of-the-art adaptive control technologies that has been proposed in the later years, and adapt them to a 3-DOF ship model. The adaptive concepts will be used to enhance the performance of an existing cascaded nonlinear feedback controller proposed in [7], by compensating for the uncertainties inherent in the ship model and control disturbances. The thesis will also look into how actuator handling methods can be used in cooperation with adaptive means, to ensure feasible control input and limit actuator wear. More specifically, the work in this thesis shall:

- Investigate $\mathcal{L}_1$ adaptive control as an adaptive concept to use with a nonlinear cascaded feedback controller for motion control of a ship.

- Investigate Immersion and Invariance adaptive control as an adaptive concept to use with a nonlinear cascaded feedback controller for motion control of a ship.
- Investigate methods of actuator handling with the aim of reducing energy consumption and wear & tear of adaptive control.
- Develop a simulator that approximates real conditions with noise and uncertainties, for testing and verification of control schemes.
- Test the implemented adaptive control techniques in laboratory experiments in an ocean basin to verify the adaptive controllers with model-scale conditions.
- Evaluate and compare controllers using a set of different performance metrics.

1.3 Literature Overview

1.3.1 $\mathcal{L}_1$ Adaptive Control

The term $\mathcal{L}_1$ Adaptive control was coined and the underlying adaptive control concept was first developed by Chengyu Cao and Naira Hovakimyan [8]-[9]. The name originates from the concept of the $\mathcal{L}_1$ norm needed to prove stability of the control law. One of the key features of this control concept compared to other adaptive approaches is the decoupling of the adaptation loop and the control loop, allowing fast adaptation.

The high-gain $\mathcal{L}_1$ adaptive approach was proposed as a way to address the inherent uncertainties that is present in most dynamic models. The fast adaptation property has previously been utilized for vessels in marine applications, such as a high-speed personal watercraft (PWC) in [10] where the $\mathcal{L}_1$ was used in design of an adaptive autopilot that guaranteed robustness and closed-loop system stability. In [11], the $\mathcal{L}_1$ adaptive control concept is implemented as a method to deal with model uncertainties in a ship path-following problem, providing improved transient and target tracking. The $\mathcal{L}_1$ adaptation has also been utilized for aerial applications, where in [12], the adaptive scheme is used as part of a re-configurable flight controller on an unstable multiple-input multiple-output (MIMO), unmanned aircraft subjected to unknown actuator failures. It was shown that the $\mathcal{L}_1$ improved transient tracking and robustness compared to a conventional Model Reference Adaptive Controller (MRAC). To summarize, the high-gain $\mathcal{L}_1$ adaptive scheme has yielded promising results, proving capable of handling both sudden changes in disturbance and large model uncertainties.

1.3.2 Command Governor

Command governor-based control is an approach for augmenting the tracking signal given to the control system, in order to improve the tracking signal. The core idea behind using a command governor can be conceptually compared to using a reference model for introducing reference input to the control system. In case of a rapid change/step in the desired

pose, the reference will smooth the input signal to avoid saturation. Similarly, the motivation behind command governor is to achieve predictable transient and tracking behaviour of a closed-loop control system, without dependency of a high-gain adaption scheme.
A novel command governor architecture is proposed in [13], and proven to cause the closed-loop system to approximate a Hurwitz linear time-invariant (LTI) system, and stabilizing the uncertain, nonlinear model to Lyapunov.

More specifically, the idea behind command governor is to avoid the need for knowledge of the specific, conservative upper bound on the unknown weights in the uncertainty parametrization of the model, which might not be feasible to find in all applications. Without knowing the bound, it is difficult to design controllers that achieve predictable transient response and steady-state of the closed-loop.

Further, in [14], the command governor adaptive architecture is applied to a 6 degrees-of-freedom autonomous helicopter, and shown to achieve improved tracking results using the command governor compared to the baseline adaptive control. In [15], the novel command governor from [13] is augmented for use in a nonlinear controller for a 3DOF ship model, combining the command governor with an $\mathcal{L}_1$ implementation, improving transient behaviour.

1.3.3 Magnitude-Rate Saturation Model

In most control applications, it is necessary to address the issue of handling actuator constraints in order to reduce wear & tear as well as ensuring feasible control outputs. The issue has been investigated in a variety of approaches, which of one is the use of a Magnitude-Rate-Saturation model (MRS). In [16], a MRS model is developed to handle the combination of magnitude and rate saturation constraints and solving the anti-windup problem. The model is tested in simulations using a F8 aircraft model. Further, in [1], the MRS model from [16] is implemented with a cascaded nonlinear feedback controller for a scale-model ship, showing improvement of energy consumption and actuator wear in ocean basin experiments.

1.3.4 Immersion and Invariance Adaptive Control

Immersion and Invariance, I&I, as phrased in [17] is an approach for adaptive control of nonlinear systems, as well as stabilization. The approach aims to reduce the problem of designing a control system capable of adaptive stabilization of a nonlinear system into sub-problems, which can be easier to solve. This approach can be a solution in design situations where, using traditional nonlinear design, one should find an appropriate Lyapunov function candidate, which might not always be feasible. In [18], the I&I adaptive control concept is used to compensate for parametric uncertainties in a Quadrotor control implementation.

1.4 Contributions

The main contributions from this thesis are simuation and experimental results from scale testing the adaptive control concepts on a 1:90 ship model. The $\mathcal{L}_1$ adaptive control and the Immersion and Invariance adaptive control are applied to a nominal cascaded nonlinear feedback controller, and shown to improve tracking performance by compensating for model uncertainties and external disturbances for a 3-DOF ship model. Furthermore, the adaptive concepts are combined with actuator handling schemes in order to reduce energy consumption and actuator wear.

A custom made simulator is also designed and implemented with the purpose of replicating the model-scale conditions at the ocean basin, including disturbances, noise and uncertainties. The noise design is based on signal analysis of lab data to base the introduced noise on real signals.

The adaption concepts from the literature review are tested on a 3-DOF ship model and tested under real conditions at the Marine Cybernetics Laboratory (MC-lab) at the Norwegian University of Science and Technology (NTNU) in Trondheim, Norway.

Further, the work has contributed to the publication of a research paper investigating the effects of one of the actuator handling methods used in this thesis, the magnitude-rate saturation model (MRS). The paper, co-authored with Ole Nikolai Lyngstadaas and the supervisors, shows how the MRS model can reduce energy consumption and actuator wear & tear in a ship, backed up with scale model testing. The accepted paper is shown in Appendix A.

1.5 Outline

This thesis is composed of 5 chapters: Chapter 1 gives an introduction to the subject and technologies used; Chapter 2 details the deriving of the ship maneuvering model and the control approach; Chapter 3 explains the simulator development and results of the control simulations in addition to discussion; Chapter 4 presents the Marine Cybernetics Laboratory (MC-lab) and the results from lab experiments from scale-model testing, as well as modifications done between lab sessions and discussion of the results, while Chapter 5 concludes the thesis and proposes further work. Appendix A lists pose error transient plots from experiments, MATLAB model implementation and the research paper produced.

Chapter 2

Ship Modelling and Control

2.1 Ship Model and Assumptions

2.1.1 Model Definition

Normally, vessel dynamics are described with 6 DOF, with surge, sway and yaw describing position in the Cartesian 3-dimensional space, and roll, pitch and yaw as orientation variables. For a metacentrically stable ship in longitude and latitude, roll and pitch motions can be assumed zero, and since the ship is a surface vessel, vertical position changes can be discarded as the vessel is always at zero heave. Thus, the ship model can be reduced to 3 DOF.

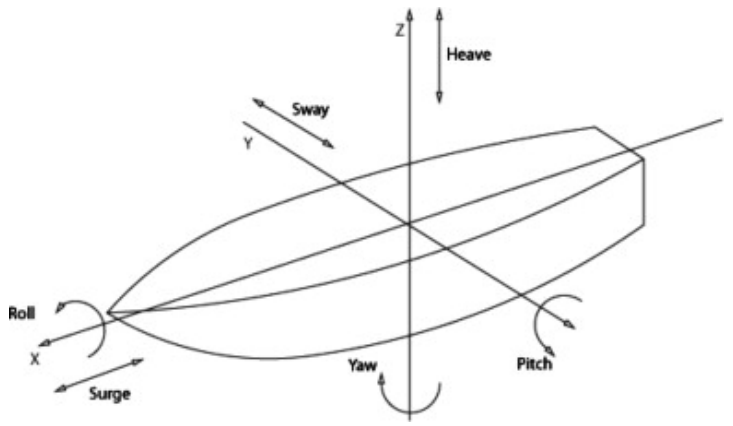

Figure 2.1: Ship degrees of freedom. Figure from [4]

The horizontal motion of a ship can be represented by the pose vector $\boldsymbol{\eta} = [x, y, \psi]^\top \in \mathbb{R}^2 \times \mathbb{S}$ and the velocity vector $\boldsymbol{\nu} = [u, v, r]^\top \in \mathbb{R}^3$. Here, (x, y) represents the Cartesian position in the local earth-fixed reference frame, ψ is the yaw angle, (u, v) represents the body-fixed linear velocities and r is the yaw rate. The 3 DOF dynamics of a ship can then be stated based on the approach in [19] as:

$$\dot{\boldsymbol{\eta}} = \boldsymbol{R}(\psi)\boldsymbol{\nu} \tag{2.1}$$

$$\boldsymbol{M}\dot{\boldsymbol{\nu}} + \boldsymbol{C}(\boldsymbol{\nu})\boldsymbol{\nu} + \boldsymbol{D}(\boldsymbol{\nu})\boldsymbol{\nu} = \boldsymbol{\tau}, \tag{2.2}$$

where $\boldsymbol{M} \in \mathbb{R}^{3\times3}$, $\boldsymbol{C}(\boldsymbol{\nu}) \in \mathbb{R}^{3\times3}$, $\boldsymbol{D}(\boldsymbol{\nu}) \in \mathbb{R}^{3\times3}$ and $\boldsymbol{\tau} = [\tau_1, \tau_2, \tau_3]^\top$ represent the inertia matrix, Coriolis and centripetal matrix, damping matrix and control input vector, respectively. The rotation matrix $\boldsymbol{R}(\psi) \in SO(3)$ is given by

$$\boldsymbol{R}(\psi) = \begin{bmatrix} \cos(\psi) & -\sin(\psi) & 0 \\ \sin(\psi) & \cos(\psi) & 0 \\ 0 & 0 & 1 \end{bmatrix}. \tag{2.3}$$

The system matrices are assumed to satisfy the properties $\boldsymbol{M} = \boldsymbol{M}^\top > 0$, $\boldsymbol{C}(\boldsymbol{\nu}) = -\boldsymbol{C}(\boldsymbol{\nu})^\top$ and $\boldsymbol{D}(\boldsymbol{\nu}) > 0$.

The inertia matrix is given as

$$\boldsymbol{M} = \boldsymbol{M}_{RB} + \boldsymbol{M}_A, \tag{2.4}$$

where

$$\boldsymbol{M}_{RB} = \begin{bmatrix} m & 0 & 0 \\ 0 & m & mx_g \\ 0 & mx_g & I_z \end{bmatrix} \tag{2.5}$$

$$\boldsymbol{M}_A = \begin{bmatrix} -X_{\dot{u}} & 0 & 0 \\ 0 & -Y_{\dot{v}} & -Y_{\dot{r}} \\ 0 & -N_{\dot{v}} & -N_{\dot{r}} \end{bmatrix}. \tag{2.6}$$

The Coriolis and centripetal matrix is given as

$$\boldsymbol{C}(\boldsymbol{\nu}) = \boldsymbol{C_{RB}}(\boldsymbol{\nu}) + \boldsymbol{C_A}(\boldsymbol{\nu}), \tag{2.7}$$

where

$$\boldsymbol{C_{RB}}(\boldsymbol{\nu}) = \begin{bmatrix} 0 & 0 & -m(x_g r + v) \\ 0 & 0 & mu \\ m(x_g r + v) & -mu & 0 \end{bmatrix} \tag{2.8}$$

$$\boldsymbol{C_A}(\boldsymbol{\nu}) = \begin{bmatrix} 0 & 0 & -c_{A,13}(\boldsymbol{\nu}) \\ 0 & 0 & c_{A,23}(\boldsymbol{\nu}) \\ c_{A,13}(\boldsymbol{\nu}) & -c_{A,23}(\boldsymbol{\nu}) & 0 \end{bmatrix}, \tag{2.9}$$

with

$$c_{A,13}(\boldsymbol{\nu}) = -Y_{\dot{v}} v - Y_{\dot{r}} r \tag{2.10}$$

$$c_{A,23}(\boldsymbol{\nu}) = -X_{\dot{u}} u. \tag{2.11}$$

Finally, the damping matrix $\boldsymbol{D}(\boldsymbol{\nu})$ is defined as

$$\boldsymbol{D}(\boldsymbol{\nu}) = \boldsymbol{D_L} + \boldsymbol{D_{NL}}(\boldsymbol{\nu}), \tag{2.12}$$

where

$$\boldsymbol{D_L} = \begin{bmatrix} -X_u & 0 & 0 \\ 0 & -Y_v & -Y_r \\ 0 & -N_v & -N_r \end{bmatrix} \tag{2.13}$$

$$\boldsymbol{D_{NL}}(\boldsymbol{\nu}) = \begin{bmatrix} d_{NL,11}(\nu) & 0 & 0 \\ 0 & d_{NL,22}(\boldsymbol{\nu}) & d_{NL,23}(\boldsymbol{\nu}) \\ 0 & d_{NL,32}(\boldsymbol{\nu}) & d_{NL,33}(\boldsymbol{\nu}) \end{bmatrix}, \tag{2.14}$$

with

$$d_{NL,11}(\boldsymbol{\nu}) = -X_{|u|u}|u| - X_{uuu}u^2 \tag{2.15}$$
$$d_{NL,22}(\boldsymbol{\nu}) = -Y_{|v|v}|v| - Y_{|r|v}|r| - Y_{vvv}v^2 \tag{2.16}$$
$$d_{NL,23}(\boldsymbol{\nu}) = -Y_{|r|r}|r| - Y_{|v|r}|r| - Y_{rrr}r^2 - Y_{ur}u \tag{2.17}$$
$$d_{NL,32}(\boldsymbol{\nu}) = -N_{|v|v}|v| - N_{|r|v}|v| - N_{vvv}v^2 - N_{uv}u \tag{2.18}$$
$$d_{NL,33}(\boldsymbol{\nu}) = -N_{|r|r}|r| - N_{|v|r}|v| - N_{rrr}r^2 - N_{ur}u. \tag{2.19}$$

In order to successfully accommodate for the Munk moment as described in [20], the damping terms

$$Y_{ur} = -X_{\dot{u}} \tag{2.20}$$
$$N_{uv} = -(Y_{\dot{v}} - X_{\dot{u}}) \tag{2.21}$$
$$N_{ur} = -Y_{\dot{r}}, \tag{2.22}$$

are introduced, so that when multiplied with u, are linearly increasing with the forward speed, and added to the damping matrix. This will result in a more physically realistic model behaviour, and will ensure that the model will not give rise to a physically impossible motion.

For this thesis, the model-scale ship C/S Inocean Cat I Drillship [2], abbreviated CSAD, will be used. CSAD is a 1:90 scale replica of a supply ship, with a length of $L = 2.578\ \mathrm{m}$, mass $m = 127.92\ \mathrm{kg}$ and inertia about z-axis in the BODY-frame $I_z = 61.987\ \mathrm{kg\,m^2}$. $x_g = 0.00375\ \mathrm{m}$ is the distance along the x-axis in the body frame from the centre of gravity. The full list of model parameters values for CSAD are shown in Table 2.1. The scale-model CSAD is shown in Figure. 2.2.

Table 2.1 compares the parameter values from [21] with the values used for this thesis. The change is due to inacurracies in the model discovered during initial testing. The bolded values have been updated from the latest article regarding the CSAD. In [21], the parameters in $\boldsymbol{M}_A$ were positive signed, which does not make sense as they relate to the

Figure 2.2: C/S Inocean Cat I Drillship in the MC-lab.

added mass in the inertia matrix, resulting in ”removed mass”. It could be that the wrong signage was a typo or an break in convention.

Furthermore, the parameters N_r, $N_{|r|r}$ and N_{rrr} relate to the yaw motion, and were found to be too small regarding the ships relative yaw, giving the model a maximum yaw rate of 8398 [deg/s]. These parameters had not been scaled according to a realistic yaw rate, which was found to be 5 [deg/s], based on the maximum rotation rate from experiments done at the MC-lab in November 2017. To approximate appropriate values for these parameters, the internal scalings are kept as in [21], with the higher order terms dependent on N_r, and the ship model is simulated with a constant maximal yaw-moment. The value of N_r is then tuned until the model yields a yaw-rate of approximately 5 [deg/s]. The resulting parameter values are displayed in the center-right column in Table 2.1, marked in bold. The updated parameters are used for the first lab session. During this session, it was discovered that the model parameters still did not fully reflect physical behaviour, and further model identification is then done, as will be discussed in Chapter 4.

Parameter	Old parameters [21]	Lab1 parameters	Unit
L	2.578	2.578	m
m	127.92	127.92	kg
x_g	0	**0.0375**	m
I_z	62	62	kgm^2
$X_{\dot{u}}$	3.26	**−3.26**	kg
$Y_{\dot{v}}$	28.9	**−28.9**	kg
$Y_{\dot{r}}$	0.525	**−0.525**	kgm
$N_{\dot{v}}$	0.157	**−0.157**	kgm
$N_{\dot{r}}$	14	**−14**	kgm^2
X_u	−2.33	-2.33	kg/s
$X_{\|u\|u}$	0	0	kg/m
X_{uuu}	−8.56	-8.56	kgs/m^2
Y_v	-4.67	-4.67	kg/s
$Y_{\|v\|v}$	0.398	**−0.398**	kg/m
Y_{vvv}	−313	-313	kgs/m^2
N_v	0	0	kgm/s
$N_{\|v\|v}$	−0.209	-0.209	kg/m
N_{vvv}	0	0	kgs/m^2
Y_r	−7.25	-7.25	kgm/s
$Y_{\|r\|r}$	−3.450	-3.450	kg/m
Y_{rrr}	0	0	kgs/m^2
N_r	−0.0168	**−6.916**	kg/s
$N_{\|r\|r}$	−0.0115	**−4.734**	kgm^2
N_{rrr}	−0.000358	**−0.147**	kgs/m^2
$N_{\|v\|r}$	0.08	0.08	kg/m
$N_{\|r\|v}$	0.08	0.08	kg/m
$Y_{\|v\|r}$	−0.845	-0.845	kg
$Y_{\|r\|v}$	−0.805	-0.805	kg

Table 2.1: Numerical values of the ship model parameters for CSAD.

2.1.2 Assumptions and Uncertainties

The kinetic model used in model-based control application is normally determined by approximations and estimations, and will never represent the real world exactly. The uncertainties present in this approximated model will influence the performance of the control system. To counter this effect, a parameterization of uncertainty in the model is introduced, and a adaptive scheme is designed to change the system on-line. As well as handling inherent uncertainties, robust adaptive control can also compensate for measurement noise and disturbances in the closed-loop control system. The parameterization of uncertainties is then used to design a simulator that resembles the scale-model conditions under which the control implementation is tested at MC-lab.

For the 3 DOF ship model used in this thesis, the following parameterization is used based on [15], giving the relation between real $\boldsymbol{M}^*$, $\boldsymbol{C}^*$, $\boldsymbol{D}^*$ and the considered matrices:

$$\boldsymbol{M}^* = \delta \boldsymbol{M} \tag{2.23}$$

$$\boldsymbol{C}^* = \delta \boldsymbol{C}(\boldsymbol{\nu}) \tag{2.24}$$

$$\boldsymbol{D}^* = \sigma \boldsymbol{D}(\boldsymbol{\nu}). \tag{2.25}$$

It is assumed that disturbance and measurement noise is present in the system, which is discussed further in Chapter 3. In addition, the uncertainty of the actuator system in relation to the control input is given as $\boldsymbol{\tau}^* = \rho\boldsymbol{\tau}$.

For notational simplicity, the matrices $\boldsymbol{C}(\boldsymbol{\nu})$, $\boldsymbol{D}(\boldsymbol{\nu})$ and $\boldsymbol{R}(\psi)$ will be written as $\boldsymbol{C}$, $\boldsymbol{D}$ and $\boldsymbol{R}$ for most of this thesis.

2.2 Methods of Actuator Handling

2.2.1 Command Governor

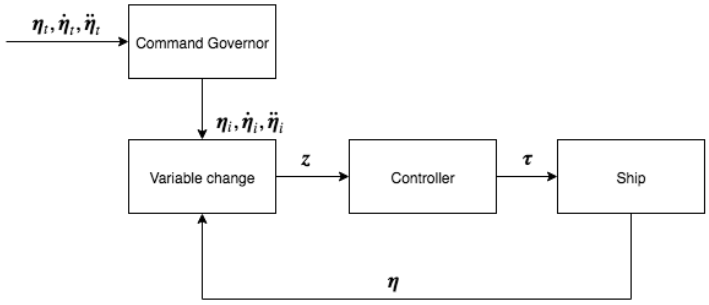

Figure 2.3: Principal sketch of the Command Governor architecture

In [13], a novel command governor structure is presented for use with traditional MRAC adaptive structure. This novel command governor is fitted to a 3-DOF nonlinear model in [15], and this approach is utilized for use in this thesis. As seen in Figure 2.3, the command governor alters the reference signals given to the controller, and such the following structure is added to the pose controller in the cascaded system in Figure 2.5. The dynamics for the new reference signal $\boldsymbol{\eta_i}$ is proposed as

$$\dot{\boldsymbol{\eta}}_i = \dot{\boldsymbol{\eta}}_t - \boldsymbol{K}_a(\boldsymbol{\eta} - \boldsymbol{\eta}_i) - K_b(\boldsymbol{\eta_t} - \boldsymbol{\eta}_i) \tag{2.26}$$

and

$$\ddot{\boldsymbol{\eta}}_i = \ddot{\boldsymbol{\eta}}_t - \boldsymbol{K}_a(\dot{\boldsymbol{\eta}} - \dot{\boldsymbol{\eta}}_i) - \boldsymbol{K}_b(\dot{\boldsymbol{\eta}}_{\boldsymbol{t}} - \dot{\boldsymbol{\eta}}_i). \tag{2.27}$$

$\boldsymbol{K}_a > 0, \boldsymbol{K}_b > 0$ can be interpreted as gains of the command governor, regulating the transient behavior the command governor with regard to $\boldsymbol{\eta}_t$. Since the adding of the command governor changes the pose control error $\boldsymbol{z}_1$ in (2.35) to $\boldsymbol{R}^\top(\psi)(\boldsymbol{\eta} - \boldsymbol{\eta}_i)$, a new control error is introduced:

$$\boldsymbol{z}_0 = \boldsymbol{\eta}_i - \boldsymbol{\eta}_t, \tag{2.28}$$

with a corresponding quadratic control Lyapunov function

$$V_0 = \frac{1}{2}\boldsymbol{z}_0^\top \boldsymbol{z}_0. \tag{2.29}$$

Differentiation of V_0 with respect to time along the dynamics gives

$$\begin{aligned}
\dot{V}_0 &= \boldsymbol{z}_0^\top \dot{\boldsymbol{z}}_0 && (2.30)\\
&= \boldsymbol{z}_0^\top(-\boldsymbol{K}_a(\boldsymbol{\eta} - \boldsymbol{\eta}_i) - \boldsymbol{K}_b(\boldsymbol{\eta_t} - \boldsymbol{\eta}_i)) && (2.31)\\
&= -\boldsymbol{z}_0^\top \boldsymbol{K}_a \boldsymbol{R}(\psi)\boldsymbol{z}_1 - \boldsymbol{z}_0^\top \boldsymbol{K}_b \boldsymbol{z}_0. && (2.32)
\end{aligned}$$

The desired velocity $\boldsymbol{\alpha}$ in (2.3.1) is changed to compensate for the $-\boldsymbol{z}_0^\top K_a \boldsymbol{R}(\psi)\boldsymbol{z}_1$ term, giving

$$\boldsymbol{\alpha} = \boldsymbol{R}^\top \boldsymbol{\eta}_t - \boldsymbol{K}_1(\cdot)\boldsymbol{z}_1 + \boldsymbol{z}_0^\top \boldsymbol{K}_a \boldsymbol{R}(\psi)\boldsymbol{z}_1, \tag{2.33}$$

as the desired velocity function in the command governor fitted cascaded controller.

2.2.2 Magnitude-Rate Saturation

The MRS model used in this thesis is based on the approach in [16] and subsequently [1], where the magnitude and rate saturation combination is parametrized as

$$\begin{aligned}
\dot{\boldsymbol{\delta}} &= sat_{\boldsymbol{r}}(\dot{\boldsymbol{\tau}}_c + \boldsymbol{K}(\boldsymbol{\tau_c} - \boldsymbol{\delta}))\\
\boldsymbol{\tau}_{mrs} &= sat_{\boldsymbol{m}}(\boldsymbol{\delta}).
\end{aligned} \tag{2.34}$$

$\boldsymbol{K}$ is a free parameter, which should be kept positive and $\boldsymbol{K} \neq I$. The input from the control algorithm, $\boldsymbol{\tau}_c$ is differentiated using numerical derivation. Intuitively, the $\boldsymbol{K}$ can be interpreted as a gain parameter regulating the inner loop speed, and consequently should be carefully selected. The selection of $\boldsymbol{K}$ is investigated further in [3]. A block diagram of the MRS model used is seen in Figure 2.4

The magnitude limits, based on the actuator configuration of the ship is chosen as $sat_{\boldsymbol{m}} = [m_1, m_2, m_3]$. The rate saturation limits are chosen by $\boldsymbol{r} = [m_1/t_{mrs,1}, m_2/t_{mrs,2}, m_3/t_{mrs,3}]^\top$, where m_1, m_2 and m_3 are the magnitude saturation limits given by $sat_{\boldsymbol{m}}$, and where $t_{mrs,1}$, $t_{mrs,2}$ and $t_{mrs,3}$, are the desired transition time for the actuators to reach maximum output in surge, sway and yaw, respectively. The tuning of the rate and magnitude limits is discussed further in [3].

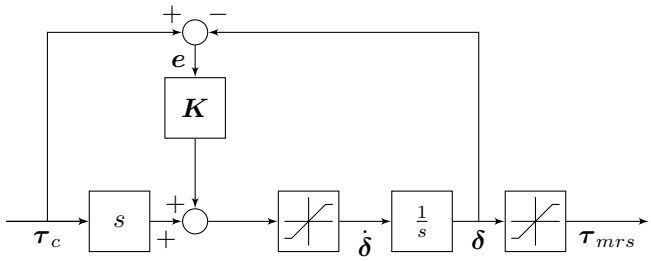

Figure 2.4: Diagram of the MRS model. From [1]

2.3 Adaptive Control

2.3.1 $\mathcal{L}_1$ Adaptive Control

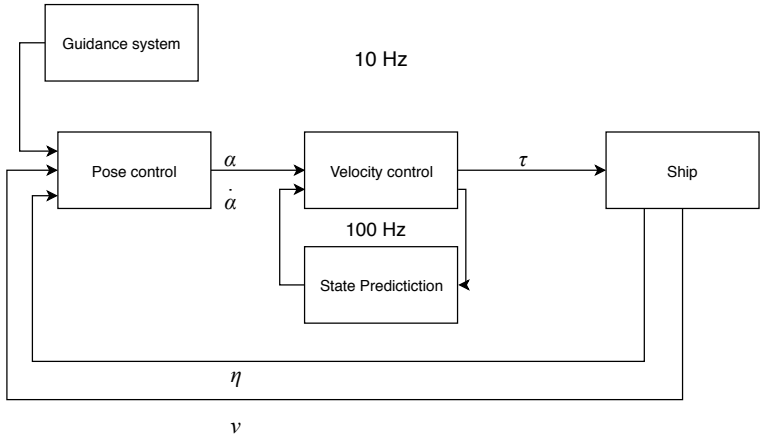

Figure 2.5: Principal sketch of the $\mathcal{L}_1$ Adaptive control architecture used in this thesis

Figure 2.5 shows the concept of the $\mathcal{L}_1$ architecture applied on a cascaded control structure,

as used in this thesis. The decoupling of control and adaptation is shown, where the state prediction runs at 100 Hz while the control system runs at 10 Hz. This concept is shown in Figure 2.6, for the pose state $\boldsymbol{\eta}$. At every 10 samples, a new measurement is given to the controller as seen in Figure 2.5, and in between samples the state is predicted. This is done for both velocity and position.

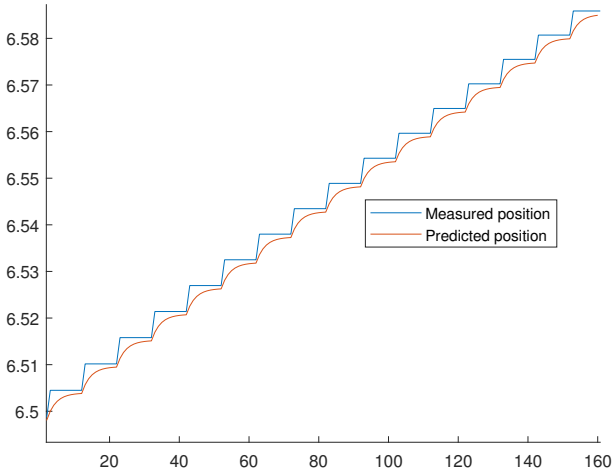

Figure 2.6: State prediction in $\mathcal{L}_1$ adaptive control

The design procedure of an $\mathcal{L}_1$ adaptive scheme is usually approached in 2 stages; One stage consists of the design of a state estimator and and predictor as well as laws for adaptation updates, and the other stage concerns the design of the control law. The $\mathcal{L}_1$ Adaptive control system is designed as a cascaded control system, in which a nominal controller will be augmented with the $\mathcal{L}_1$ architecture. The nominal controller is a cascaded feedback nonlinear pose and velocity type system, as presented in [7].

Stage 1: Nominal Control

The design of the cascaded control law is based on the approach in [7], which proposes a control approach based on a cascaded structure with subsystems for kinematic and kinetic control. The control system uses nonlinear feedback of both pose and velocity, abbreviated NP-NV. The control errors for both pose and velocity $\boldsymbol{z}_i, i \in (1, 2)$ are defined as:

$$\boldsymbol{z_1} = \boldsymbol{R}^\top(\psi)(\boldsymbol{\eta} - \boldsymbol{\eta_t}) \tag{2.35}$$

$$\boldsymbol{z_2} = \boldsymbol{\nu} - \boldsymbol{\alpha} \tag{2.36}$$

The control law is developed through the use of Control Lyapunov functions. The first quadratic function candidate is defined as:

$$V_1 = \frac{1}{2}\boldsymbol{z}_1^\top \boldsymbol{z}_1. \tag{2.37}$$

Differentiating V_1 by time, the expression becomes

$$\begin{aligned}
\dot{V}_1 &= \boldsymbol{z}_1^\top \dot{\boldsymbol{z}}_1 && (2.38)\\
&= \boldsymbol{z}_1^\top (\boldsymbol{S}^\top(r)\boldsymbol{R}^\top(\psi)((\boldsymbol{\eta} - \boldsymbol{\eta_t}) + \boldsymbol{R}^\top(\psi)(\boldsymbol{\eta}(\dot{\boldsymbol{\eta}} - \dot{\boldsymbol{\eta}}_{\boldsymbol{t}}) && (2.39)\\
&= \boldsymbol{z}_1^\top (\boldsymbol{S}^\top(r)\boldsymbol{z} + \boldsymbol{R}^\top(\psi)(\boldsymbol{\eta}(\dot{\boldsymbol{\eta}} - \dot{\boldsymbol{\eta}}_{\boldsymbol{t}}). && (2.40)
\end{aligned}$$

$\boldsymbol{S}^\top(r)$ is a skew-symmetric matrix with the property $\boldsymbol{z}_1^\top \boldsymbol{S}^\top(r)\boldsymbol{z}_1 = 0$. Using this property and the fact that $\boldsymbol{\nu} = \boldsymbol{R}^\top \boldsymbol{\eta}$, $\dot{V}_1$ reduces to

$$\dot{V}_1 = \boldsymbol{z}_1^\top (\boldsymbol{\nu} - \boldsymbol{R}^\top \eta_t). \tag{2.41}$$

Inserting (2.36) in (2.41), $\dot{V}_1$ becomes

$$\dot{V}_1 = \boldsymbol{z}_1^\top (\boldsymbol{z}_2 + \boldsymbol{\alpha} - \boldsymbol{R}^\top \eta_t). \tag{2.42}$$

The vector $\boldsymbol{\alpha}$ can be intuitively interpreted as the desired velocity computed by the kinematic subsystem, and should be chosen so that origin of the subsystem is stable. Choosing $\boldsymbol{\alpha}$ as

$$\boldsymbol{\alpha} = \boldsymbol{R}^\top \boldsymbol{\eta}_t - \boldsymbol{K}_1(\cdot)\boldsymbol{z}_1 \tag{2.43}$$

gives a negative definite $\dot{V}_1$

$$\dot{V}_1 = -\boldsymbol{z}_1^\top \boldsymbol{K}_1(\cdot)\boldsymbol{z}_1 + \boldsymbol{z}_1^\top \boldsymbol{z}_2 \tag{2.44}$$

when $\boldsymbol{z}_2 = 0$.

The kinematic subsystem is derived from the $\boldsymbol{z}_2$ dynamics, written as

$$\begin{aligned}
\boldsymbol{M}\dot{\boldsymbol{z}}_2 &= \boldsymbol{M}(\dot{\boldsymbol{\nu}} - \dot{\boldsymbol{\alpha}}) && (2.45)\\
&= \boldsymbol{\tau} - (\boldsymbol{C} - \boldsymbol{D})\boldsymbol{\nu} - \boldsymbol{M}\dot{\boldsymbol{\alpha}}, && (2.46)
\end{aligned}$$

by (2.2). Differentiated desired velocity $\boldsymbol{\alpha}$ becomes

$$\dot{\boldsymbol{\alpha}} = \boldsymbol{R}^\top(\psi)\ddot{\eta}_t + \boldsymbol{S}^\top(r)\boldsymbol{R}^\top(\psi)\dot{\eta}_t - \boldsymbol{K}(\cdot)\dot{\boldsymbol{z}}_1. \tag{2.47}$$

A Control Lyapunov Function for the second subsystem is defined as

$$V_2 = \frac{1}{2}\boldsymbol{z}_2^\top \boldsymbol{M}\boldsymbol{z}_2, \tag{2.48}$$

and differentiated by time as

$$\begin{aligned} \dot{V}_2 &= \boldsymbol{z}_2^\top \boldsymbol{M}\dot{\boldsymbol{z}}_2 && (2.49)\\ &= \boldsymbol{z}_2^\top(\boldsymbol{\tau} - (\boldsymbol{C}-\boldsymbol{D})\boldsymbol{\alpha} - \boldsymbol{M}\dot{\boldsymbol{\alpha}}). && (2.50) \end{aligned}$$

The control law $\boldsymbol{\tau}$ to give stable origin is then chosen as

$$\boldsymbol{\tau} = \boldsymbol{M}\dot{\boldsymbol{\alpha}} + (\boldsymbol{C}-\boldsymbol{D})\boldsymbol{\alpha} - \boldsymbol{K}_2(\cdot)\boldsymbol{z}_2, \tag{2.51}$$

giving

$$\dot{V}_2 = -\boldsymbol{M}^{-1}\boldsymbol{K}_2(\cdot)\boldsymbol{z}_2 < 0 \tag{2.52}$$

The nonlinear feedback terms $\boldsymbol{K}_1, \boldsymbol{K}_2$ are defined as

$$\boldsymbol{K_1}(\cdot) = \boldsymbol{\Gamma}_1 \begin{bmatrix} \frac{1}{\sqrt{\boldsymbol{z}_{\boldsymbol{1},\tilde{\boldsymbol{p}}}^{\boldsymbol{T}}\boldsymbol{z}_{\boldsymbol{1},\tilde{\boldsymbol{p}}}+\Delta_{\tilde{p}}^2}}\boldsymbol{I}_{2x2} & \boldsymbol{0}_{2x1} \\ \boldsymbol{0}_{1x2} & \frac{1}{\sqrt{z_{1,\tilde{\psi}}^2+\Delta_{\tilde{\psi}}^2}} \end{bmatrix}, \tag{2.53}$$

with $\boldsymbol{z_{1,\tilde{p}}} = [z_{1,x}, z_{1,y}]^\top$ and $\Delta_i > 0$ are tuning parameters, and

$$\boldsymbol{K_2}(\cdot) = \boldsymbol{\Gamma}_2 \begin{bmatrix} \frac{1}{\sqrt{\boldsymbol{z}_{\boldsymbol{2},\tilde{\nu}}^{\boldsymbol{T}}\boldsymbol{z}_{\boldsymbol{2},\tilde{\nu}}+\Delta_{\tilde{\nu}}^2}}\boldsymbol{I}_{2x2} & \boldsymbol{0}_{2x1} \\ \boldsymbol{0}_{1x2} & \frac{1}{\sqrt{z_{2,\tilde{r}^2}+\Delta_{\tilde{r}}^2}} \end{bmatrix}, \tag{2.54}$$

with $\boldsymbol{z_{2,\tilde{\nu}}} = [z_{2,u}, z_{2,v}]^\top$ and $\Delta_i > 0$ are tuning parameters. The design of the feedback terms is inspired by constant bearing guidance, and is detailed in [7].

Stage 2: State Predictor and Adaptation

The prediction errors is defined as:

$$\tilde{\boldsymbol{\eta}} = \hat{\boldsymbol{\eta}} - \boldsymbol{\eta} \tag{2.55}$$

$$\tilde{\boldsymbol{\nu}} = \hat{\boldsymbol{\nu}} - \boldsymbol{\nu}, \tag{2.56}$$

with $\boldsymbol{\eta}, \boldsymbol{\nu}$ being measured pose and velocity and $\hat{\boldsymbol{\eta}}, \hat{\boldsymbol{\nu}}$ being the respective estimates. The state prediction dynamics are defined as

$$\dot{\hat{\boldsymbol{\eta}}} = \boldsymbol{L_1}\tilde{\boldsymbol{\eta}} + \boldsymbol{R}\boldsymbol{\nu} \tag{2.57}$$

$$\dot{\hat{\boldsymbol{\nu}}} = \boldsymbol{L_2}\tilde{\boldsymbol{\nu}} + \boldsymbol{M^{-1}}(\boldsymbol{\tau} + \boldsymbol{R}^T\hat{\boldsymbol{w}}_{\boldsymbol{\delta}} - \boldsymbol{C}\boldsymbol{\nu} - \boldsymbol{D}\boldsymbol{\nu}). \tag{2.58}$$

To design the adaptation laws, a positive definite CLF is proposed:

$$V_1 = \frac{1}{2\gamma_{w_\delta}}\tilde{\boldsymbol{w}}_\delta^T\tilde{\boldsymbol{w}}_\delta + \frac{1}{2}\tilde{\boldsymbol{\eta}}^T\tilde{\boldsymbol{\eta}} + \frac{1}{2}\tilde{\boldsymbol{\nu}}^T\boldsymbol{M}\tilde{\boldsymbol{\nu}} \tag{2.59}$$

Differentiation of V_1 w.r.t time gives

$$\dot{V}_1 = \frac{1}{\gamma_{w_\delta}}\tilde{\boldsymbol{w}}_\delta\dot{\hat{\boldsymbol{w}}}_\delta - \tilde{\boldsymbol{\eta}}^T\boldsymbol{L_1}\tilde{\boldsymbol{\eta}} + \tilde{\boldsymbol{\nu}}^T(-\boldsymbol{M}\boldsymbol{L_2}\tilde{\boldsymbol{\nu}} + \boldsymbol{\tau} + \boldsymbol{R}^T\tilde{\boldsymbol{w}}_{\boldsymbol{\delta}} - \boldsymbol{D}\boldsymbol{\nu}) \tag{2.60}$$

$$\dot{V}_1 = -\tilde{\boldsymbol{\eta}}^T\boldsymbol{L_1}\tilde{\boldsymbol{\eta}} - \tilde{\boldsymbol{\nu}}^T\boldsymbol{M}\boldsymbol{L_2}\tilde{\boldsymbol{\nu}} + \tilde{\boldsymbol{w}}_\delta^T(\frac{1}{\gamma_{w_\delta}}\dot{\hat{\boldsymbol{w}}}_\delta + \boldsymbol{R}\tilde{\boldsymbol{\nu}}). \tag{2.61}$$

The next step is to choose a adaptation law that ensure a negative definite $\dot{V}_1$ for all $\boldsymbol{\eta}, \boldsymbol{\nu} \neq \mathbf{0}$. Choosing adaptation law

$$\dot{\hat{\boldsymbol{w}}}_\delta = -\gamma_{w_\delta}\boldsymbol{R}\tilde{\boldsymbol{\nu}}, \tag{2.62}$$

$\dot{V}_1$ becomes

$$\dot{V}_1 = -\tilde{\boldsymbol{\eta}}^T\boldsymbol{L_1}\tilde{\boldsymbol{\eta}} - \tilde{\boldsymbol{\nu}}^T\boldsymbol{M}\boldsymbol{L_2}\tilde{\boldsymbol{\nu}}, \tag{2.63}$$

which is negative semi-definite.

To extend the nominal NP-NV with the adaptive terms, the control law from (2.3.1) is altered to the adaptive control law

$$\boldsymbol{\tau} = \boldsymbol{M}\dot{\boldsymbol{\alpha}} + (\boldsymbol{C} - \boldsymbol{D})\boldsymbol{\alpha} - \boldsymbol{K}_2(\cdot)\boldsymbol{z}_2 - \hat{\boldsymbol{w}}_\delta. \tag{2.64}$$

As mentioned earlier, the name of the adaptive control concept comes from the $\mathcal{L}_1$ norm from the stability. In this thesis, for simplicity the term $\mathcal{L}_1$ is used to describe the adaptive control, instead the norm.

Stability and Parameter Tuning

In [22], the NP-NV controller is proven to have the stability properties of uniformly globally asymptotically stable (UGAS) origin $(\boldsymbol{z}_1, \boldsymbol{z}_2) = (\mathbf{0}, \mathbf{0})$. Further, on each compact set $B \triangleq \{\boldsymbol{z}_1, \boldsymbol{z}_2\} \subset \mathbb{R}^6$ containing the origin, it is uniformly exponentially stable (UES).

The key tuning rules are detailed in [22], and can be related by the relationship between the kinetic and the kinematic subsystem, where of the two, the kinetic subsystem should be faster, thus the gain parameters should be have smaller time constants.

The Δ-values scale linear feedback gains and time constants in the linear region, and should consequently keep this relationship, ensuring that the kinetic subsystem is faster than the kinematic.

The state predictor gain parameters $\boldsymbol{L_1}, \boldsymbol{L_2}$ are chosen by tuning rules based on the time constants of the system, as suggested by [22]. By the relation between gain and time constants

$$\boldsymbol{T_{L1}} = \boldsymbol{L_1}^{-1} \tag{2.65}$$

$$\boldsymbol{T_{L2}} = \boldsymbol{L_2}^{-1} \tag{2.66}$$

where

$$\boldsymbol{T_L 1} = \begin{bmatrix} t_{L_1} & 0 & 0 \\ 0 & t_{L_1} & 0 \\ 0 & 0 & t_{L_1} \end{bmatrix} \tag{2.67}$$

$$\boldsymbol{T_L 2} = \begin{bmatrix} t_{L_2} & 0 & 0 \\ 0 & t_{L_2} & 0 \\ 0 & 0 & t_{L_2} \end{bmatrix}. \tag{2.68}$$

In [8]-[9], it is suggested to set the predictor gains $\boldsymbol{L_1}, \boldsymbol{L_2}$ as high as the computer system can handle without overflow. This will introduce system noice, which is then handled using a low-pass filter in the control law to filter the noise. By this approach, the stability of the adaptive controller can be shown using the $\mathcal{L}_1$ norm requirement, derived from the *small gain requirement* in [23].

$$||\bar{\boldsymbol{G}}(s)||_{\mathcal{L}_1} \boldsymbol{L} < 1.$$

However, in the application in this thesis, no filter is implemented, and the gains are selected by the time constants instead. Thus, the $\mathcal{L}_1$ norm requirement cannot be used to show stability, and the proof becomes difficult and will not be shown in this thesis. For the interested reader, it is suggested to obtain the proof using the method of observing that a feedback interconnection is equivalent to a cascaded inter-connection, as proposed in [24].

2.3.2 Immersion and Invariance Adaptive Control

To simplify the implementation of the Immersion and Invariance Adaptive concept, the focus will be on handling the uncertainties in the nonlinear damping matrix as well as system disturbance. However, as previously mentioned, it can be assumed that uncertainties are present in the inertia matrix $\boldsymbol{M}$ as well as the coriolis and centripetal matrix $\boldsymbol{C}(\boldsymbol{\nu})$. Based on the adaptive approach I&I in [17], the system model definition in (2.1)-(2.2) can be rewritten as

$$\dot{\boldsymbol{\eta}} = \boldsymbol{R}(\psi)\boldsymbol{\nu} \tag{2.69}$$

$$\boldsymbol{M}\dot{\boldsymbol{\nu}} = \boldsymbol{\tau} + \boldsymbol{R}^{\top}\boldsymbol{w_{\delta}} - \boldsymbol{C}(\boldsymbol{\nu})\boldsymbol{\nu} + \boldsymbol{g}(\boldsymbol{\nu})\boldsymbol{\nu} + \boldsymbol{\Phi}(\boldsymbol{\nu})\boldsymbol{\phi}, \tag{2.70}$$

where $\boldsymbol{w_{\delta}}$ is the system disturbance, $\boldsymbol{g}(\boldsymbol{\nu})\boldsymbol{\nu}$ is $-\boldsymbol{D}(\boldsymbol{\nu})\boldsymbol{\nu}$ and $\boldsymbol{\Phi}(\boldsymbol{\nu})$, $\boldsymbol{\phi}$ are defined as

$$\boldsymbol{\Phi}(\boldsymbol{\nu})\boldsymbol{\nu} = \begin{bmatrix} 0 & 0 & 0 & 0 & 0 & 0 & 0 & 0 & cos(\psi) & sin(\psi) & 0 \\ |r|v & r & |v|r & |r|r & 0 & 0 & 0 & 0 & -sin(\psi) & cos(\psi) & 0 \\ 0 & 0 & 0 & 0 & |r|v & r & |v|r & |r|r & 0 & 0 & 1 \end{bmatrix} \tag{2.71}$$

$$\boldsymbol{\phi} = [Y_{|r|v}, Y_r, Y_{|v|r}, Y_{|r|r}, N_{|r|v}, N_r, N_{|v|r}, N_{|r|r}, w_1, w_2, w_3]^{\top}, \tag{2.72}$$

based on the damping matrix parametrization in (2.13). Revisiting the non-adaptive NP-NV cascaded controller presented earlier, which will be extended using the novel I&I adaptive framework, we have the control errors defined in (2.35)-(2.36) as

$$\boldsymbol{z_1} = \boldsymbol{R}^{\top}(\psi)(\boldsymbol{\eta} - \boldsymbol{\eta_t})$$
$$\boldsymbol{z_2} = \boldsymbol{\nu} - \boldsymbol{\alpha},$$

as well as desired velocity and control law

$$\boldsymbol{\alpha} = \boldsymbol{R}^{\top}\boldsymbol{\eta}_t - \boldsymbol{K}_1(\cdot)\boldsymbol{z}_1$$
$$\boldsymbol{\tau} = \boldsymbol{M}\dot{\boldsymbol{\alpha}} + (\boldsymbol{C} - \boldsymbol{D})\boldsymbol{\alpha} - \boldsymbol{K}_2(\cdot)\boldsymbol{z}_2.$$

The manifold is defined as the estimation error, inspired by the approach in [18]

$$\tilde{\boldsymbol{\phi}} = \hat{\boldsymbol{\phi}} - \boldsymbol{\phi} + \boldsymbol{\beta}(\boldsymbol{z}), \tag{2.73}$$

which gives the manifold dynamics

$$\dot{\tilde{\boldsymbol{\phi}}} = \dot{\hat{\boldsymbol{\phi}}} + \frac{\partial \boldsymbol{\beta}}{\partial \boldsymbol{z}_1^{\top}}\dot{\boldsymbol{z}}_1 + \frac{\partial \boldsymbol{\beta}}{\partial \boldsymbol{z}_2^{\top}}\dot{\boldsymbol{z}}_2 \tag{2.74}$$

$$= \dot{\hat{\boldsymbol{\phi}}} + \frac{\partial \boldsymbol{\beta}}{\partial \boldsymbol{z}_1^{\top}}\dot{\boldsymbol{z}}_1 + \frac{\partial \boldsymbol{\beta}}{\partial \boldsymbol{z}_2^{\top}}(\boldsymbol{\tau} - \boldsymbol{M}\dot{\boldsymbol{\alpha}} + \boldsymbol{R}^{\top}\boldsymbol{w_{\delta}} - \boldsymbol{C}(\boldsymbol{\nu})\boldsymbol{\nu} \tag{2.75}$$

$$+ \boldsymbol{g}(\boldsymbol{\nu})\boldsymbol{\nu} + \Phi(\nu)(\hat{\boldsymbol{\phi}} + \boldsymbol{\beta}(\boldsymbol{z}) - \tilde{\boldsymbol{\phi}})), \tag{2.76}$$

where $\dot{\boldsymbol{\alpha}}$ is defined as in (2.3.1).

Consequently, the adaptation law and control law are chosen as

$$\dot{\hat{\boldsymbol{\psi}}} = -\frac{\partial \boldsymbol{\beta}}{\partial \boldsymbol{z}_1^\top}\dot{\boldsymbol{z}}_1 - \frac{\partial \boldsymbol{\beta}}{\partial \boldsymbol{z}_2^\top}(\boldsymbol{\tau} - \boldsymbol{M}\dot{\boldsymbol{\alpha}} + \boldsymbol{R}^\top \boldsymbol{w}_{\boldsymbol{\delta}} - \boldsymbol{C}(\boldsymbol{\nu})\boldsymbol{\nu} \tag{2.77}$$

$$+ \boldsymbol{g}(\boldsymbol{\nu})\boldsymbol{\nu} + \Phi(\nu)(\hat{\boldsymbol{\phi}} + \boldsymbol{\beta}(\boldsymbol{z}) - \tilde{\boldsymbol{\phi}})) \tag{2.78}$$

$$\boldsymbol{\tau} = \boldsymbol{M}\dot{\boldsymbol{\alpha}} + \boldsymbol{C}(\boldsymbol{\nu})\boldsymbol{\nu} - \boldsymbol{g}(\boldsymbol{\nu})\boldsymbol{\nu} - \boldsymbol{K}_2(\cdot)\boldsymbol{z}_2 - \Phi(\nu)(\hat{\boldsymbol{\phi}} + \boldsymbol{\beta}(\boldsymbol{z})). \tag{2.79}$$

The design function $\boldsymbol{\beta}$ partial derivatives are then selected as

$$\frac{\partial \boldsymbol{\beta}}{\partial \boldsymbol{z}_1^\top} = 0 \tag{2.80}$$

$$\frac{\partial \boldsymbol{\beta}}{\partial \boldsymbol{z}_2^\top} = \boldsymbol{\Gamma}\boldsymbol{\Phi}(\boldsymbol{\nu})^\top, \tag{2.81}$$

which is then inserted in (2.78)-(2.79), giving the control and adaptive laws

$$\dot{\hat{\boldsymbol{\psi}}} = -\boldsymbol{\Gamma}\boldsymbol{\Phi}(\boldsymbol{\nu})^\top(\boldsymbol{\tau} - \boldsymbol{M}\dot{\boldsymbol{\alpha}} + \boldsymbol{R}^\top \boldsymbol{w}_{\boldsymbol{\delta}} - \boldsymbol{C}(\boldsymbol{\nu})\boldsymbol{\nu} + \boldsymbol{g}(\boldsymbol{\nu})\boldsymbol{\nu} + \boldsymbol{\Phi}(\boldsymbol{\nu})(\hat{\boldsymbol{\phi}} + \Gamma\Phi(\nu)^\top \boldsymbol{z}_2) \tag{2.82}$$

$$\boldsymbol{\tau} = \boldsymbol{M}\dot{\boldsymbol{\alpha}} + \boldsymbol{C}(\boldsymbol{\nu})\boldsymbol{\nu} - \boldsymbol{g}(\boldsymbol{\nu})\boldsymbol{\nu} - \boldsymbol{K}_2(\cdot)\boldsymbol{z}_2 - \boldsymbol{\Phi}(\boldsymbol{\nu})(\hat{\boldsymbol{\phi}} + \Gamma\boldsymbol{\Phi}(\boldsymbol{\nu})^\top \boldsymbol{z}_2). \tag{2.83}$$

To show the stability of the I&I - NP-NV adaptive controller, a quadratic Lyapunov function candidate is proposed

$$V = \frac{1}{2}\boldsymbol{z}_1^\top \boldsymbol{z}_1 + \frac{1}{2}\boldsymbol{z}_2^\top \boldsymbol{M}\boldsymbol{z}_2 + \frac{1}{2}\tilde{\boldsymbol{\phi}}^\top \tilde{\boldsymbol{\phi}} \tag{2.84}$$

By differentiating V for time we get

$$\dot{V} = \boldsymbol{z}_1^\top \boldsymbol{M}\dot{\boldsymbol{z}}_1 + \boldsymbol{z}_2^\top \boldsymbol{M}\dot{\boldsymbol{z}}_2 + \tilde{\boldsymbol{\phi}}^\top \dot{\tilde{\boldsymbol{\phi}}} \tag{2.85}$$

$$= -\boldsymbol{z}_1^\top \boldsymbol{K}_1(\cdot)\boldsymbol{z}_1 + \boldsymbol{z}_1^\top(\boldsymbol{K}_2 \cdot \boldsymbol{z}_2 + \boldsymbol{\Phi}(\boldsymbol{\nu})\tilde{\boldsymbol{\phi}}) - \tilde{\boldsymbol{\phi}}^\top \Gamma\boldsymbol{\Phi}(\boldsymbol{\nu})^\top \boldsymbol{\Phi}(\boldsymbol{\nu})) < 0 \tag{2.86}$$

negative definite.

2.4 The 4-corner Maneuvering Test

The main objective of the control system is to ensure $\tilde{\boldsymbol{\eta}}(t) \triangleq \boldsymbol{\eta}(t) - \boldsymbol{\eta}_t(t) \to \boldsymbol{0}$ when $t \to \infty$. Furthermore, it is desirable to analyze the performance of the control system

during different modes of motion. For this reason, a test compromised of different motions will be utilized, a "4-corner test", inspired by [5]. The 4-corner test is shown in Figure 2.7. In this test, the ship is moved to 4 different set-points, or "corners" of a square, testing different modes of motion required of a autonomous ship. The movements in the 4-corner test are:

- Position change $2\,(m)$ straight North: positive surge-only movement.
- Position change $2\,(m)$ straight East: sway-only movement in starboard direction.
- Heading change $45\,(deg)$ clockwise: pure yaw motion, "turning test", while holding position.
- Position change $2\,(m)$ straight South: coupled surge-sway movement while holding heading degree.
- Position change $2\,(m)$ straight West and heading change $45\,(deg)$ counterclockwise: coupled surge-sway-yaw movement.

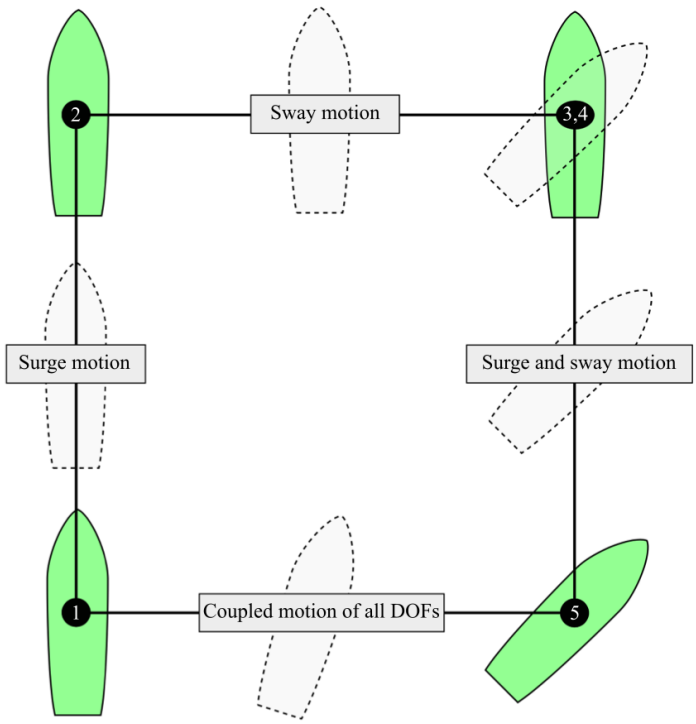

Figure 2.7: 4-corner test, modified from [5]

2.5 Performance Metrics

For analyzing performance of control systems, performance metrics are a useful tool when comparing different types of controllers. For this thesis, the scaled norm of the pose control $\boldsymbol{z}_1$ error will be used as the error in the metric calculation. The pose control error contains values of different units, metres and radians, thus the normalized pose error $\bar{z}_1$ is defined on the intervals of the operational space in the 4-corner test [25]. For the position errors, this interval is $[-2, 2]$ and for heading the interval is $[-\frac{\pi}{4}, \frac{\pi}{4}]$. Dividing the pose errors by 4 and the heading error by $\frac{\pi}{2}$, resulting in the normalized pose error signal

$$\bar{\boldsymbol{z}}_1 = [\frac{z_{1,x}}{4}, \frac{z_{1,y}}{4}, \frac{z_{1,\psi}}{\pi/2}]^\top, \tag{2.87}$$

and the scaled norm

$$e = \sqrt{\bar{\boldsymbol{z}}_1^\top \bar{\boldsymbol{z}}_1}, \tag{2.88}$$

It should be noted that this is not an exclusive definition, as the error can be defined multiple ways, including cross-track and velocity-tracking error. In this thesis, 3 different types of performance metric will be used; integral of the absolute error (IAE), integral of the absolute error multiplied by energy consumption (IAEW) and lastly the integral of the absolute differentiated control (IADC).

The IAE metric is an unweighted integral of the error over time, and is a simple measure on how well the controller holds the desired pose throughout the motions.

$$IAE(t) = \int_0^t |e(\gamma)| \, d\gamma. \tag{2.89}$$

In the IAEW metric, the power consumption $P = \left|\left|\boldsymbol{\nu}^\top \boldsymbol{\tau}\right|\right|$ is used to scale the IAE-metric, and takes the energy consumption, and consequently, the energy efficiency into account.

$$IAEW(t) = \int_0^t |e(\gamma)| \, d\gamma \int_0^t P(\gamma) d\gamma. \tag{2.90}$$

Finally, it is desirable to evaluate the dynamic behaviour of the commanded input, which is relevant to take into account when the desire is to reduce wear and tear on actuators. The IADC-metric defined as in [25] as

$$IADC(t) = \int_{t_0}^t |\dot{\bar{\tau}}(\gamma)| \, d\gamma, \tag{2.91}$$

with $\bar{\tau}(t) = \sqrt{\boldsymbol{\tau}^\top \boldsymbol{\tau}}$, and where the variable $\dot{\bar{\tau}}$ is computed using numerical derivation.

Chapter 3

Simulation Results

3.1 Simulator Design

Frequently used in control theory, computer simulation is a powerful tool utilized for a variety of purposes. It can be used during development of control schemes, during tuning and implementation, and to verify results. As an example for this thesis, running simulations of a control implementation to verify how the control input performs in terms of magnitude and rate is recommended to ensure physically viable control signals and to protect the actuator system from excessive strain. In order to achieve reliable results from simulations, the simulator should be implemented in such a way that it represents the real world conditions as close as possible, including noise, disturbances and other environmental influences. In the matter of this thesis, the goal of the simulator implementation is to approximate the conditions in the lab. A block diagram of the simulator is shown in Figure 3.1. The differential equation solver used in simulations is the same as in the lab, the Runge-Kutta solver.

To implement the simulator, a mathematical model of the system is needed. In this thesis the system model from Chapter 2.1 is implemented as the function

$$\dot{\boldsymbol{\nu}} = \boldsymbol{M}^{*-1}(\boldsymbol{\tau}^* - \boldsymbol{C}^*\boldsymbol{\nu} - \boldsymbol{D}^*\boldsymbol{\nu}), \tag{3.1}$$

where the model matrices $\boldsymbol{M}^*, \boldsymbol{C}^*$ and $\boldsymbol{D}^*$ are given by the uncertainty relation between real and considered model in (2.23). The variable $\dot{\boldsymbol{\nu}}$ is integrated to get velocity measurement $\boldsymbol{\nu}$, and rotated about z then integrated to get position $\boldsymbol{\eta}$. In addition to model uncertainty, the uncertainty associated with the actuators is parameterized as $\boldsymbol{\tau}^* = \rho\boldsymbol{\tau}$, where $\rho > 0$ is the actuator uncertainty as described in Chapter 2.

It is assumed that noise is present in the position and velocity measurements used for feedback. In order to replicate the same noise in the simulator, an analysis of the noisy data is needed. A sample of position and velocity data from an earlier experiment in the lab

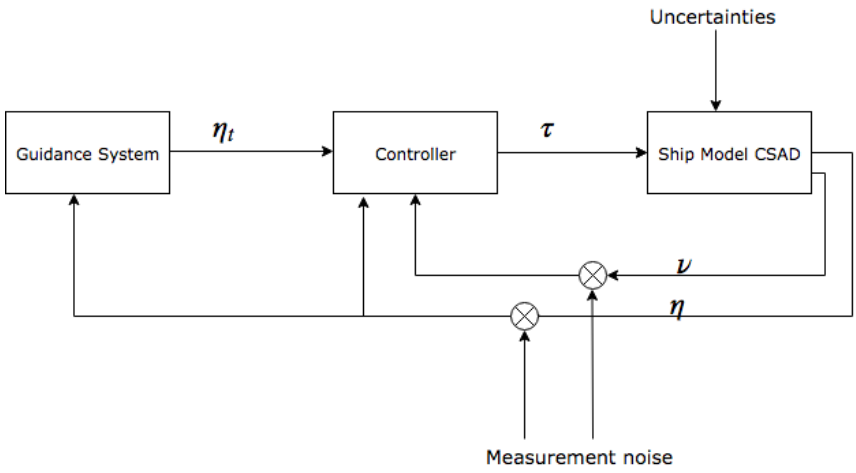

Figure 3.1: Simulator block diagram

is used for the analysis. By examining the Power Spectral Density (PSD) of the position signal shown in Figure 3.2, one can see that the noise is most significant in the frequency range close to 20Hz. As the aim is to replicate the conditions in the lab, a similar noise profile should be introduced to the simulator measurements. By bandpass-filtering band-limited white noise and adding it to band-limited white noise of lower power, the noise profile is approximately recreated, as seen in Figure 3.2. The PSD is found using the Fast-Fourier-Transform (FFT).

The power of the white noise used is displayed in Table 3.1. Note that the power of the noise in the y-measurement is set higher than in the x-measurement. This is due to the setup of the positioning system in the lab, resulting in more noise for the y-measurement.

	Value
Noise $\boldsymbol{\eta}_{filtered}$	$[1.5, 6.0, 1.5]10^{-7}$
Noise $\boldsymbol{\eta}_{added}$	$[0.75, 3.0, 0.75]10^{-7}$
Noise $\boldsymbol{\nu}_{filtered}$	$[0.1, 0.24, 0.48]10^{-6}$
Noise $\boldsymbol{\nu}_{added}$	$[0.05, 0.05, 0.25]10^{-7}$
δ	1.5
σ	2
ρ	0.8

Table 3.1: Noise and model uncertainty parameters in the simulator

The implemented parametrization of uncertainties can be seen in the full model implementation shown in Appendix.

Figure 3.3 shows how the measurement noise is introduced in the simulator. The same structure is used for the velocity measurement noise, using the noise power values in Table

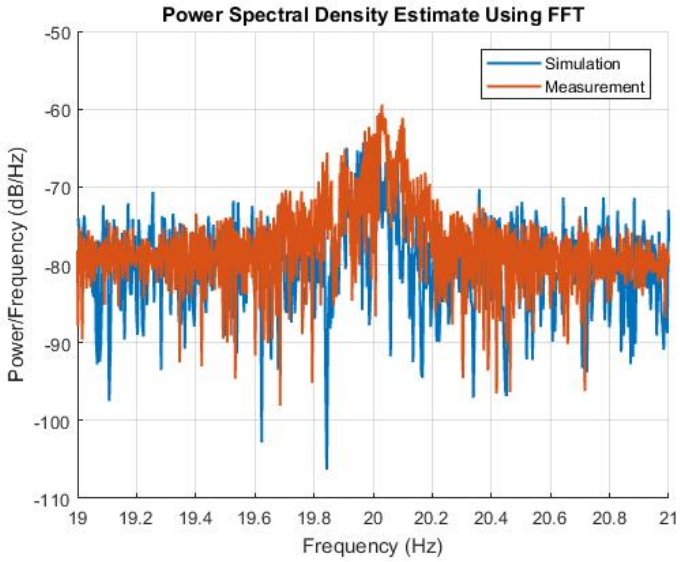

Figure 3.2: Reconstructed noise profile for the position measurements

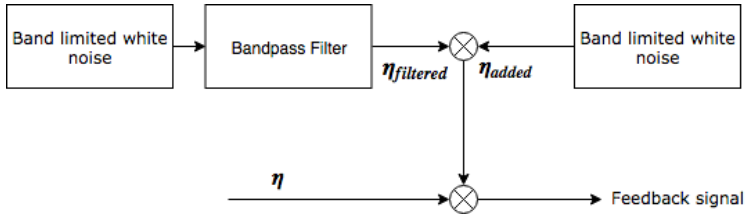

Figure 3.3: Block diagram of noise implementation in the simulator

3.1.

3.2 Results

To have a basis of comparison in order to evaluate how the adaptive schemes handle the uncertainties and disturbances in the simulator, a simulation of the nominal NP-NV controller is run under identical conditions as the adaptive versions. The simulations in this section are performed with the parameter values displayed in Table 3.2.

	$\mathcal{L}_1$	I&I
$\boldsymbol{\Gamma}_1$	diag($[0.08, 0.08, 0.0698]$)	$-\|\|-$
$\boldsymbol{\Gamma}_2$	diag($[0.2, 0.2, 0.1745]$)$\boldsymbol{M}$	$-\|\|-$
$\Delta_{\tilde{p}}$	0.5	$-\|\|-$
$\Delta_{\tilde{\psi}}$	0.5	$-\|\|-$
$\Delta_{\tilde{v}}$	0.7	$-\|\|-$
$\Delta_{\tilde{r}}$	1	$-\|\|-$
$\boldsymbol{L_1}$	$\boldsymbol{I}(2\pi)^2$	$-$
$\boldsymbol{L_2}$	$\boldsymbol{I}(4.8\pi)$	$-$
γ_{w_δ}	$(20\pi)^2/4$	$-$
$\boldsymbol{\Gamma}_k$	$-$	diag([6,3,6,6,6,3, 6, 6,0.3,0.3,0.3])
$\boldsymbol{K}$	diag($[4, 3, 2]$)	$-\|\|-$
$\boldsymbol{sat_m}$	$[2, 1.5, 1]$	$-\|\|-$
$\boldsymbol{sat_r}$	$[1.9, 1.1, 0.8]$	$-\|\|-$

Table 3.2: Control gains used in simulations

The following adaptive simulations presented are

- $\mathcal{L}$ adaptive control,4-corner unconstrained.
- $\mathcal{L}$ àdaptive control with MRS, 4-corner.
- I&I adaptive control, 4-corner unconstrained.
- I&I adaptive control with MRS, 4-corner.

3.2.1 $\mathcal{L}_1$ Adaptive Control Simulations

As mentioned earlier, the name of the adaptive control concept comes from the $\mathcal{L}_1$ norm from the stability. In this thesis, for simplicity the term $\mathcal{L}_1$ refers to the adaptive control, not the norm.

$$\boldsymbol{\tau} = \boldsymbol{M}\dot{\boldsymbol{\alpha}} + (\boldsymbol{C} + \boldsymbol{D})\boldsymbol{\alpha} - \boldsymbol{K}_2\boldsymbol{z}_2 - \hat{\boldsymbol{w}}_{\boldsymbol{\delta}}$$
$$\dot{\hat{\boldsymbol{w}}}_{\boldsymbol{\delta}} = -\gamma_{w_\delta}\boldsymbol{R}\tilde{\boldsymbol{\nu}}$$

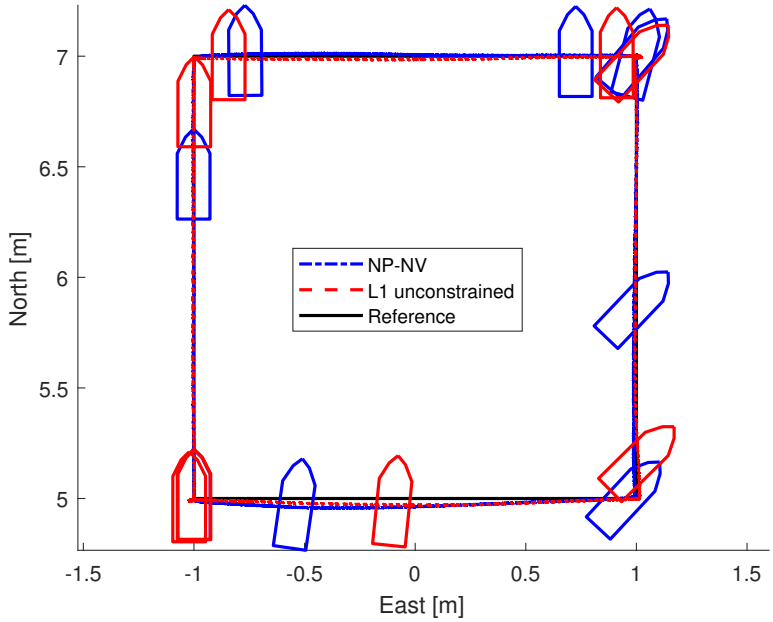

Figure 3.4: Unconstrained $\mathcal{L}_1$ simulation, 4-corner test.

Figure 3.4 displays the surface plot of the simulated $\mathcal{L}_1$ unconstrained adaptive control together with the nominal NP-NV controller. The adaptive controller follows the reference track well. Path following is improved compared to the nominal NP-NV, and pose error metric IAE is reduced which can seen from the metric plot in Fig 3.5.

It can be read from the metrics the $\mathcal{L}_1$ adaptive control is faster around the 4corner test, but that the improvement in pose tracking results in higher energy IAEW metric and control rate IADC. It can be assumed that the increased IADC metrics comes from the property of the adaptive scheme being more susceptible to measurement noise. Figure 3.6 illustrates this, as it is seen that the same introduced signal noise affects $\mathcal{L}_1$ adaptive control more than the nominal NP-NV controller.

The simulated surface plot of $\mathcal{L}_1$ - MRS is shown in Figure 3.7. The results show that path tracking performance is not reduced by adding the MRS-model. Furthermore, as can be seen in the metric plot in Figure 3.8, the IADC metric is significantly reduced, an effect that points to a smoother operation with less actuator wear.

From the control signal plot in Figure 3.9 it can be seen that the fitting of the MRS model leads to longer control transients, more in tune with the actual actuator system, which naturally cannot change thrust instantly.

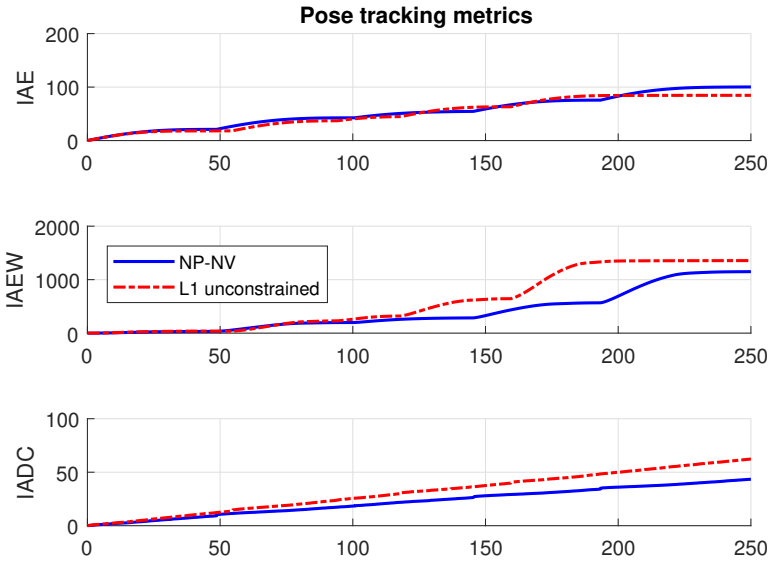

Figure 3.5: Unconstrained $\mathcal{L}_1$ simulation, Pose error metrics.

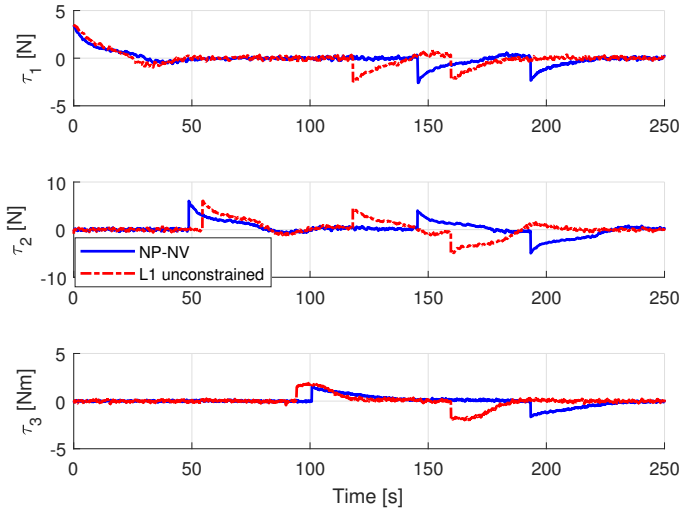

Figure 3.6: Unconstrained $\mathcal{L}_1$ simulation, Control inputs.

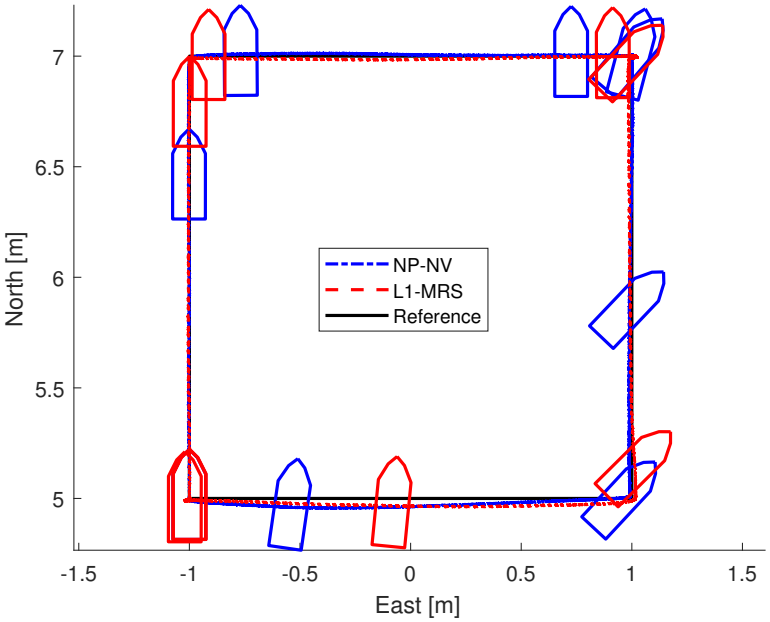

Figure 3.7: $\mathcal{L}_1$ with MRS simulation, 4-corner test.

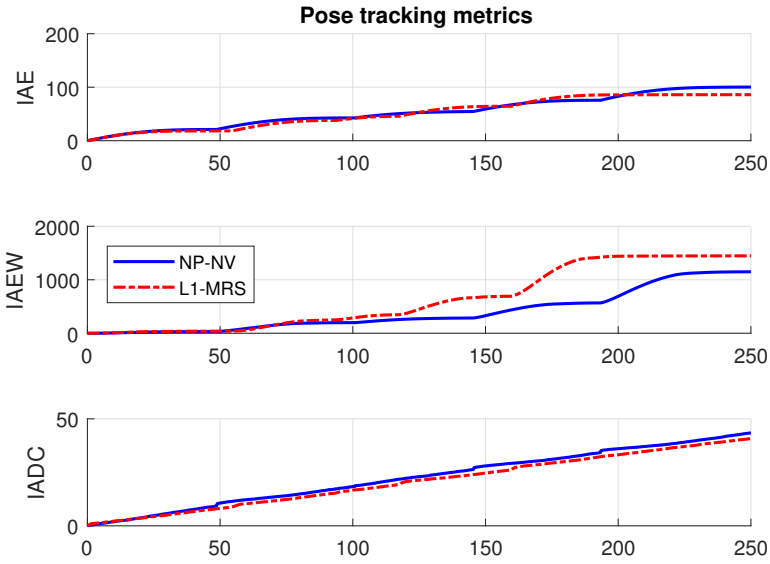

Figure 3.8: $\mathcal{L}_1$ with MRS simulation, Pose error metrics.

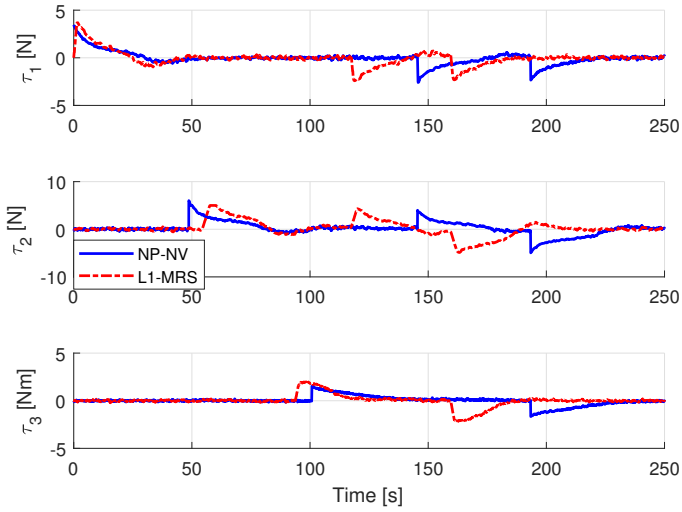

Figure 3.9: $\mathcal{L}_1$ with MRS simulation, Control inputs.

3.2.2 Immersion and Invariance Adaptive Control Simulations

$$\boldsymbol{\tau} = \boldsymbol{M}\dot{\boldsymbol{\alpha}} + \boldsymbol{C}(\boldsymbol{\nu})\boldsymbol{\nu} - \boldsymbol{g}(\boldsymbol{\nu})\boldsymbol{\nu} - \boldsymbol{K}_2(\cdot)\boldsymbol{z}_2 - \boldsymbol{\Phi}(\boldsymbol{\nu})(\hat{\boldsymbol{\phi}} + \Gamma_k \boldsymbol{\Phi}(\boldsymbol{\nu})^\top \boldsymbol{z}_2)$$
$$\dot{\hat{\boldsymbol{\psi}}} = -\boldsymbol{\Gamma_k}\boldsymbol{\Phi}(\boldsymbol{\nu})^\top(\boldsymbol{\tau} - \boldsymbol{M}\dot{\boldsymbol{\alpha}} + \boldsymbol{R}^\top \boldsymbol{w_\delta} - \boldsymbol{C}(\boldsymbol{\nu})\boldsymbol{\nu} + \boldsymbol{g}(\boldsymbol{\nu})\boldsymbol{\nu} + \boldsymbol{\Phi}(\boldsymbol{\nu})(\hat{\boldsymbol{\phi}} + \Gamma_k \Phi(\nu)^\top \boldsymbol{z}_2).$$

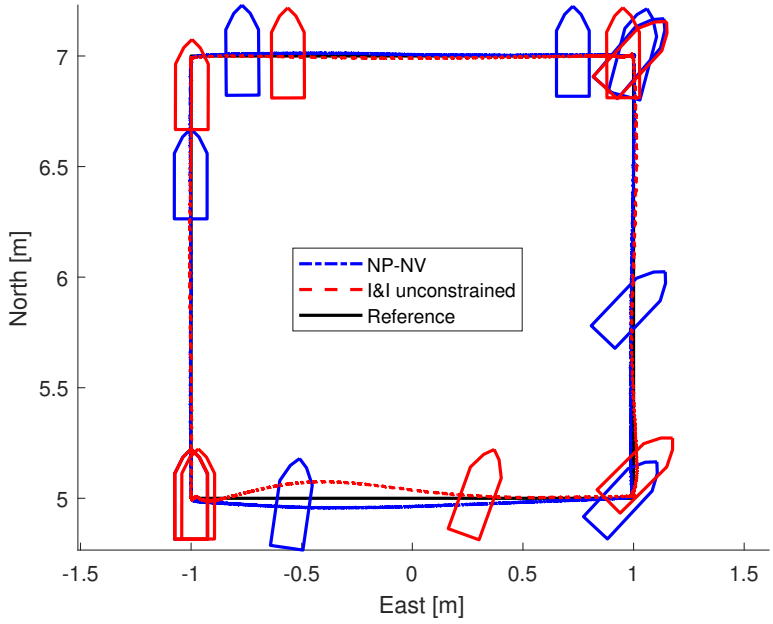

Figure 3.10: Unconstrained I&I simulation, 4-corner test.

Figure 3.10 shows the surface plot of the unconstrained I&I adaptive controller. The ship follows the path nicely, but with somewhat drift at the final movement ($5 \rightarrow 1$). However, this drift does not reflect in the overall pose control error, as seen in Table 3.3 and Figure 3.11. This is most likely due to how the error is weighed, as the I&I tries to reduce heading error early, while moving in sway to the final corner.

As was the case for the $\mathcal{L}_1$ adaptive control, I&I completes the 4-corner test in shorter time than the nominal NP-NV, but at the cost of higher energy consumption and control rate. The IADC metric, similar to $\mathcal{L}_1$ adaptive, is higher compared to nominal control due to the adaptive schemes inherent susceptibility to measurement noise, although it seems that I&I is less affected than $\mathcal{L}_1$.

Figure 3.13 shows the MRS fitted I&I simulation surface plot. It would seem that the cascaded system becomes oscillated due to the limitations of the MRS model. Comparing with the control output of the unconstrained I&I in Figure 3.12, it can be seen that the desired output, especially in sway, is far beyond the actual limitation of the ship. So when the adaptive controller is limited by MRS, this leads to the oscillations when the

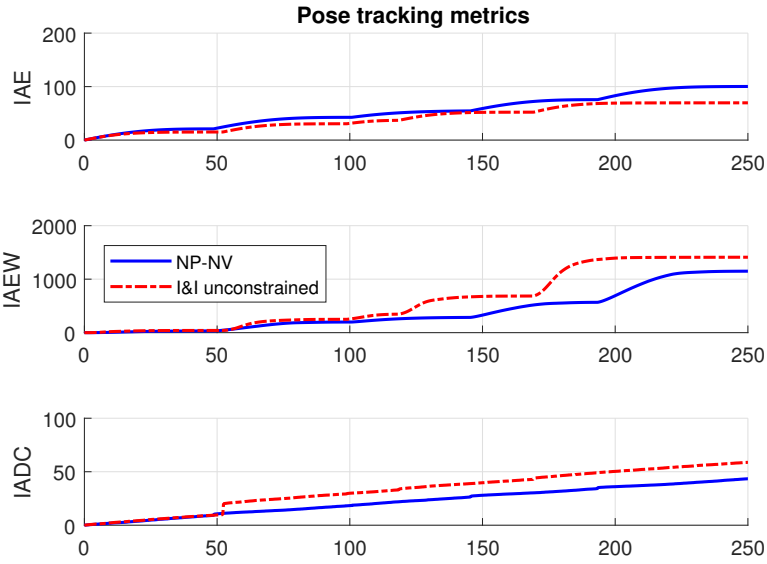

Figure 3.11: Unconstrained I&I simulation, Pose error metrics.

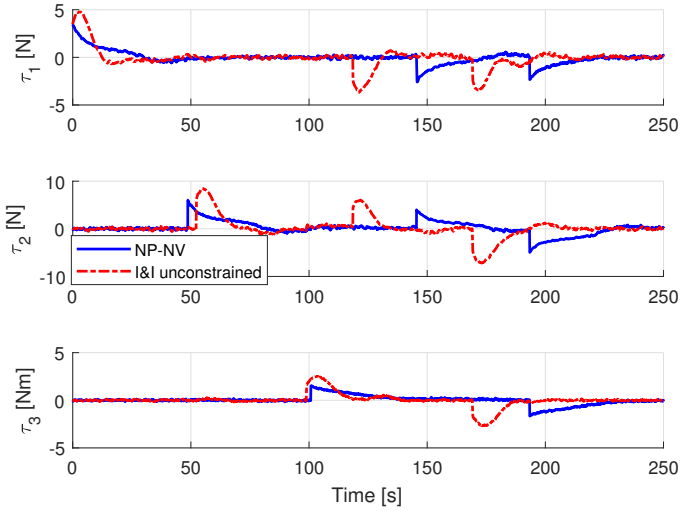

Figure 3.12: Unconstrained I&I simulation, Control inputs.

controller is not permitted to output the commanded control signal. Figure 3.14 displays the evolution of the performance metrics.

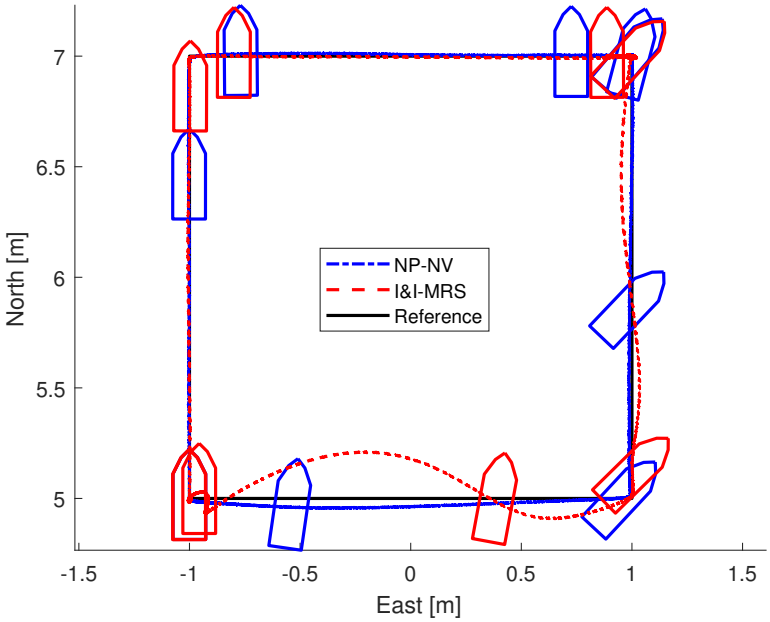

Figure 3.13: I&I with MRS simulation, 4-corner test.

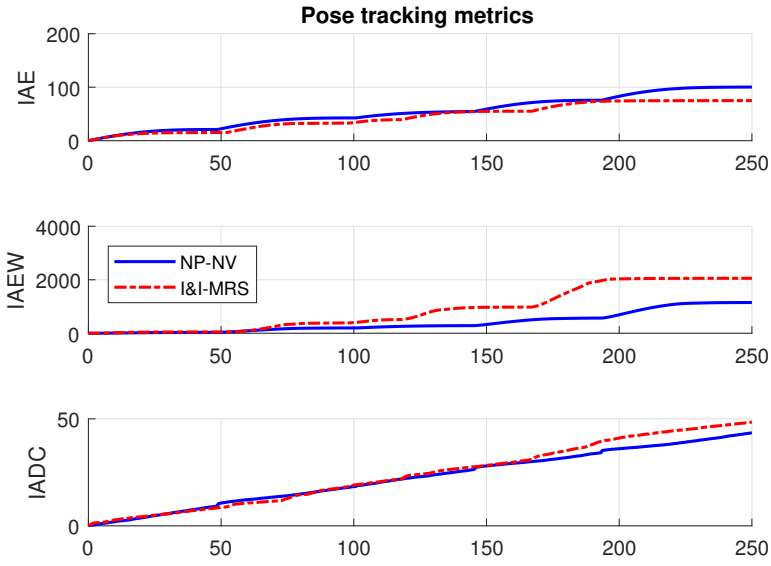

Figure 3.14: I&I with MRS simulation, Pose error metrics.

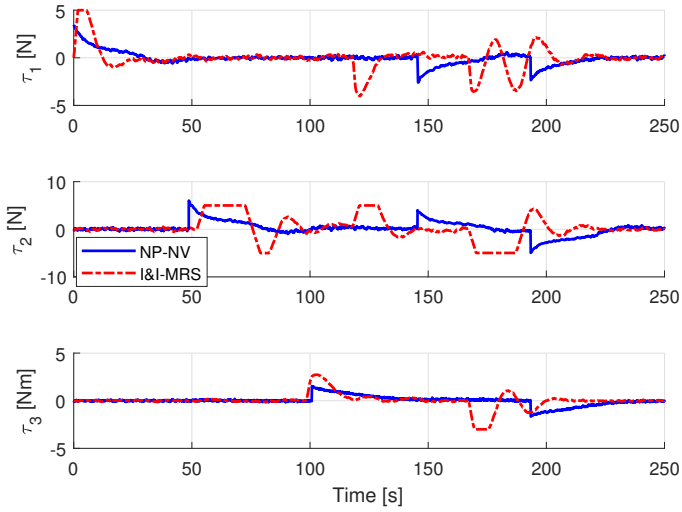

Figure 3.15: I&I with MRS simulation, Control inputs.

3.2.3 Summary

Controller	IAE	IAEW	IADC
$NP-NV$	101	**1149**	43
$\mathcal{L}_1 unconstr.$	85	1352	62
$\mathcal{L}_1 MRS$	86	1442	**41**
$I\&I unconstr.$	**70**	1410	61
$I\&I MRS.$	75	2052	46

Table 3.3: End values of simulated performance metrics - pose error

In Table 3.3, the final maximum values of performance metrics for the simulated control implementations are displayed. The metric values are rounded to the nearest integer for readability, and the lowest values are marked in bold.

3.3 Discussion

Even though effort has been put into replicating the real world conditions of the lab in the simulator, it will never fully represent all aspects of the conditions. Even so, the simulation results contribute as a preliminary step in testing that the control implementations work satisfactory to a degree, and form a basis on which to move to laboratory testing. As can be seen in Table 3.3, all the adaptive controllers reduce the overall control error, but at the cost of energy efficiency. The improvements can be accredited to how the adaptive controllers approximate the real model, and so improves on the set model of the nominal NP-NV controller the adaptive schemes has been fitted to.

It can also be seen, especially for the $\mathcal{L}_1$, that the MRS model significantly reduces the control rate, and thus wear & tear of actuators. This is desirable when moving from simulations to laboratory testing in order to reduce risk of breakage on the scale model. It can also be noted that the $\mathcal{L}_1$ is less affected by the MRS in terms of IAE and IAEW, whereas the I&I suffers relatively more. The simulations also prove as a way to validate the choice of gain parameters, as the selected values give a fairly realistic behaviour and thus can be safely tested in the lab, as will be presented in the next chapter.

3.3.1 Error Sources

In the simulator, noise approximations are introduced to mimic lab behavior. While this contributes to replicate lab conditions, more realistic measures could introduced, such as Hardware-In-the-Loop (HIL). This, however, is outside the scope of this thesis.

Furthermore, the choice of uncertainty parametrization is based on a combination of intuitively selection and simulating the results. It follows that this relationship between the ”real” and the considered model is an approximation, which does not represent the uncertainty perfectly, but is a fair assumption.

Chapter 4

Experimental Results

4.1 Experimental Setup

4.1.1 Marine Cybernetics Laboratory

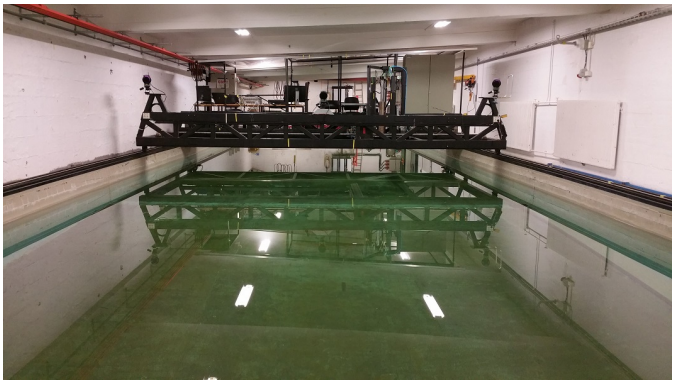

Figure 4.1: MC-lab basin (Picture from MC-Lab Handbook)[6]

The Marine Cybernetics laboratory (MC-lab) is a small wave basin laboratory with the Department of Marine Technology at NTNU. Due to its relatively small size and advanced instrumentation package, the facility is especially suited for tests of motion control system for marine vessels, but is also suitable for more specialized hydrodynamic tests due to the advanced towing carriage, which has capability for precise movement of models up to six degrees-of-freedom for both surface ships and submersibles. The basin measures [40x6.45x1.5] meter in length, width and depth, displayed in Figure 4.1.

4.1.2 Hardware

The lab is equipped with a Qualisys QTM (Qualisys Track Manager) system for motion capture and measurements, which is used for position feedback to the on-board control system of scale models. Input to the Qualisys system comes from 3 Oqus highspeed Infrared cameras, which tracks the IR reflector orbs fitted on vessel models in the basin. The Qualisys QTM system is installed on a dedicated workstation, using P2P communication with the Oqus cameras.

Experiments can be fully supervised from a control room equipped with a dedicated computer for the QTM system and TV connected to 2 high-resolution video-cameras. The block diagram of the control system can be seen in Figure 4.2.

The internal communications in the lab is done over IP on a dedicated WLAN network, allowing wireless control of the model vessels as well as transfer of data.

The ship model is equipped with a National Instrument CompactRIO (cRIO) embedded computer system for control computation.

4.1.3 Software

To communicate with the ship, the laptops are fitted with a substantial software suite, which includes LabVIEW Full Development System, MATLAB with Simulink package as well as the National Instruments Veristand complete software suite. The full list of dependency software is listed in the MC-lab Handbook [6].

Although the Qualisys system supplies position measurements, it does not compute the velocity feedback signals needed for the control implementations in this thesis. Instead, using the position measurements, the on-board computer estimates BODY-fixed velocities for control feedback with an applied derivative filter implemented in the system block, as seen in Figure 4.2. While the controller runs as 100Hz, it takes inputs and produces the output signal at 10Hz.

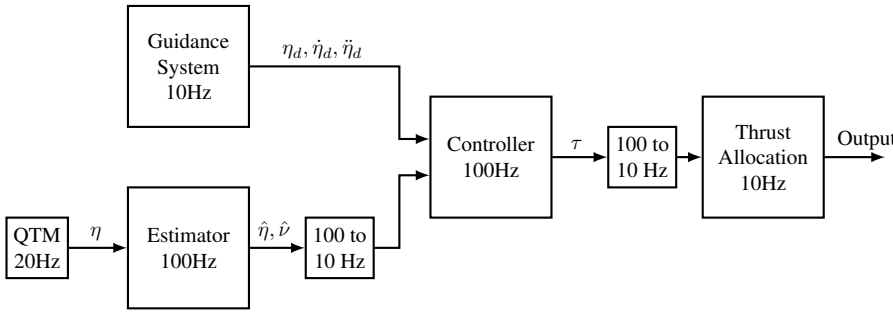

Figure 4.2: MC-Lab Simulink setup

4.2 Lab Session 1 - March 2018

In this section, results from scale model experiments are presented. The outline of the ship is scaled by 1:6 in the 4-corner plots to better display the ship behaviour. To have a basis of comparison for the adaptive techniques in the laboratory experiments, an initial 4-corner test of the CSAD is done with the nonlinear pose and velocity feedback controller NP-NV as described in Chapter 2. The 4-corner test for NP-NV controller is shown in Figure 4.3.

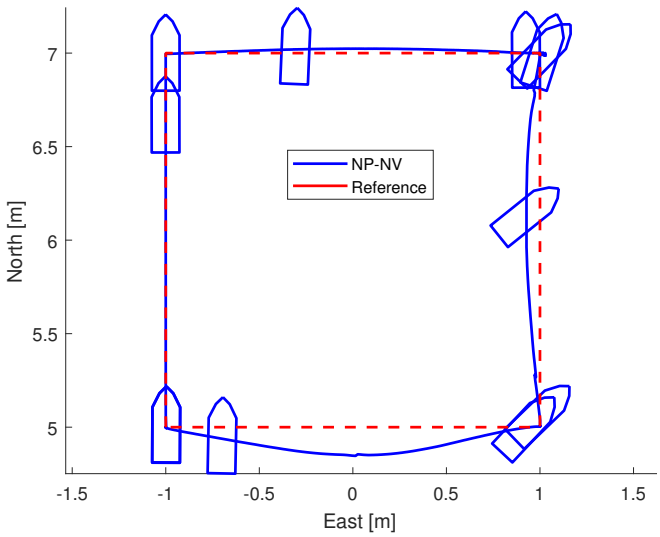

Figure 4.3: Unconstrained NPNV 4-corner test.

Table 4.1 displays the control and parameter gains used in Lab session 1.

In lab session 1, the following adaptive control experiments are performed

- $\mathcal{L}$ adaptive control,4-corner unconstrained.
- $\mathcal{L}$ adaptive control,4-corner unconstrained.
- $\mathcal{L}$ àdaptive control with MRS, rate constraints factored by 1.2, 4-corner.
- $\mathcal{L}$ àdaptive control with MRS, rate constraints factored by 1.5, 4-corner.
- I&I adaptive control, 4-corner unconstrained.
- I&I adaptive control with MRS, 4-corner.

	$\mathcal{L}_1$	I&I
$\boldsymbol{\Gamma}_1$	$\text{diag}([0.08, 0.08, 0.0698])$	$-\|\|-$
$\boldsymbol{\Gamma}_2$	$\text{diag}([0.2, 0.2, 0.1745])\boldsymbol{M}$	$-\|\|-$
$\Delta_{\tilde{p}}$	0.5	$-\|\|-$
$\Delta_{\tilde{\psi}}$	0.5	$-\|\|-$
$\Delta_{\tilde{v}}$	0.7	$-\|\|-$
$\Delta_{\tilde{r}}$	1	$-\|\|-$
$\boldsymbol{L_1}$	$I(2\pi)^2$	$-$
$\boldsymbol{L_2}$	$I(4.8\pi)$	$-$
γ_{w_δ}	$(20\pi)^2/4$	$-$
$\boldsymbol{\Gamma}_k$	$-$	diag([6,3,6,6,6,3,6,6,0.3,0.3,0.3])
$\boldsymbol{K}$	$\text{diag}([4, 3, 2])$	$-\|\|-$
$\boldsymbol{sat_m}$	$[2, 1.5, 1]$	$-\|\|-$
$\boldsymbol{sat_r}$	$[1.9, 1.1, 0.8]$	$-\|\|-$

Table 4.1: Control parameters for lab session 1

4.2.1 $\mathcal{L}_1$ Adaptive Control Experiments

The following control and adaptation law is used in the following experiments:

$$\boldsymbol{\tau} = \boldsymbol{M}\dot{\boldsymbol{\alpha}} + (\boldsymbol{C} + \boldsymbol{D})\boldsymbol{\alpha} - \boldsymbol{K}_2\boldsymbol{z}_2 - \hat{\boldsymbol{w}}_{\boldsymbol{\delta}}$$
$$\dot{\hat{\boldsymbol{w}}}_{\boldsymbol{\delta}} = -\gamma_{w_\delta}\boldsymbol{R}\tilde{\boldsymbol{\nu}}$$

Figure 4.4 shows the path plot of the unconstrained $\mathcal{L}_1$ cascaded controller. It can be seen that the controller follows the reference path better than the nominal NP-NV, especially for the $(4 \rightarrow 5)$ backwards motion in Figure 2.7 where it almost keeps the pose perfectly. This is most likely due to the adaptation compensating for uncertainties in the model during motion while keeping the heading at 45^o.

The evolution of the performance metrics for pose error is shown in Figure 4.5. One can see that the $\mathcal{L}_1$ controller performs the 4 corner faster than the NP-NV, and with lower pose error (IAE). However, the energy consumption is significantly higher, due to the aggressive nature of the adaptive scheme. This is especially significant for the coupled motion in $(5 \rightarrow 1)$, where the controller seeks to reduce control error in both sway and yaw simultaneously.

Figure 4.6 displays the commanded control input in all degrees of freedom. There are significant spikes in the control input for the $\mathcal{L}_1$, which can be attributed not only to the aggressive adaptation, but also to the fact that the adaptation is more susceptible to errors in the measurements due to the high-gain state predictor.

In Figure 4.7, the $\mathcal{L}_1$ has been run with a Low-pass filter fitted to the control input, cut-off frequency at 100 Hz. The desired goal was to reduce noice in the commanded input to the ship. The path plot, as well as the IAE shows that the LP did not reduce path tracking precision. The LP filter did not reduce the noise in the control signal seen in Figure 4.9.

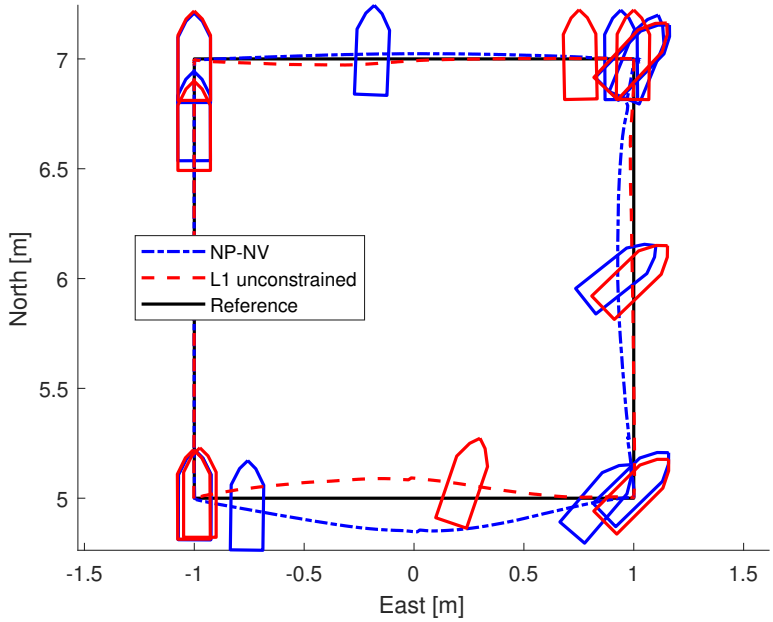

Figure 4.4: Unconstrained $\mathcal{L}_1$ 4-corner test.

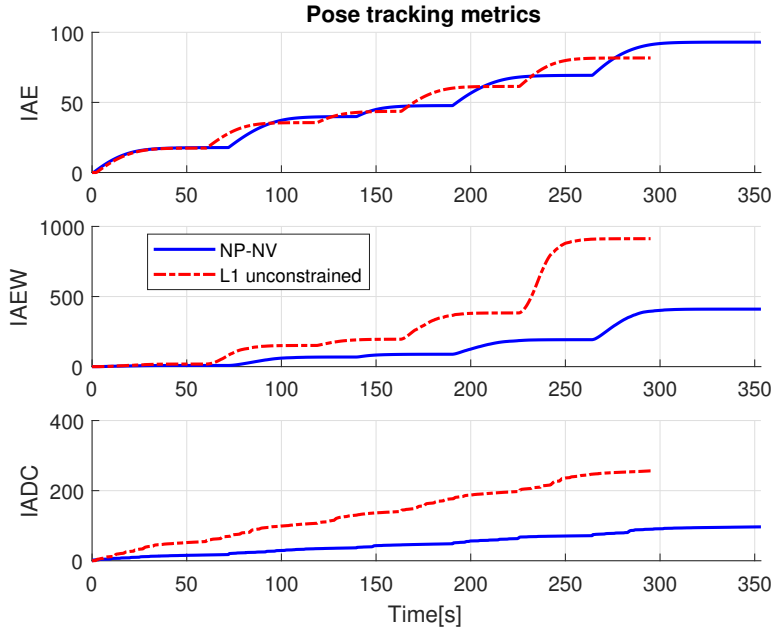

Figure 4.5: Unconstrained $\mathcal{L}_1$, Pose error metrics.

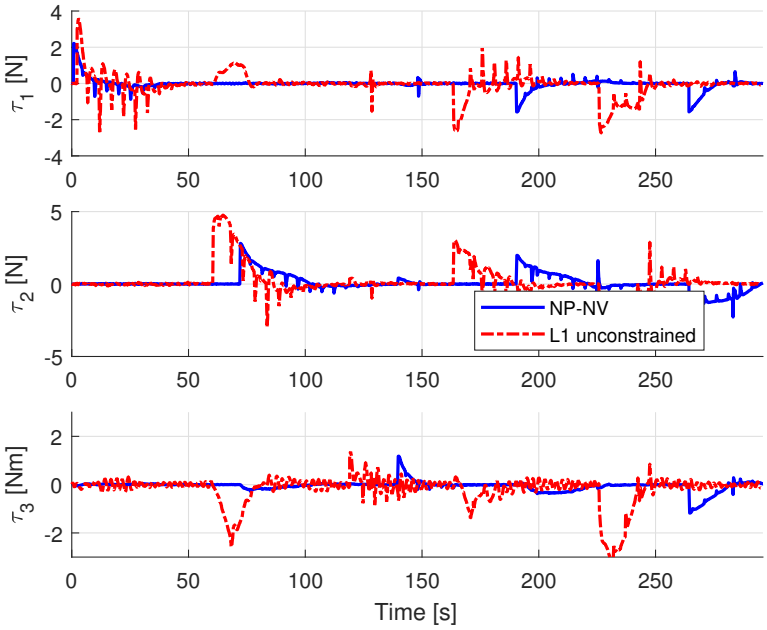

Figure 4.6: Unconstrained $\mathcal{L}_1$, Control inputs.

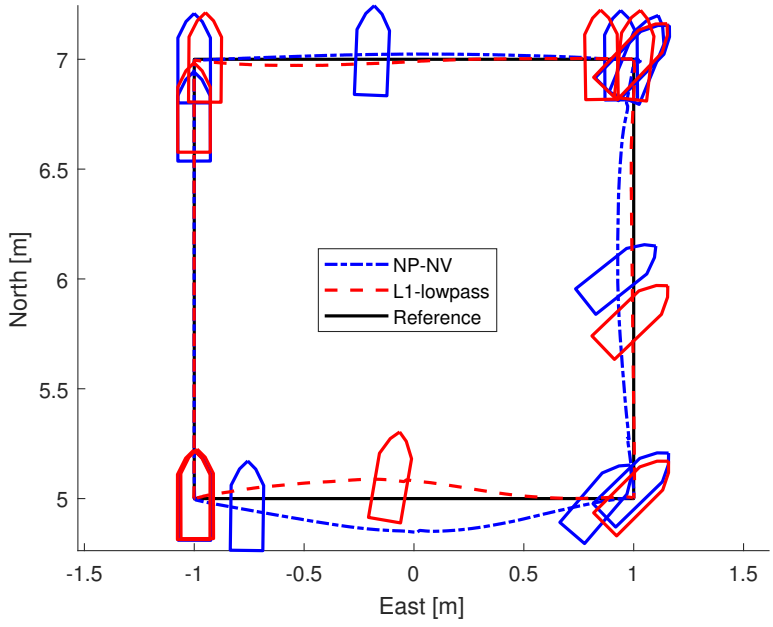

Figure 4.7: Lowpass filtered $\mathcal{L}_1$ 4-corner test.

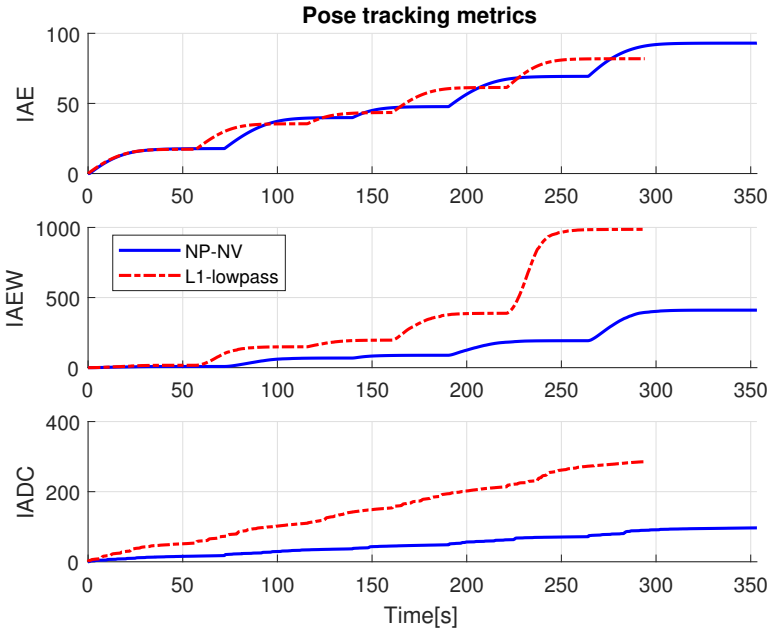

Figure 4.8: Lowpass filtered $\mathcal{L}_1$, Pose error metrics.

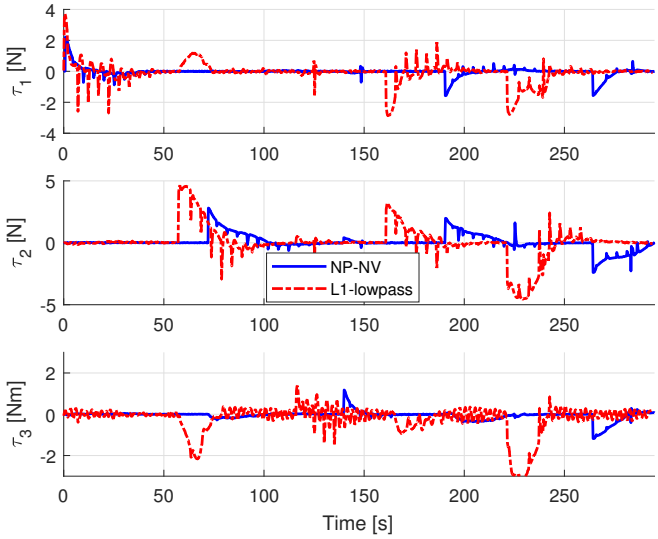

Figure 4.9: Lowpass filtered $\mathcal{L}_1$, Control inputs.

Figure 4.10 shows the path of the $\mathcal{L}_1$ controller enhanced with an MRS-model to limit the control input to the ship. Initially, the $\mathcal{L}_1$-MRS was run with the rate constrains in

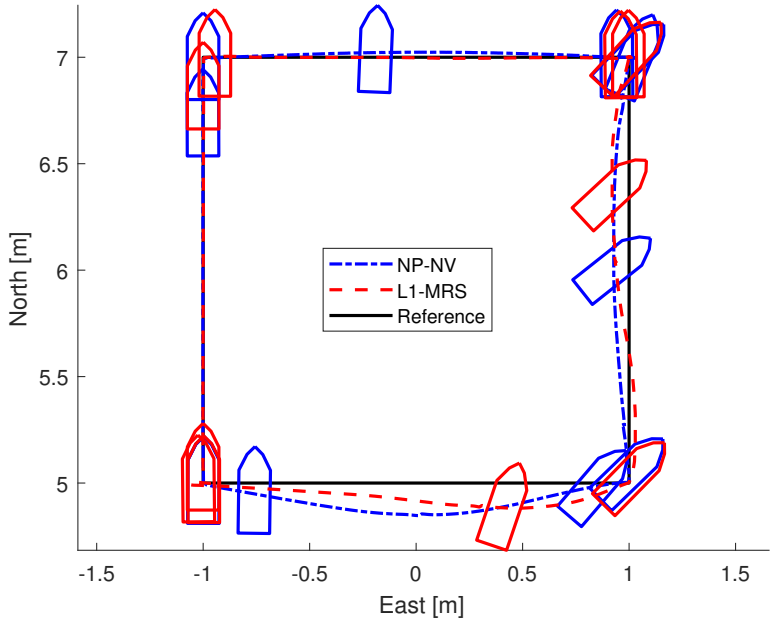

Figure 4.10: $\mathcal{L}_1$ with MRS 4-corner test. Rate constraints factored by 1.2.

Table 4.1, but it resulted in significant overshoot, likely due to the rate limits being to conservative for the aggressive controller. In this test, the limits are increased by a factor of 1.2. The ship follows the reference better than the nominal NP-NV, but not as good as the unconstrained $\mathcal{L}_1$. This could be due to too strict limits on both the magnitude and rate of the MRS model.

In Figure 4.11, the evolution of the metrics is shown. As with the unconstrained test of $\mathcal{L}_1$, the MRS-fitted controller is faster to complete the 4-corner test than the nominal, but with higher IAEW and IADC. Nonetheless, it can be noted that the MRS reduces the energy consumption by the IAEW in comparison to the unconstrained $\mathcal{L}_1$, as seen in Table 4.2.

The effects of the magnitude limits of the MRS is seen in Figure 4.12, where especially the commanded force in sway is limited, and lower than the nominal.

Since the results from the first $\mathcal{L}_1$-MRS test could indicate that the saturation limits were not liberal enough, a new experiment was done with increasing the rate limits with a factor of 1.5. The path plot for this experiment is shown in Figure 4.13. Unfortunately, this did not lead to better tracking, as the path and the IAE are similar to the MRS test with rate factored by 1.2. This indicates that the possibly the issue is not only with the rate but also with the magnitude limitations set.

Even though the increased rate limitations of the MRS fitted on $\mathcal{L}_1$ does not improve tracking, the wear on actuators by the IADC metric were reduced by the more liberal rate limit, a reduction of approximately 11 percent, as seen in Table 4.2.

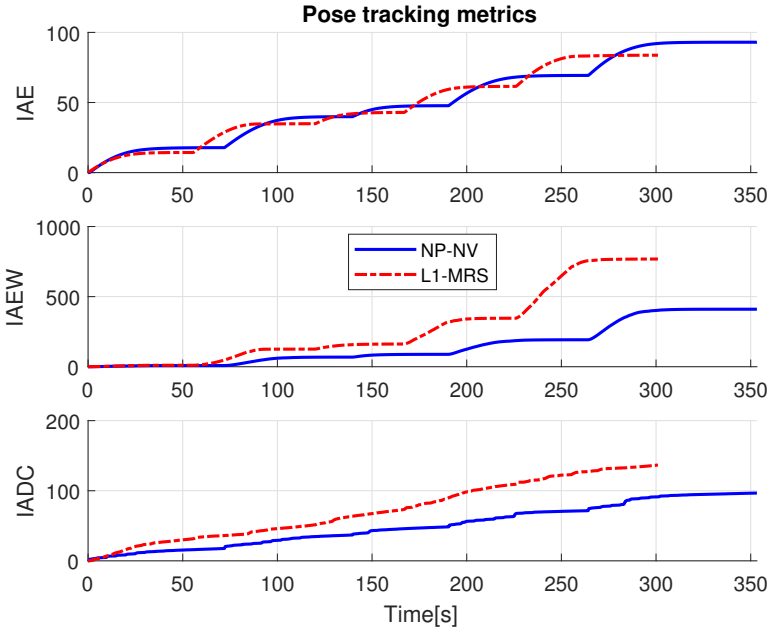

Figure 4.11: $\mathcal{L}_1$ with MRS, Pose error metrics. Rate constraints factored by 1.2.

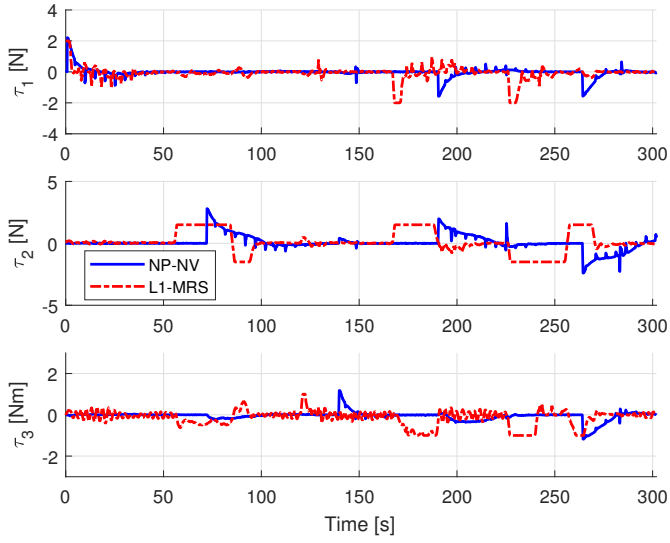

Figure 4.12: $\mathcal{L}_1$with MRS, Control input. Rate constraints factored by 1.2.

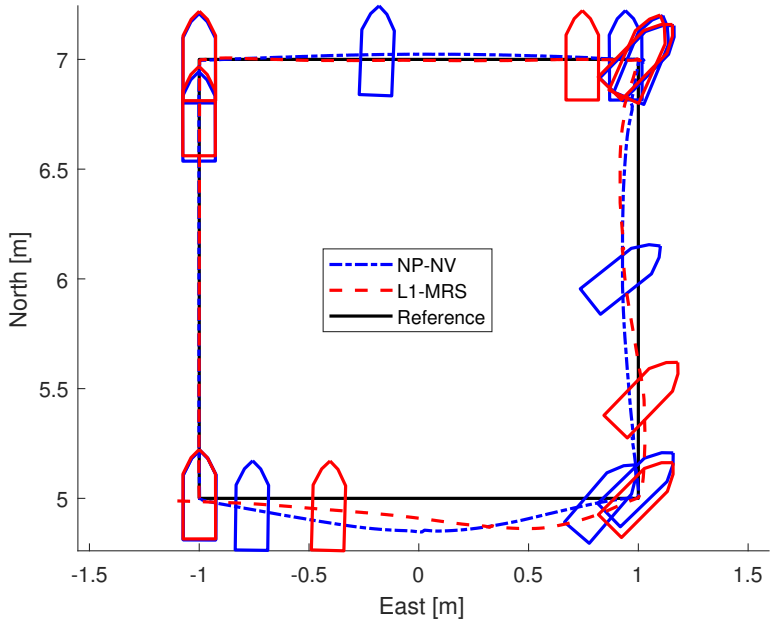

Figure 4.13: $\mathcal{L}_1$ with MRS 4-corner test. Rate constraints factored by 1.5.

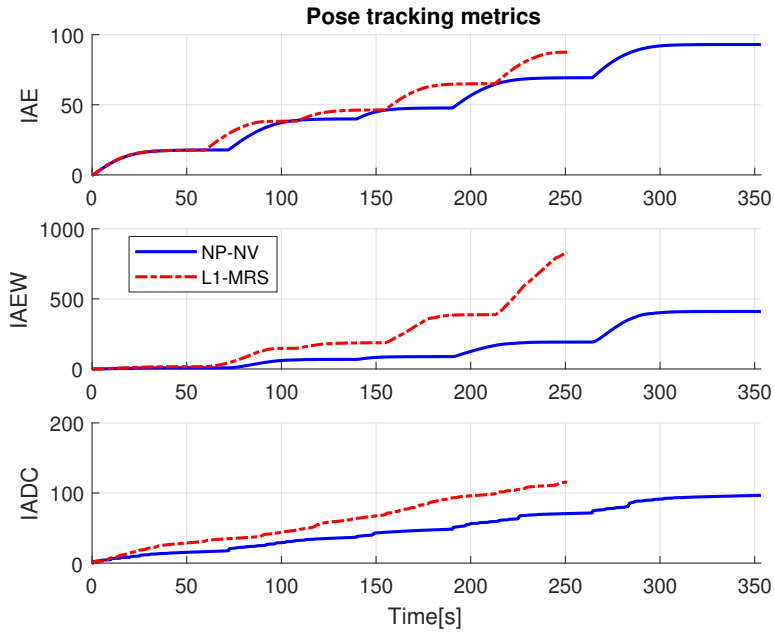

Figure 4.14: $\mathcal{L}_1$ with MRS, Pose error metrics. Rate constraints factored by 1.5.

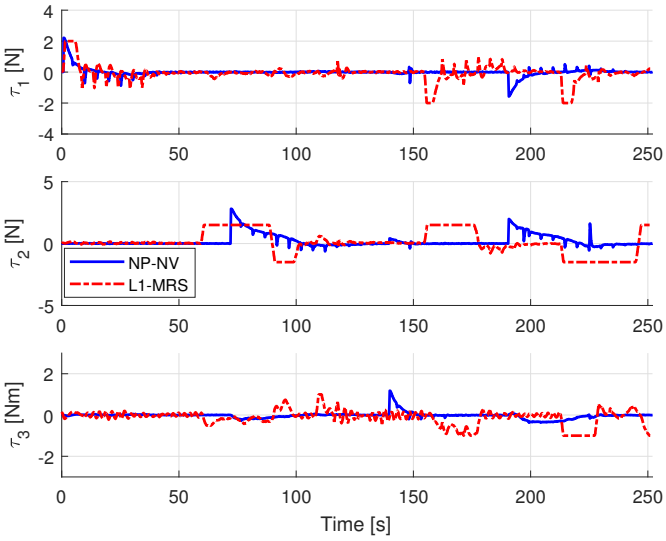

Figure 4.15: $\mathcal{L}_1$ with MRS, Control inputs. Rate constraints factored by 1.5.

4.2.2 Immersion and Invariance Adaptive Control Experiments

The following control and adaptation law is used in these experiments:

$$\boldsymbol{\tau} = \boldsymbol{M}\dot{\boldsymbol{\alpha}} + \boldsymbol{C}(\boldsymbol{\nu})\boldsymbol{\nu} - \boldsymbol{g}(\boldsymbol{\nu})\boldsymbol{\nu} - \boldsymbol{K}_2(\cdot)\boldsymbol{z}_2 - \boldsymbol{\Phi}(\boldsymbol{\nu})(\hat{\phi} + \Gamma_k \boldsymbol{\Phi}(\boldsymbol{\nu})^\top \boldsymbol{z}_2)$$
$$\dot{\hat{\psi}} = -\boldsymbol{\Gamma_k}\boldsymbol{\Phi}(\boldsymbol{\nu})^\top(\boldsymbol{\tau} - \boldsymbol{M}\dot{\boldsymbol{\alpha}} + \boldsymbol{R}^\top \boldsymbol{w_\delta} - \boldsymbol{C}(\boldsymbol{\nu})\boldsymbol{\nu} + \boldsymbol{g}(\boldsymbol{\nu})\boldsymbol{\nu} + \boldsymbol{\Phi}(\boldsymbol{\nu})(\hat{\phi} + \Gamma_k \Phi(\nu)^\top \boldsymbol{z}_2).$$

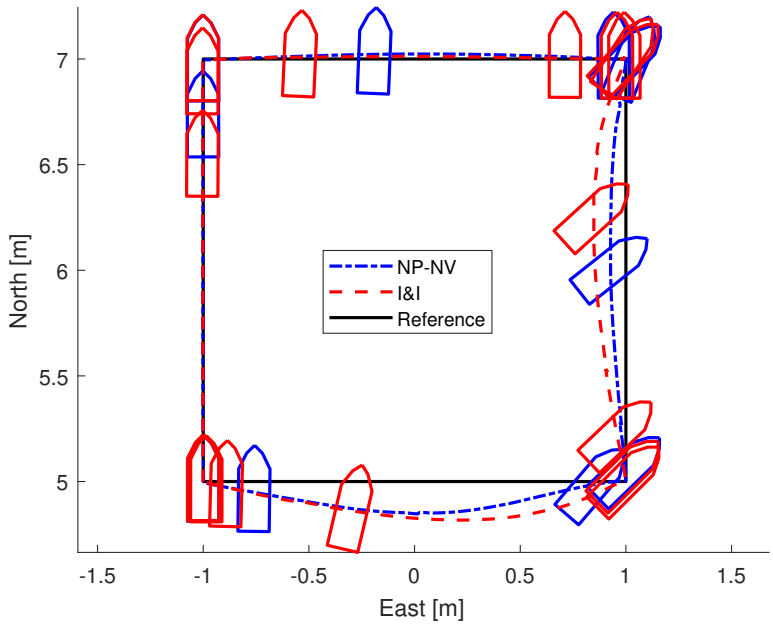

Figure 4.16: Unconstrained I&I 4-corner test.

The 4-corner path of the I&I adaptation is shown in Figure 4.16. As with the $\mathcal{L}_1$ adaptive, the I&I is adaptation fitted to the nominal NP-NV cascaded nonlinear feedback controller. Although, in this case the adaptation seems to deteriorate the reference tracking ability, as seen in the pose error metrics in Figure 4.17.

Additionally, the adaptation also appears to slow the controller down by almost 150 seconds overall on the 4-corner maneuver. This could suggest that the tuning of the adaptive parameter gains are not sufficiently accurate, causing the adaptation to not compensate for the inherent uncertainties in the model, but on the contrary worsen the performance. Moreover, as seen in Figure 4.18, similarly to $\mathcal{L}_1$, the I&I adaptation is more susceptible to noise in the feedback signals.

The I&I is then tested with the MRS model fitted, using the rate limits from Table 4.1, to which the path plot is shown in Figure 4.19. Even though it might look as the performance is worsened compared to the unconstrained test, the MRS limited I&I achieved the same

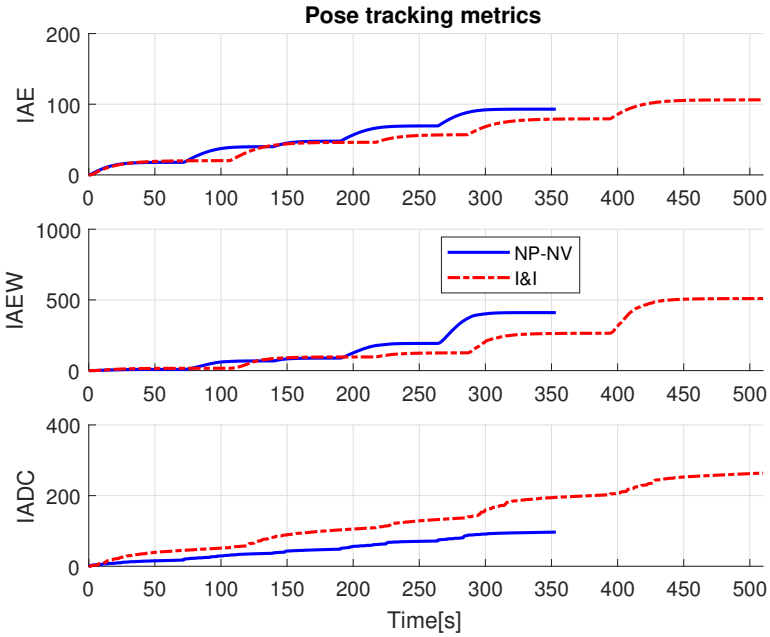

Figure 4.17: Unconstrained I&I , Pose error metrics.

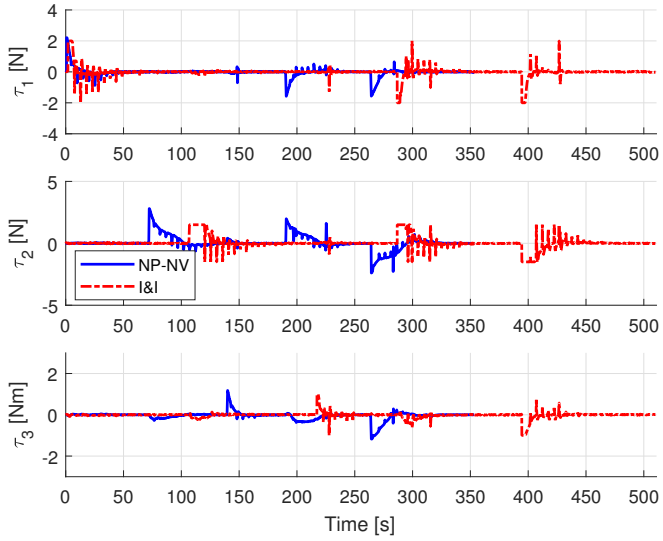

Figure 4.18: Unconstrained I&I , Control inputs.

overall pose error, as seen in Figure 4.20 and Table 4.2. Moreover, the IADC metric illustrating actuator wear is lowered compared to the nominal NP-NV. This is reasonably

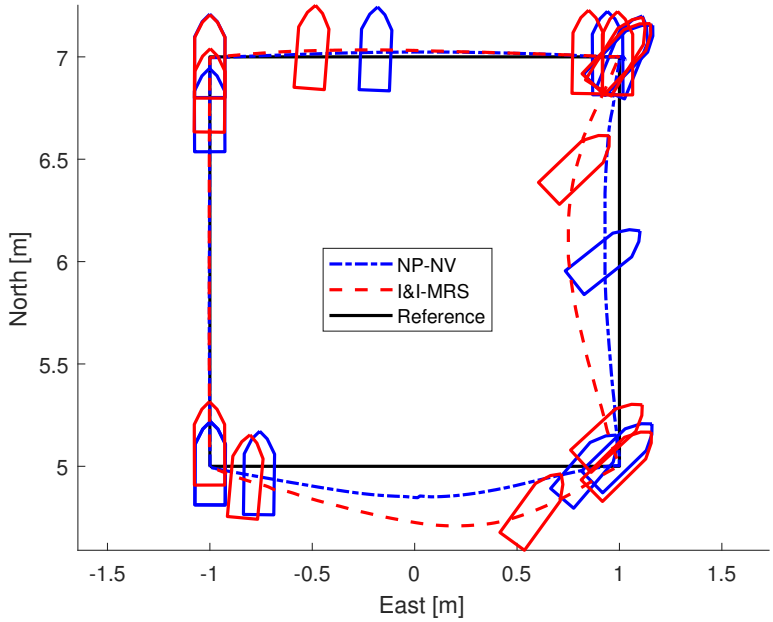

Figure 4.19: I&I with MRS, 4-corner test.

assumed to be due to the limiting effects of the MRS-model.

As the metrics in Fig .4.17 show, the I&I-MRS control system still has higher energy consumption than NP-NV.

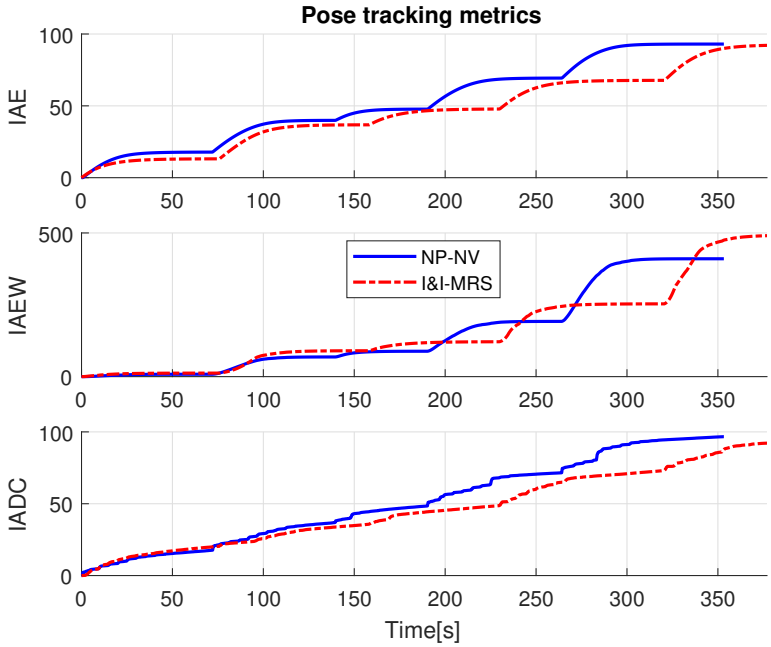

Figure 4.20: I&I with MRS , Pose error metrics.

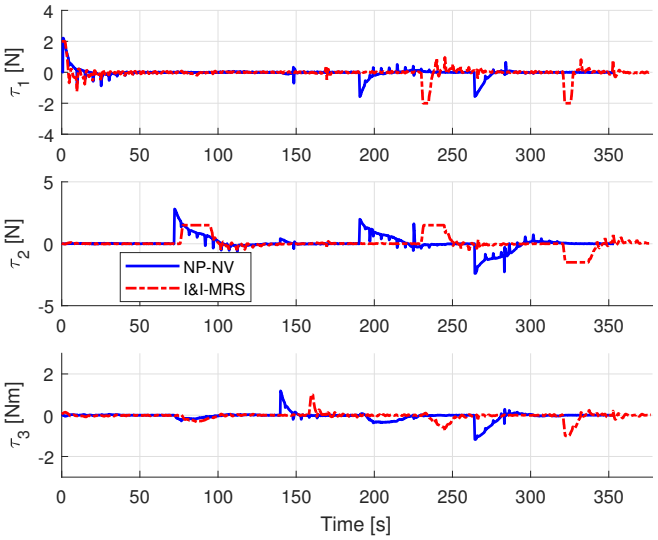

Figure 4.21: I&I with MRS , Control inputs.

4.2.3 Summary of Lab Session 1

Summarizing the experiments from the first lab session, there are some key findings to note. When evaluating the controllers overall ability to reduce control error during the 4-corner test, the unconstrained $\mathcal{L}_1$ adaptive scheme is the most capable in terms of the IAE metric, especially in the $(4 \rightarrow 5)$ backwards motion as seen in Figure 2.7. For this motion, all other controllers seem to relax the keeping of the East coordinate, as well as several degrees in heading keeping, while $\mathcal{L}_1$ manages to keep the East and heading at a small error. Admittedly, the aggressiveness of the $\mathcal{L}_1$ does lead to a higher energy consumption and actuator wear when achieving improved tracking. The experiments with using an MRS model in cascade with $\mathcal{L}_1$ does seem promising in reducing these downsides, at a minimal cost to pose error, therefore this adaptive control system will be continued in the second lab session, discussed later in this chapter. Since the I&I experiments are not as promising, the main focus will be on the $\mathcal{L}_1$ further-on.

One can observe that while the I&I adaptive control was significantly better in the simulations than nominal control, the results here point to the opposite, suggesting that the adaptation failing to estimate the real model.

The results from the first lab session correspond with the simulation results in terms of pose error. However, when considering the energy consumption by the IAEW metric, where in the simulations the MRS lead to a higher IAEW than the unconstrained, in the experiments it reduces the IAEW. Intuitively, the MRS should lead to a lower energy consumption by limiting control input, which points to that the simulator might not represent all aspects of the lab conditions.

Another thing to note about the results presented here is the significant spikes that are present in the plotted control inputs for all controllers. This phenomenon is due to inherent flaws in the velocity estimator, which will be addressed and corrected in the following section. In Table 4.2, all the final maximum values for the tested control implementations

Controller	**IAE**	**IAEW**	**IADC**
$NP-NV$	93	**410**	96
$\mathcal{L}_1 unconstr.$	**81**	915	256
$\mathcal{L}_1 LP$	81	982	282
$\mathcal{L}_1 MRS1.2$	83	762	130
$\mathcal{L}_1 MRS1.5$	85	831	115
$I\&I unconstr.$	106	509	261
$I\&I MRS.$	92	490	**92**

Table 4.2: End values of performance metrics - pose error

are displayed. The metric values are rounded to the nearest integer for readability.

4.3 Findings and Improvements

4.3.1 Velocity Estimation

When evaluating the experimental data from the first lab session, it became clear that there were some problems with the positioning camera system. During a experiment, due to a combination of calibration inaccuracies and motion, the infrared reflector orbs on the ship can cause ”reflection shadow”, thus leading to a small jump in position. This phenomenon is shown in Figure 4.22. While the change might only be 2 cm in magnitude, it occurs in a single time sample of 10 milliseconds, which results in a sudden velocity change of 2 m/s, which is not only a physically unreachable velocity for the ship, but also beyond the feasible acceleration. Since the estimated velocity is fed back into the control system, it causes the controller to try to compensate for the non-physical behavior, leading to a noisy control signal and also higher wear on the actuators which is seen in the plotted control inputs in the previous section.

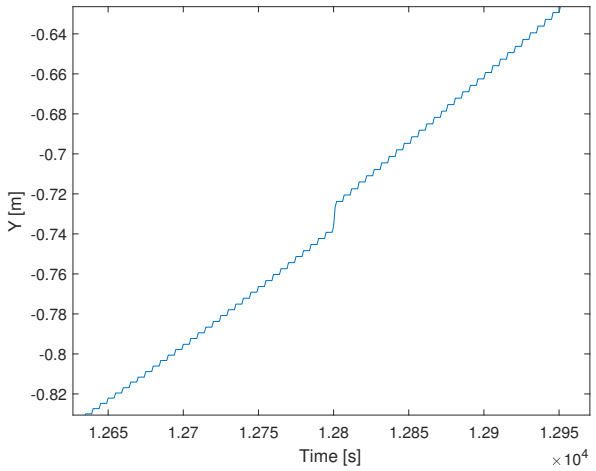

Figure 4.22: Jump-phenomenon in pose measurement

The correct for this behavior, some changes to the estimator are proposed; The velocity estimator previously implemented in CSAD for the lab is a applied derivative filter. Augmenting this filter to compensate for the ”spring”-effect, maximal values for CSAD feasible acceleration were set as follows:

$$a_{surge}^{MAX} = \pm 0.13 m/s^2 \tag{4.1}$$

$$a_{sway}^{MAX} = \pm 0.0267 m/s^2 \tag{4.2}$$

$$a_{yaw}^{MAX} = \pm 0.0052 rad/s^2 \tag{4.3}$$

These maximal values are determined through velocity tests in the MC-lab basin, using CSAD on maximum thrust in each degree-of-freedom. Since the control system runs at

100Hz, these limit parameters are then scaled by 100 to get allowed change-per-sample, and then implemented in block form in the derivative filter. Only minor tuning is then needed to achieve optimal cutting of impulse transients in the estimated velocity signal. The final limit values are displayed in Table 4.3. It should be noted that these are vessel-specific, and should be adjusted in the event of a new actuator setup, or if using the control system on another vessel.

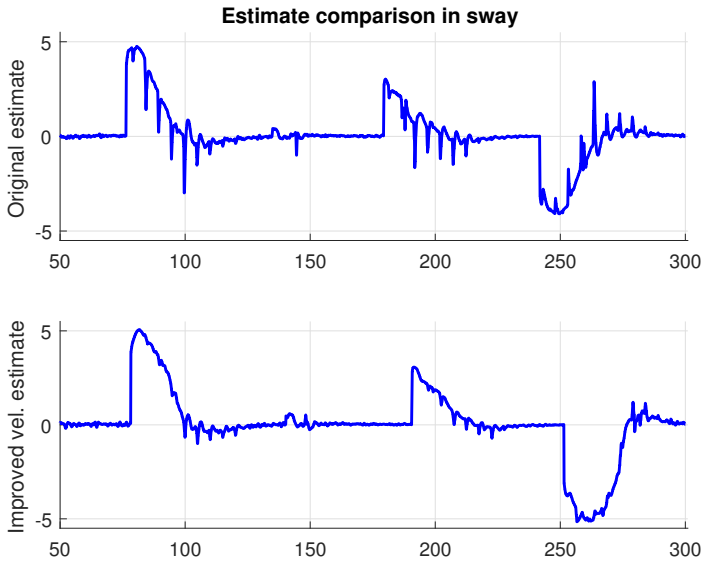

Figure 4.23: Comparison of control input in sway with new velocity estimator

The effects of the estimator changes is illustrated in Figure 4.23. The figure shows the commanded input in sway for a 4-corner test using the the original and the improved velocity estimator. Both runs are done using the $\mathcal{L}_1$ cascade controller with the same controller and parameter gains. The experiments are done 10 minutes apart, giving identical water conditions in the MC-lab basin. While using the new estimator might not further affect the overall tracking accuracy of the controller significantly, it is beneficial in reducing actuator wear and tear, and can reduce power consumption since the controller will not try to compensate for non-physical behavior. This is especially useful for the $\mathcal{L}_1$ cascade controller, due to its relatively high-gain adaptation, which leads to significant jerk in the actuator system.

As previously discussed, the velocity estimator implemented in the lab prior has some design weaknesses. By design weaknesses, it is meant how it handles errors occurring in the camera-system, which cannot simply be corrected without extensive reconfiguration of the lab setup, only compensated for. Among these errors is the ”spring”-effect, which in this new estimator design is handled by setting maximum values for the acceleration in each degree of freedom, per time sample. This corrects a lot of the spikes in the estimated

DOF	Value
$surge$	0.0011
$sway$	0.000454
yaw	0.00071

Table 4.3: Acceleration limits per sample in velocity estimator

velocity signal, thus leading to a smoother control signal, as seen in Figure 4.23.

Furthermore, to make the estimator more fault-tolerant, it is necessary to address the issue of a lost position signal. At some points, the Qualisys camera system will simply loose the view of the ship. To avoid giving a measurement of the basin origin, at $[0, 0, 0]^T$, which might lead to uncontrolled acceleration of the ship, the firmware of the system will simply give the last measured position in a loop until the ship is detected again, usually within a few samples. An example of the lost signal can be seen in Figure 4.24. However, this approach will cause some unwanted effects. The estimated pose follows the measurement, since it is updated using the measurement signal. Then, when the estimate is corrected, the consequence is a sudden change in velocity, as seen in Figure 4.25.

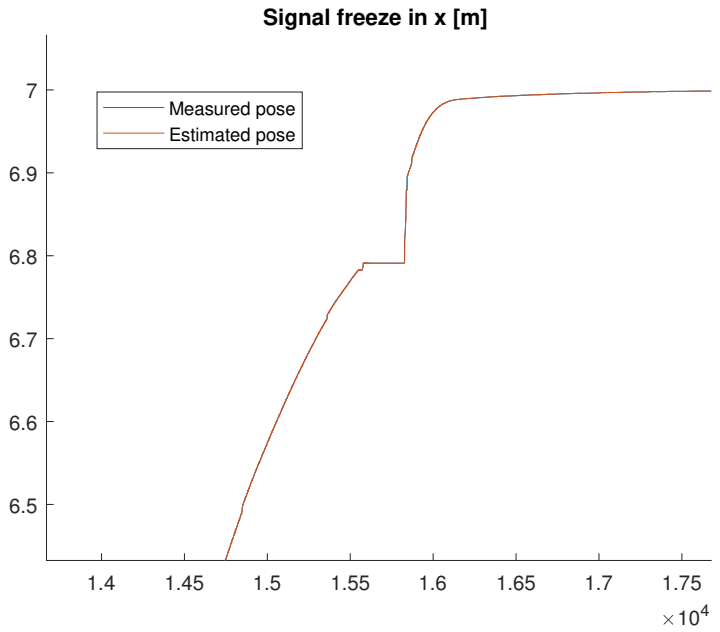

Figure 4.24: "Frozen" measurement signal

In Figure 4.24, as one can see, the pose measurement is still for around 250 samples, or 2,5 seconds, and while the control system assumes the ship is at a constant position, it is in the middle of a motion and has a surge speed. When the camera system then again detects the ship, the pose is changed and the estimate jumps to the new position, leading to a

corresponding, sudden change in the velocity estimate, as seen in Figure 4.25. In addition to having a reliable estimate, it is strongly desirable to avoid the velocity spikes in order to avoid false motions and correspondent noise in the control input.

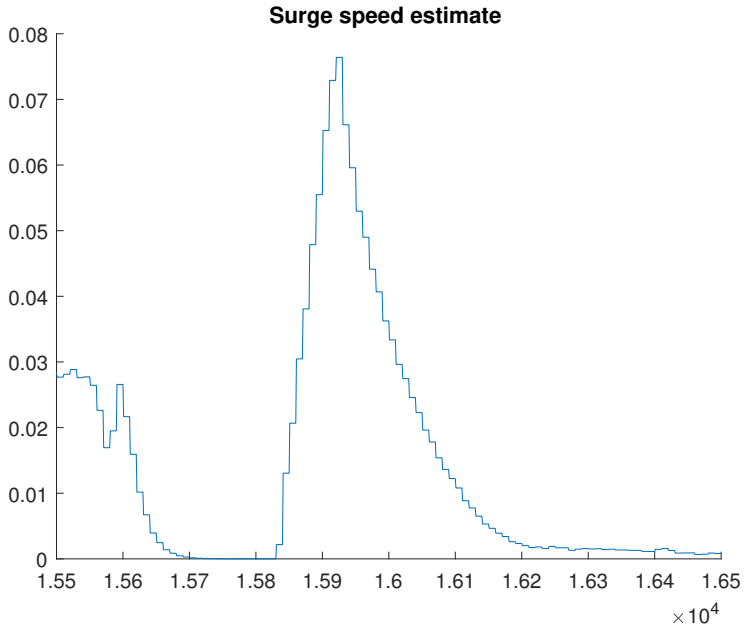

Figure 4.25: Sudden surge after recovering position measurement

To ensure that the velocity estimator is fault-tolerant to the phenomenons mentioned, and also more robust operation, a revision is proposed:
The estimator will have three states of operation; Normal operation, frozen measurement signal and rediscovered measurement signal. A subsystem is written in the control implementation, which compares each new sample to the previous down to the 8th decimal. The Qualisys system runs at 20Hz, while the control system runs at 100Hz, which means that every five consecutive samples from the camera system will be identical. If, however, the following sample is identical to the previous five at 10^8 decimal precision in all DOF, the signal is assumed to have been lost. A Boolean ”measurement frozen” signal is then sent to the estimator, which switches state. To avoid detecting false positives, the threshold for a lost signal is set to seven consecutive identical measurement samples.

The velocity estimator is rewritten as a derivative filter using the pose measurements as

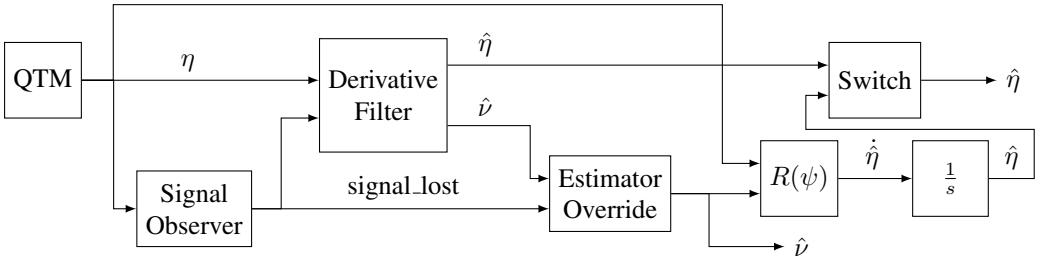

Figure 4.26: Block diagram for the updated velocity estimator

input. For normal operation, this is implemented as such:

$$\boldsymbol{\eta}_{filtered(n)} = a * \boldsymbol{\eta}_{measured(n)} + (1-a) * \boldsymbol{\eta}_{filtered(n-1)} \tag{4.4}$$

$$\dot{\boldsymbol{\eta}} = \frac{\boldsymbol{\eta}_{filtered(n)} - \boldsymbol{\eta}_{filtered(n-1)}}{h} \tag{4.5}$$

$$\dot{\boldsymbol{\eta}}_{filtered(n)} = b * \dot{\boldsymbol{\eta}}_{measured} + (1-b) * \dot{\boldsymbol{\eta}}_{filtered(n-1)} \tag{4.6}$$

$$\hat{\boldsymbol{\nu}} = \boldsymbol{R}^T(\psi) * \dot{\boldsymbol{\eta}}_{filtered(n)}, \tag{4.7}$$

where h is the sample time in the control system, 0.01 second, and a, b are the cutoff-parameters for the filter. When the estimator detects a lost signal, it switches state and keeps the last recorded $\hat{\boldsymbol{\nu}}$ to estimate the position until the camera system again detects the ship. While the signal is lost, the estimator will run as:

$$\hat{\boldsymbol{\eta}} = \int \boldsymbol{R}(\hat{\psi})\hat{\boldsymbol{\nu}} \tag{4.8}$$

$$\hat{\boldsymbol{\eta}}_{(0)} = \hat{\boldsymbol{\eta}}_{(n-1)} \tag{4.9}$$

Then, when the measurement signal is recovered, it switches back to (4.7), and is then initialized by:

$$\boldsymbol{\eta}_{filtered(n-1)} = \hat{\boldsymbol{\eta}}_{(n-1)} \tag{4.10}$$

$$\dot{\boldsymbol{\eta}}_{filtered(n-1)} = \hat{\boldsymbol{\nu}}_{(n-1)} \tag{4.11}$$

The block diagram for the re-written velocity estimator as implemented on CSAD can be seen in Figure 4.26.

4.3.2 Ship Model Adjustment

As discussed in Chapter 2, some adjustments to the ship model presented were needed from the model presented in [2] and [21]. The first lab session is run with these parameter

changes, see Table 2.1. After the first lab session, behavior of the ship suggested that the model was not entirely accurate. To identify the model discrepancies, performance tests were done to determine maximum velocity and acceleration in each DOF. The tests were done by giving the ship maximum thrust and allowing it to reach constant velocity, before retrieving data. For the yaw measurement, the ship was placed in the midle of the basin and allowed to rotate freely at maximum thrust. As in the initial modelling, the model parameters are adjusted using simulations until the behaviour matches the lab behaviour, as seen in Figure 4.27, 4.28 and 4.29. Note that the spikes present in the lab data in the plots are due to the faulty velocity estimator, which has been previously discussed and corrected. The maximum velocities were found to be 0.4142 [m/s], 0.109 [m/s] and 6.327 [deg/s] in surge, sway and yaw rate, respectively, which corresponds well to the experimental results from the laboratory tests.

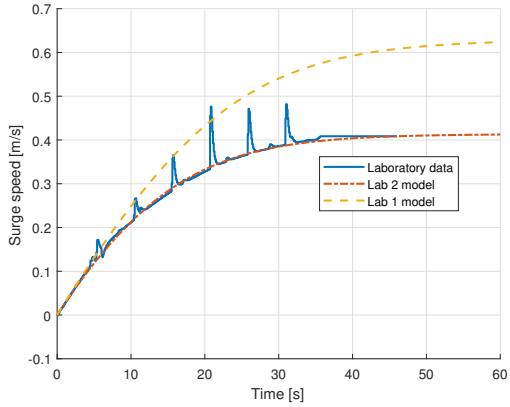

Figure 4.27: Surge test

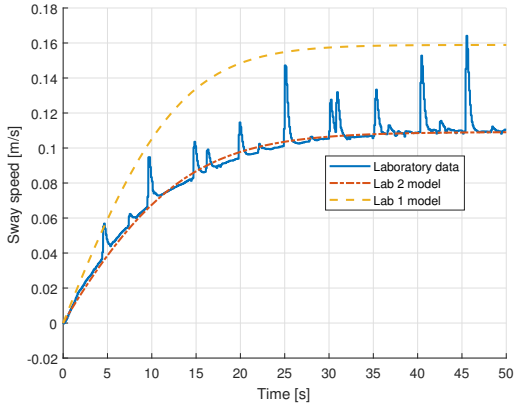

Figure 4.28: Sway test

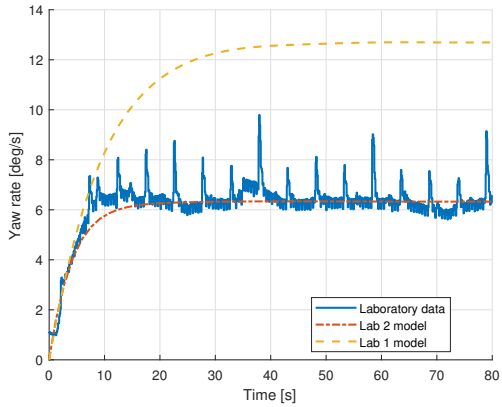

Figure 4.29: Yaw test

Table 4.4 displays the final values of the parameter values after the model adjustments, and will be used in the second lab session. Adjusted values are marked in bold. Note that in particular, the damping parameters needed adjustment, which point to the old model being under-damped compared with the real ship.

Parameter	Lab session 1 parameters	Updated for session 2	Unit
L	2.578	2.578	m
m	127.92	127.92	kg
x_g	0.0375	0.0375	m
I_z	62	62	kgm^2
$X_{\dot{u}}$	-3.26	$\mathbf{-10}$	kg
$Y_{\dot{v}}$	-28.9	$\mathbf{-105}$	kg
$Y_{\dot{r}}$	-0.525	-0.525	kgm
$N_{\dot{v}}$	-0.157	-0.157	kgm
$N_{\dot{r}}$	-14	$\mathbf{-3.5}$	kgm^2
X_u	-2.33	$\mathbf{-5.1}$	kg/s
$X_{\|u\|u}$	0	0	kg/m
X_{uuu}	-8.56	$\mathbf{-18.63}$	kgs/m^2
Y_v	-4.67	$\mathbf{-10.2}$	kg/s
$Y_{\|v\|v}$	-0.398	$\mathbf{-0.86}$	kg/m
Y_{vvv}	-313	$\mathbf{-665}$	kgs/m^2
N_v	0	0	kgm/s
$N_{\|v\|v}$	-0.209	$\mathbf{-0.24}$	kg/m
N_{vvv}	0	0	kgs/m^2
Y_r	-7.25	$\mathbf{-6.25}$	kgm/s
$Y_{\|r\|r}$	-3.45	$\mathbf{-3.65}$	kg/m
Y_{rrr}	0	0	kgs/m^2
N_r	-6.916	$\mathbf{-14.55}$	kg/s
$N_{\|r\|r}$	-4.734	$\mathbf{-9.96}$	kgm^2
N_{rrr}	-0.147	$\mathbf{-0.31}$	kgs/m^2
$N_{\|v\|r}$	0.08	0	kg/m
$N_{\|r\|v}$	0.08	0	kg/m
$Y_{\|v\|r}$	-0.845	0	kg
$Y_{\|r\|v}$	-0.805	0	kg

Table 4.4: Updated values of the ship model parameters for CSAD.

4.3.3 Parameter Gain Adjustment

$\mathcal{L}_1$ adaptive control

Before the first lab session, the chosen parameter gains for the controller was tested using simulated results. In the real conditions in the lab basin however, it became clear that some adjustments were needed. Among these, it is worth mentioning updating the gains for the state predictor. The L2 gain should be of greater magnitude than the L1 gain, a relation not maintained in lab session 1, see Table 4.1. The predictor L2 parameter is increased by a factor of 3 to ensure this relation. After the re-written velocity estimator is implemented, a double 4-corner test is performed for the $\mathcal{L}_1$ controller, one with the previous value, and

one updated.

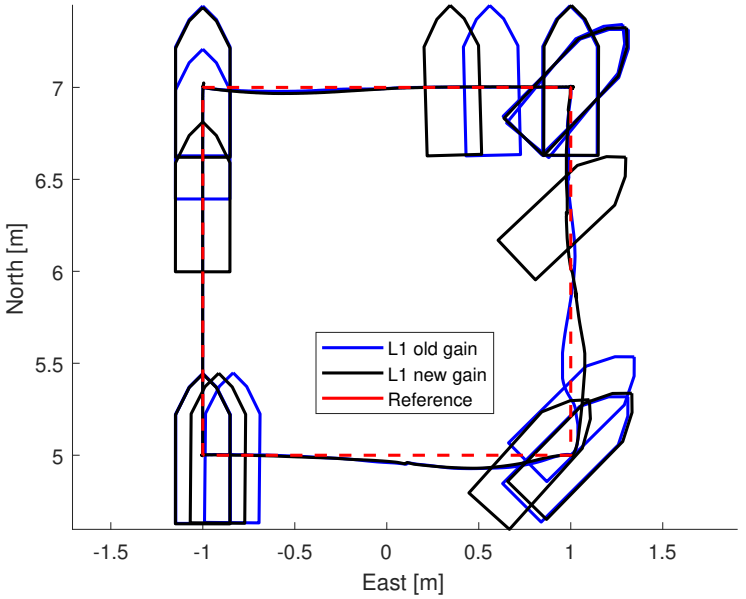

Figure 4.30: 4-corner test comparing predictor gain adjustment

L2 gain value	IAE	IAEW	IADC
$\boldsymbol{I}(4.8\pi)$	76	1231	253
$\boldsymbol{I}(14.4\pi)$	77	722	155

Table 4.5: Performance metric comparison - Updated L2 gain

As seen in from the surface plot in Figure 4.30 and the performance metrics in Figure 4.32, there is no significant difference in overall pose error for the 4-corner test. However, the updated predictor gain greatly reduces the power consumption by the IAEW metric, and the actuator wear. This can be seen by Figure 4.32 and in Table 4.5, where the final values of the metrics are displayed. The IAEW metric is reduced by 41% and the IADC by 38%, which is a substantial decrease. This parameter change will be kept into the second lab session.

Figure 4.31 shows the time evolution of the control input. The overall lower amplitude gives reduced power consumption, but does not lead to a longer duration of the 4-corner test.

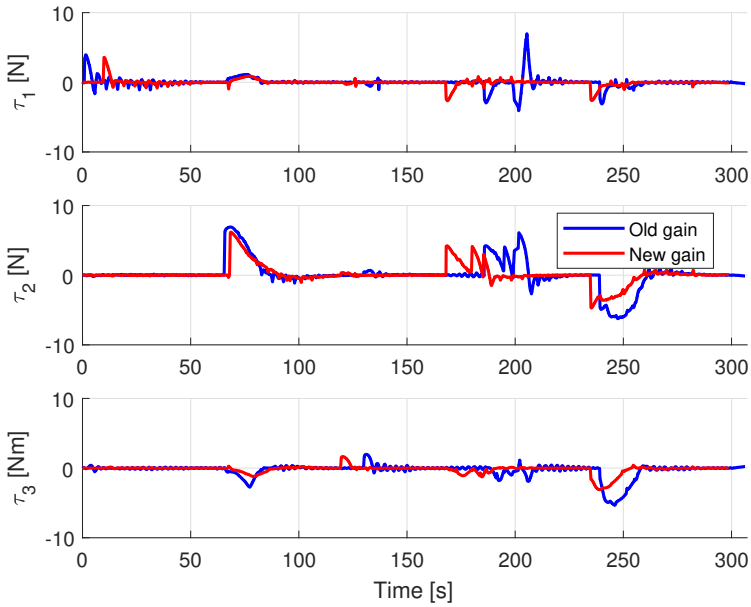

Figure 4.31: Control inputs comparing predictor gain adjustment

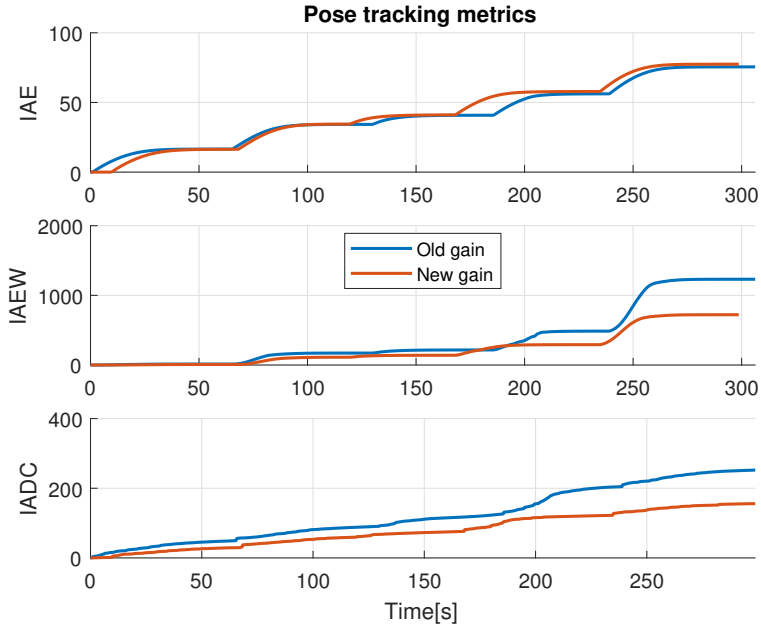

Figure 4.32: Performance metrics for comparing predictor gain adjustment

4.4 Lab Session 2 - May 2018

As in the first lab session, the NP-NV controller will be used as a nominal controller for comparison and to evaluate the performance of the adaptive scheme in this session. The NP-NV test is done under the new conditions as described in the previous section. The 4-corner test for the NP-NV is shown in Figure 4.33. It can be observed that the redesign of the velocity estimator and adjusted model parameters has an improving effect on the nominal NP-NV controller, especially for the $(4 \rightarrow 5)$ movement. The pose error IAE metric for NP-NV is also reduced by 14%, from 92 to 79.

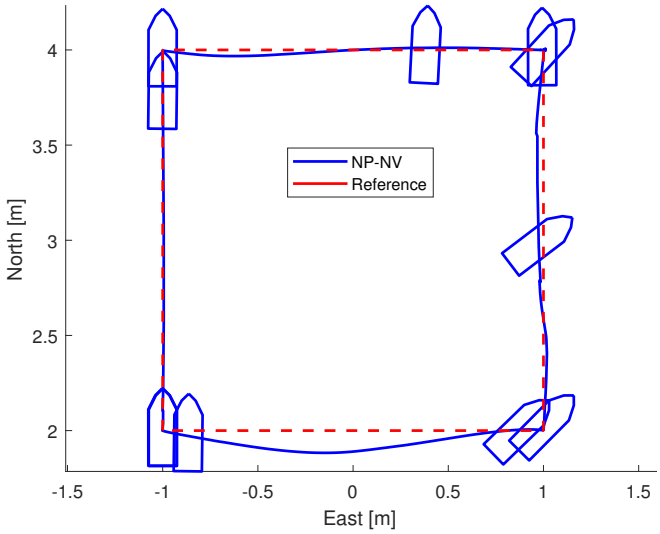

Figure 4.33: Unconstrained NPNV 4-corner test

The change of the North-axis of the 4-corner surface plots in this session, from [5,7] to [2,4], is due to a full re-calibration of the camera system, with the goal of reducing inaccuracies in the measurements. Otherwise the 4-corner experiments are performed in the same fashion as the first session.

	$\mathcal{L}_1$
$\boldsymbol{\Gamma}_1$	$\text{diag}([0.08, 0.08, 0.0698])$
$\boldsymbol{\Gamma}_2$	$\text{diag}([0.2, 0.2, 0.1745])\boldsymbol{M}$
$\Delta_{\tilde{p}}$	0.5
$\Delta_{\tilde{\psi}}$	0.5
$\Delta_{\tilde{v}}$	0.7
$\Delta_{\tilde{r}}$	1
$\boldsymbol{L_1}$	$\boldsymbol{I}(2\pi)^2$
$\boldsymbol{L_2}$	$\boldsymbol{I}(14.4\pi)$
$\boldsymbol{\gamma}_{w\delta}$	$(20\pi)^2/4$
$\boldsymbol{K}$	$\text{diag}([5, 2.78, 2.36])$
$\boldsymbol{sat_m}$	$[2.88, 1.60, 1.36]$
$\boldsymbol{sat_r}$	$[2.88, 1.60, 1.36]$
$\boldsymbol{K}_a$	$[0.01, 0.01, 0.05]$
$\boldsymbol{K}_a$	$[0.05, 0.05, 0.01]$

Table 4.6: Control parameters for lab session 2

Table 4.6 displays the control and parameter gains used for the second lab session. As mentioned in the summary of the first lab session, this session will focus on the $\mathcal{L}_1$ and improvement of the actuator handling, as it showed more promise than the I&I adaptive. In this session, the following adaptive control experiments are performed:

- $\mathcal{L}$ adaptive control,4-corner unconstrained.
- $\mathcal{L}$ adaptive control with MRS, 4-corner.
- $\mathcal{L}$ adaptive control with MRS, increased magnitude limits, 4-corner.
- $\mathcal{L}$ adaptive control with CG,4-corner.

4.4.1 $\mathcal{L}_1$ Adaptive Control Experiments

The following control and adaptation law is used in these experiments:

$$\boldsymbol{\tau} = \boldsymbol{M}\dot{\boldsymbol{\alpha}} + (\boldsymbol{C} + \boldsymbol{D})\boldsymbol{\alpha} - \boldsymbol{K}_2\boldsymbol{z}_2 - \hat{\boldsymbol{w}}_{\boldsymbol{\delta}}$$
$$\dot{\hat{\boldsymbol{w}}}_{\boldsymbol{\delta}} = -\gamma_{w_\delta}\boldsymbol{R}\tilde{\boldsymbol{\nu}}$$

Figure 4.34 shows the surface plot of the unconstrained $\mathcal{L}_1$. It can be seen that the reference tracking has been improved from the previous session, and the $\mathcal{L}_1$ has improved tracking over the nominal controller, in particular for the $(5 \rightarrow 1)$ motion.

In Figure 4.35 the time evolution of the performance metrics is shown. The unconstrained $\mathcal{L}_1$, as in the first session, is overall faster and more accurate in reference tracking than the

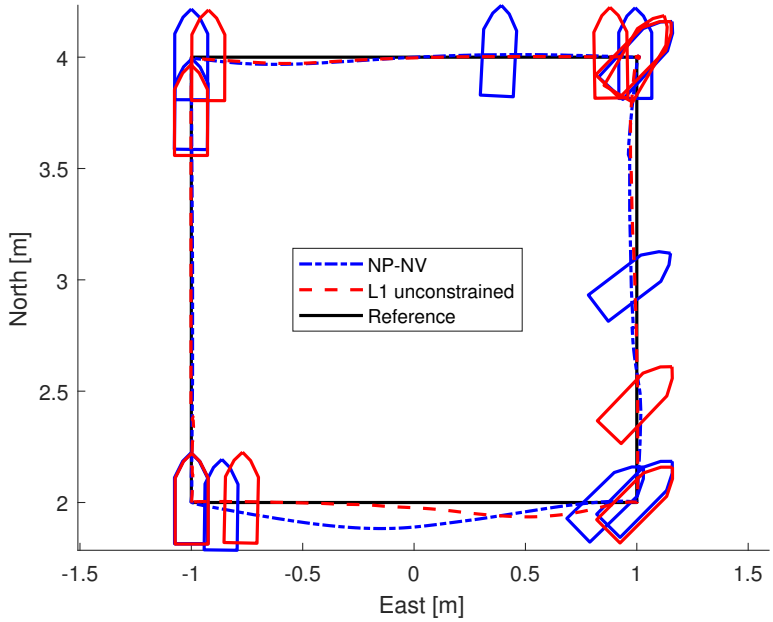

Figure 4.34: Unconstrained $\mathcal{L}_1$ 4-corner test.

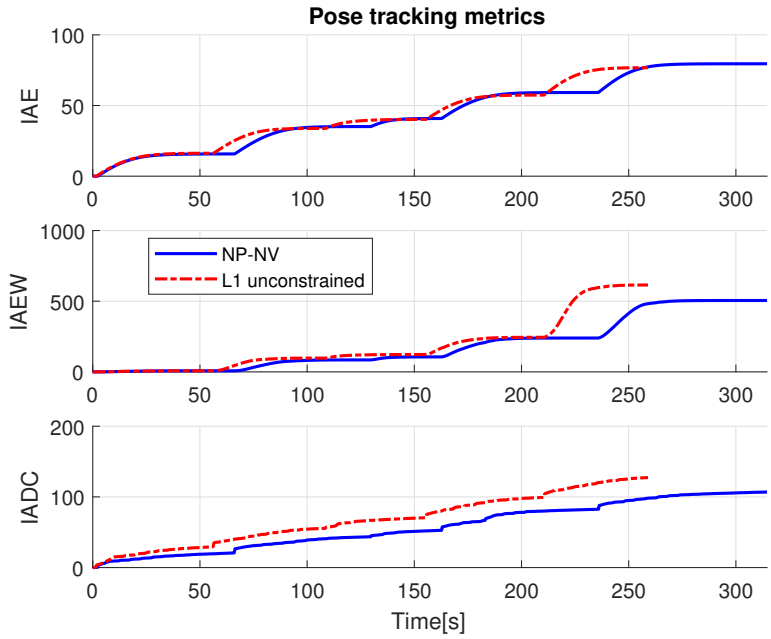

Figure 4.35: Unconstrained $\mathcal{L}_1$, Pose error metrics.

NP-NV for the 4-corner test. Note that even though the adaptive control is higher in terms of energy IAEW and wear IADC, the difference from the nominal is significantly reduced from the first lab session. This improvement is most likely due to the improved velocity estimation, as well as the upscaled L2 gain which was discussed in the last section. As a result, the adaptation is less exposed to measurement noise and this leads to a cleaner control input signal, which can be seen in Figure 4.36.

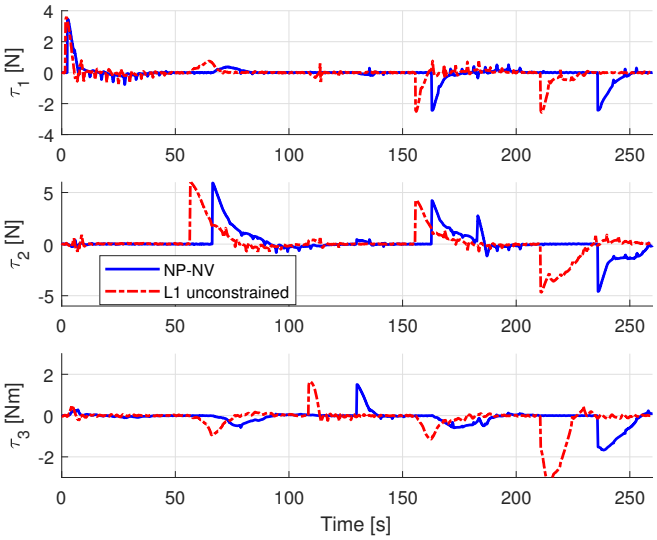

Figure 4.36: Unconstrained $\mathcal{L}_1$, Control inputs.

As mentioned in the discussion from the first lab session, the cascaded $\mathcal{L}_1$-MRS control yielded promising results. The MRS model limitations are tuned according to a more realistic behavior on the basis of tests done on the ship actuator setup, see Table 4.6. The path plot of the first MRS test is shown in Figure 4.37.

It can be observed that the adaptive controller follows the path well, although with some slip during the last 2 motions. This indicates that the magnitude limits could be too conservative for the $\mathcal{L}_1$ adaptive controller. Even though the ship is not physically able to output the desired force from $\mathcal{L}_1$, it could be that the high-gain adaptation gives a more suited control input than the set limitations of the MRS.

The pose error metrics for $\mathcal{L}_1$-MRS are shown in Figure 4.38. Note that the adaptive controller has reduced control rate metric IADC, or wear, than the nominal NP-NV.

Since the last $\mathcal{L}_1$-MRS experiment could indicate that the magnitude saturation limits were too conservative, the limits are then set to $[5, 5, 3]^\top$ with the goal of improving tracking by higher thrust allowance at the cost of energy consumption. The rate limitations are kept as before. The path plot is shown in Figure 4.40. As can be seen, the boat achieves better track following than in the last experiment, as well as NP-NV.

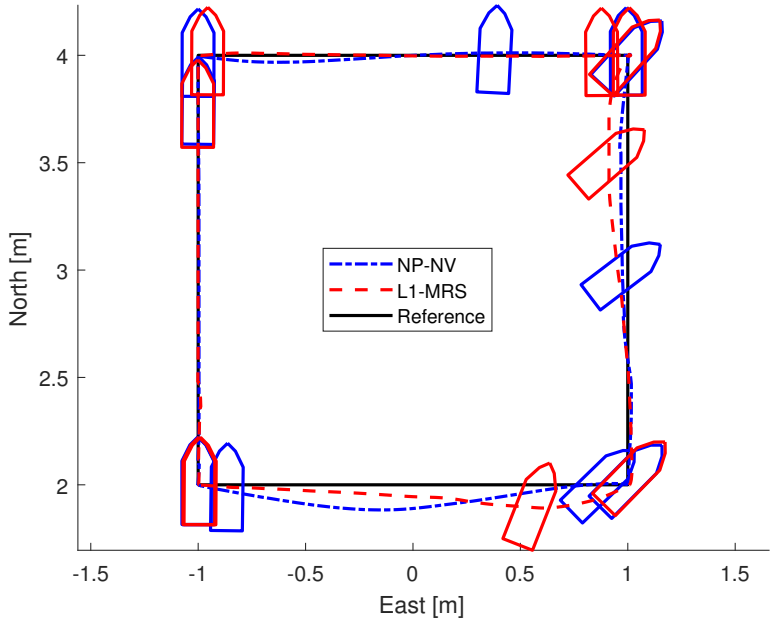

Figure 4.37: $\mathcal{L}_1$ with MRS 4-corner test. Magnitude limits as in Table 4.6

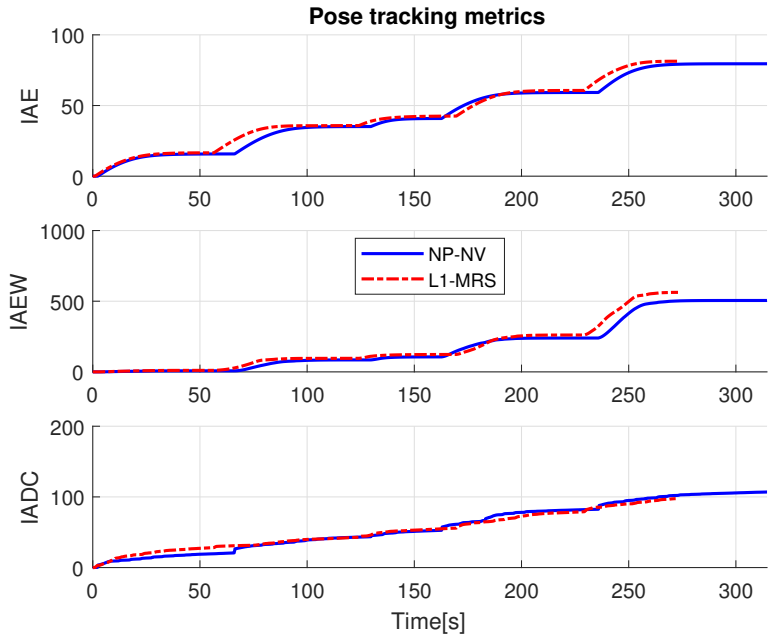

Figure 4.38: $\mathcal{L}_1$ with MRS, Pose error metrics. Magnitude limits as in Table 4.6

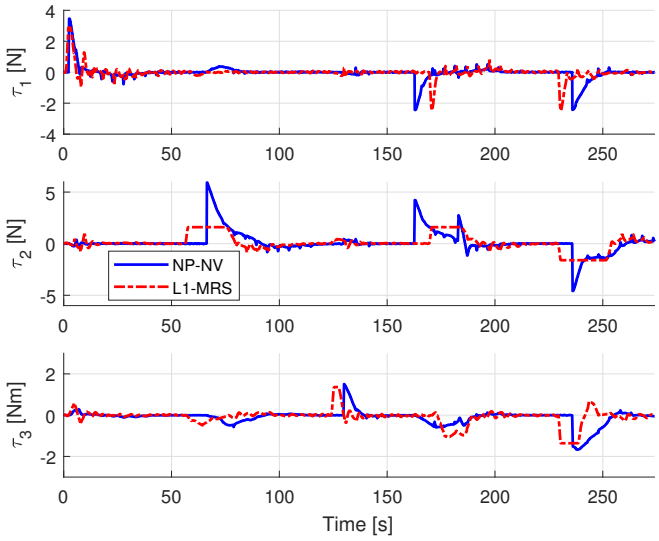

Figure 4.39: $\mathcal{L}_1$ with MRS, Control inputs. Magnitude limits as in Table 4.6.

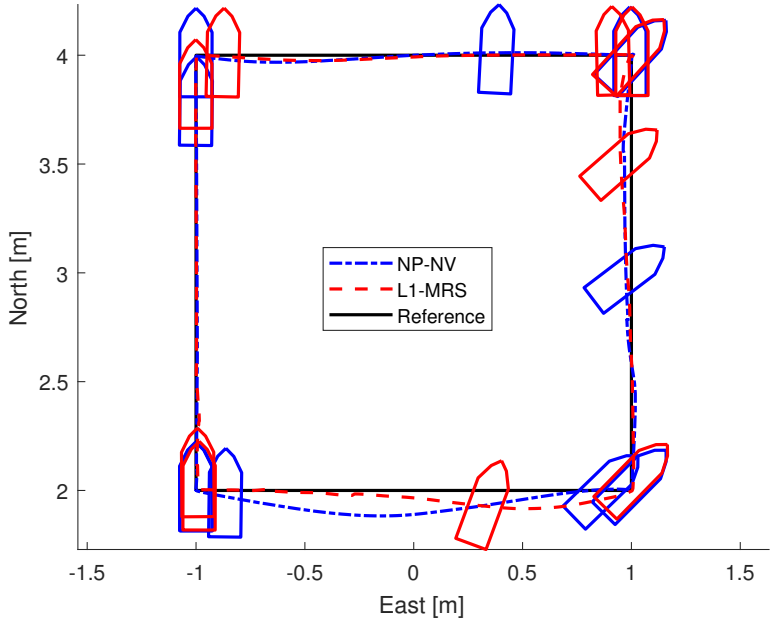

Figure 4.40: $\mathcal{L}_1$ with MRS 4-corner test. Magnitude limit $[5\ 5\ 3]^\top$.

However, as assumed the higher allowance increases the IAEW metric by 22 percent compared to the conservative magnitude limits, as can be seen in Table 4.7 and the metric plot

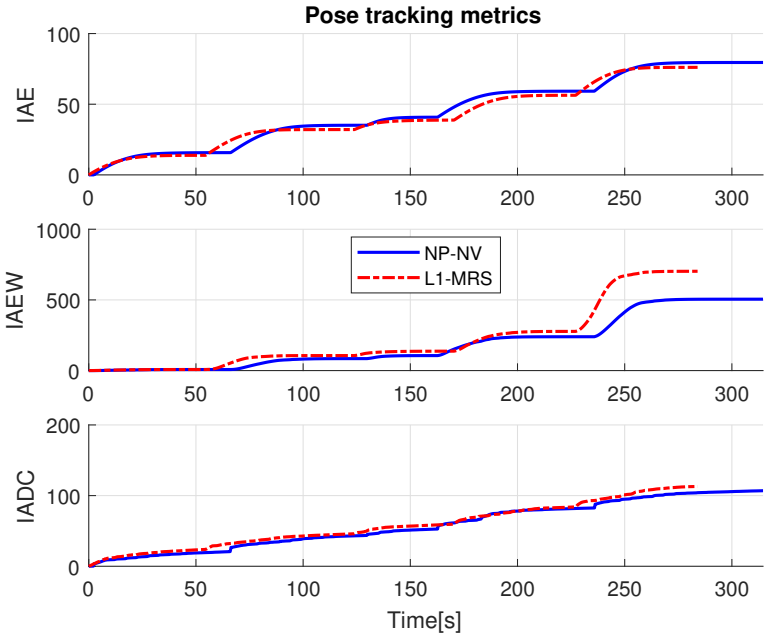

Figure 4.41: $\mathcal{L}_1$ with MRS, Pose error metrics. Magnitude limit $[5\ 5\ 3]^\top$.

in Figure 4.41. Fortunately, the IADC is similar to the nominal, indicating that the rate limits of the MRS has a positive effect on actuator wear & tear of the $\mathcal{L}_1$ adaptation.

Figure 4.43 displays the $\mathcal{L}_1$ adaptive controller fitted with the novel command governor architecture. Besides from a small drift at the first corner, $\mathcal{L}_1$-CG follows the path almost perfectly, admittedly at the cost of a significantly longer experiment time, which corresponds with the simulations. This is due to the nature of the command governor, which gives the control system target tracking behavior by altering the reference signal by the variable change. This can be seen in Figure 4.44 and 4.45, where the CG increases the experimental duration by approximately 200 seconds.

In Figure 4.44 the time evolution of the performance metrics for $\mathcal{L}_1$-CG is displayed. The adaptive implementation has significantly lower error and energy consumption, 70% in IAE and 87% in IAEW compared to the nominal NP-NV.

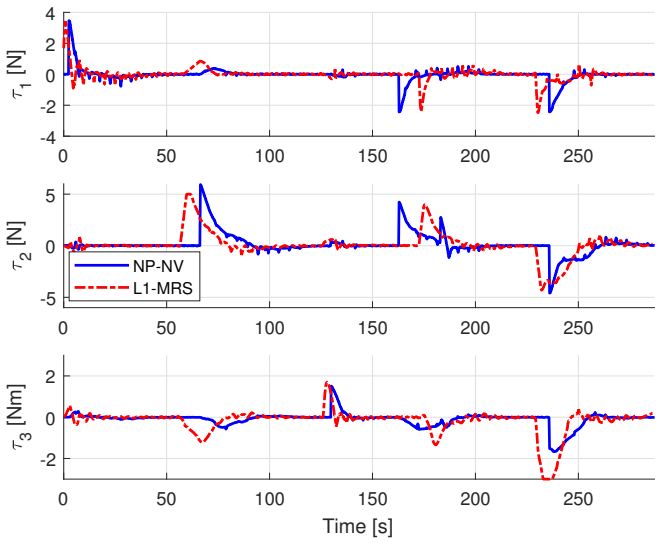

Figure 4.42: $\mathcal{L}_1$ with MRS, Control inputs. Magnitude limit $[5\ 5\ 3]^\top$.

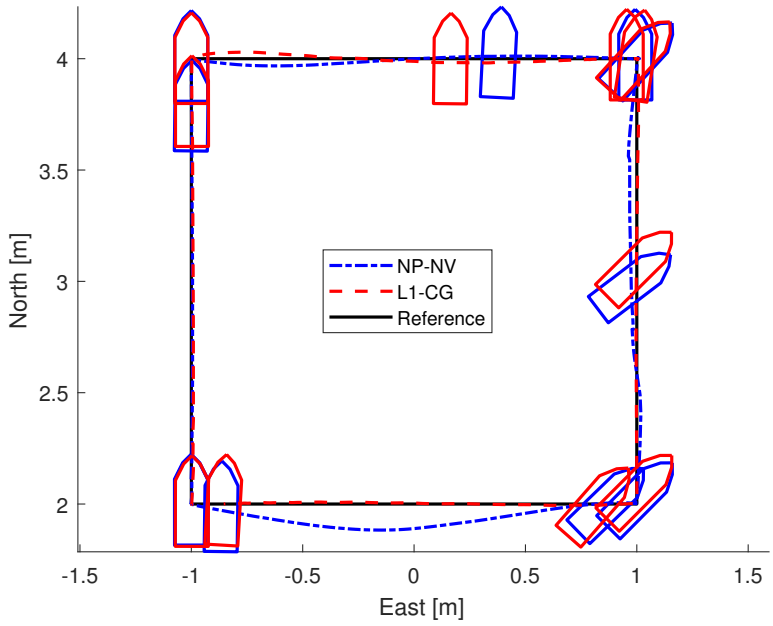

Figure 4.43: $\mathcal{L}_1$ with command governor 4-corner test.

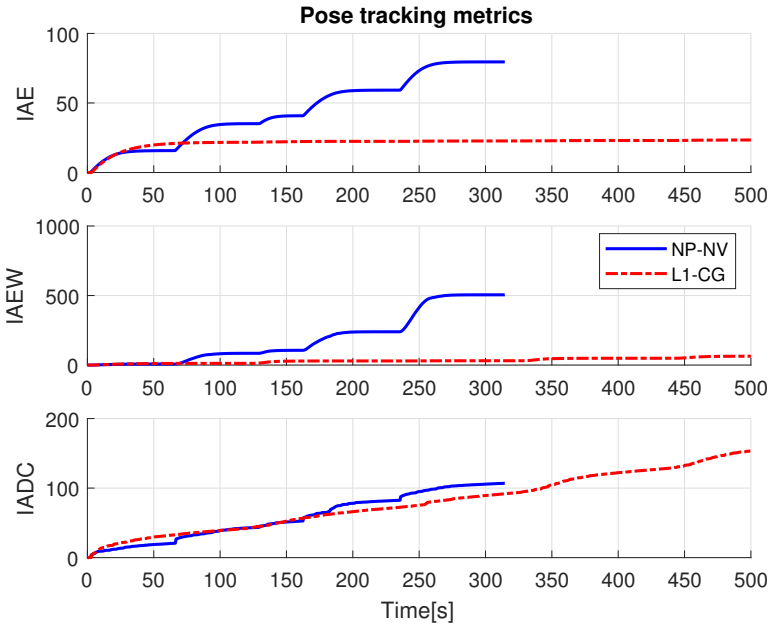

Figure 4.44: $\mathcal{L}_1$ with command governor, Pose error metrics.

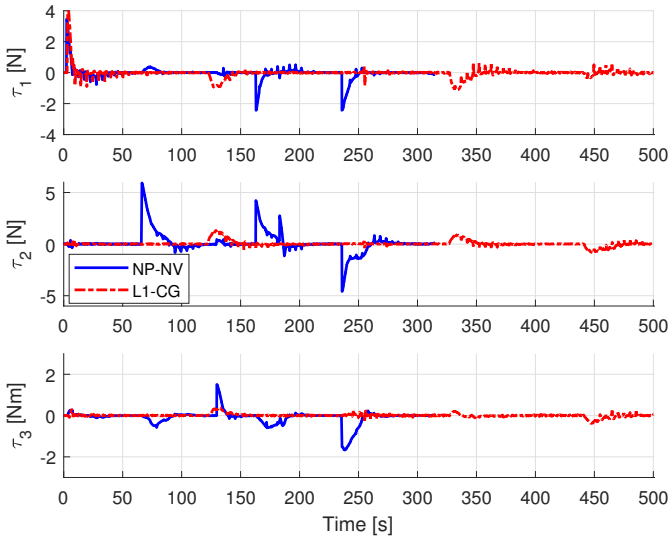

Figure 4.45: $\mathcal{L}_1$ with command governor, Control inputs.

4.4.2 Summary of Lab Session 2

Controller	IAE	IAEW	IADC
$NP-NV$	79	505	107
$\mathcal{L}_1 unconstr.$	76	614	127
$\mathcal{L}_1 MRS$	81	562	**97**
$\mathcal{L}_1 MRS - high$	78	729	115
$\mathcal{L}_1 CG$	**23**	**64**	153

Table 4.7: End values of performance metrics - pose error

Table 4.2 lists the final maximum values for the tested control implementations in lab session 2. The metric values are rounded to the nearest integer for readability, and the lowest values are marked in bold. Plots of the pose transients in each DOF are shown in Appendix.

4.5 Discussion

It is a known behavior for all controllers to slip in North-coordinate during the final $(5 \rightarrow 1)$ coupled motion displayed in Figure 2.7. A notable similarity seen in the $\mathcal{L}_1$ experiments, is that adaptive controller corrects for this error fast, whereas the nominal NP-NV first reduces control error in heading before correcting surge. This is likely due to how the adaptation weights the errors in each DOF.

Comparing the results from the experiments in the lab with the simulations, some notable trends can be seen. Most of the adaptive implementations reduce the overall pose control error compared to the nominal NP-NV, but does so at the cost of higher energy consumption and control rate. The notable exception from this is the I&I adaptive control, which did not prove to work satisfactory in the lab conditions, contrary to what the simulations indicated. When fitting the adaptive controllers with an MRS model, the energy consumption reduces significant not to the level of nominal NP-NV. The control rate metric IADC is also reduced, especially for the first $\mathcal{L}_1$-MRS test in session 2, where IADC is lower than for the nominal. Also, the $\mathcal{L}_1$ has consistently lower experiment run times than NP-NV, an attribute also present in simulations. The reduction of run time can be accounted to how the adaptation contributes to the more realistic model, thus improving the behaviour and run time, in addition to a more aggressive control signal.

The command governor added to $\mathcal{L}_1$ adaptive gives very low IAE and IAEW metrics compared to the other controllers. This can be attributed to how the command governor adjust on the target reference between corners, giving a smoother motion, although slower. The run-time could possibly be reduced by adjusting the transient gains of the command governor, allowing for a faster motion, but at the cost of higher pose error.

When comparing the two lab sessions, a key feature is how the adaptive schemes is affected by measurement noise. With the improved velocity estimator of session 2, both energy consumption and wear & tear is significantly improved, illustrating the need for noise-free measurements.

Plots of the pose transients in each DOF for the experiments in MC-lab are shown in Appendix. The plots show how each controller handles intermittent errors during motions.

4.5.1 Error Sources

As discussed in this chapter, the velocity measurement on the scale model is supplied using an estimator on the position signal. As it is difficult to provide a noise free position signal, it follows that the velocity measurement needed by the control will be affected by this. A possible solution to this could be to use a inertial measurements of an IMU and then calibrating the signal with position measurements at intervals, much like how a real world implemented system uses IMU and GPS signals for positioning. This is beyond the scope of this thesis, but should be investigated in further experimental implementations.

Chapter 5

Conclusions and Future Work

This thesis investigates $\mathcal{L}_1$ adaptive control and Immersion & Invariance adaptive control, two different approaches for adaptive ship control, which are then used to improve the performance on an existing non-adaptive, cascaded nonlinear feedback controller. To account for higher control rate leading to increased actuator wear & tear, MRS and command governor, two methods of actuator handling are then used on the control implementations, thus reducing the combining adaptation with actuator handling to achieve overall improved performance.

A dedicated simulator is developed to mimic lab conditions, and the adaptive control system implementations are tested using this simulator with added noise and uncertainties. To verify performance, the adaptive controllers are further tested laboratory experiments under model-scale conditions in a noisy and uncertain environment. The results show that of the adaptive methods tested, the cascaded $\mathcal{L}_1$ adaptive controller with actuator handling yields the most promising results, having good performance in terms of energy consumption, improving reference tracking and wear & tear. I&I adaptive control has good performance in simulations, but does not work as satisfactory in the lab experiments, most likely due to infeasible control inputs. While adding an adaptive scheme to a controller has shown to reduce control error, it does lead to higher energy consumption. This is a trade-off one needs to consider when using adaptive methods in control applications, even if actuator handling is included.

5.1 Future Work

The implemented simulator setup tries to replicate the noise inherently present in the measurement system in the lab, in addition to implementing a choice of uncertainty parametrizations. To improve the validity of the results, other aspects of the lab could be added. The unknown transport delay present in the position measurement feedback loop should be

identified and replicated. Further signal identification of the noise should also be done in order to represent this in the simulator more accurately.

The simplified novel command governor used in this thesis yields promising results, and could possibly be extended into a nonlinear architecture, thus improving performance of the adaptive schemes.

Immersion & Invariance has potential as an adaptive method for ship motion control, but further designing of the adaptation should be investigates for improved results in experiments. As the implementation in this thesis focuses on uncertainties in the damping matrix, it could be extended to include inertia and centripetal uncertainties.

As discussed and seen in the results, the adaptive schemes are inherently more susceptible to measurement noise. While the derivative filter estimator is a simple method to create the velocity measurement, it is vulnerable to noise in the position measurements, even with the implemented changes in Chapter 4. Effort should be put into developing a model based estimator instead of the modified derivative filter used. As this was beyond the scope of this thesis, it is proposed as further work.

Bibliography

[1] O. N. Lyngstadaas, T. E. Sæterdal, M. E. N. Sørensen, and M. Breivik, "Improvement of ship motion control using a magnitude-rate-saturation model," *in Proceedings of the 2nd IEEE Conference on Control Technology and Applications, Copenhagen, Denmark*, 2018.

[2] J. Bjørnø, *Thruster-Assisted Position Mooring of C/S Inocean Cat I Drillship*. Master thesis, Norwegian University of Science and Technology, Trondheim, Norway, 2016.

[3] O. N. Lyngstadaas, *Ship Motion Control Concepts Considering Actuator Constraints*. Master thesis, Norwegian University of Science and Technology, Trondheim, Norway, 2018.

[4] G. Malara, P. D. Spanos, and F. Arena, "Maximum roll angle estimation of a ship in confused sea waves via a quasi-deterministic approach," *Probabilistic Engineering Mechanics, Volume 35, pp. 75-81*, 2014.

[5] R. Skjetne, M. E. N. Sørensen, M. Breivik, S. A. T. Værnø, A. H. Brodtkorb, A. J. Sørensen, Ø. K. Kjerstad, V. Calabrò, and B. O. Vinje, "AMOS DP research cruise 2016: Academic full-scale testing of experimental dynamic positioning control algorithms onboard R/V Gunnerus," *in Proceedings of the 36th International Conference on Ocean, Offshore and Arctic Engineering OMAE 2017, Trondheim, Norway*, 2017.

[6] NTNU, "Handbook marine cybernetics laboratory," 2017.

[7] M. E. N. Sørensen and M. Breivik, "Comparing combinations of linear and nonlinear feedback terms for motion control of marine surface vessels," *in Proceedings of the 10th IFAC Conference on Control Applications in Marine Systems, Trondheim, Norway*, 2016.

[8] C. Cao and N. Hovakimyan, "Design and analysis of a novel l1 adaptive controller, part i: Control signal and asymptotic stability," *in Proceedings of the 2006 American Control Conference, Minneapolis, USA*, 2006.

[9] C. Cao and N. Hovakimyan, "Design and analysis of a novel l1 adaptive controller,

part ii: Guaranteed transient performance," *in Proceedings of the 2006 American Control Conference, Minneapolis, USA*, 2006.

[10] C. H. Svendsen, N. O. Holck, R. Galeazzi, and M. Blanke, "$\mathcal{L}_1$ adaptive manoeuvring control of unmanned high-speed water craft," *in Proceedings of 9th IFAC Conference on Manoeuvring and Control of Marine Craft, Arenzano, Italy*, 2012.

[11] R. Ren and Z. Zou, "L1 adaptive control used in ship control system when encountering slow varying disturbances," *in Proceedings of the 25th International Ocean and Polar Engineering Conference, Hawaii, USA*, 2015.

[12] V. V. Patel, C. Cao, N. Hovakimyan, K. A. Wise, and E. Lavretsky, "L1 adaptive controller for tailless unstable aircraft in the presence of unknown actuator failures," *International Journal of Control, Volume: 82, Issue: 4, pp. 705-720*, 2009.

[13] T. Yucelen and E. Johnson, "Command governor-based adaptive control," *in Proceedings of AIAA Guidance, Navigation, and Control Conference, Minneapolis, USA*, 2012.

[14] D. Magree, T. Yucelen, and E. Johnson, "Command governor-based adaptive control of an autonomous helicopter," *in Proceedings of AIAA Guidance,Navigation, and Control Conference, Minneapolis, USA*, 2012.

[15] M. E. N. Sørensen and M. Breivik, "Comparing nonlinear adaptive motion controllers for marine surface vessels," *in Proceedings of the 10th IFAC Conference on Manoeuvring and Control of Marine Craft, Copenhagen, Denmark*, 2015.

[16] S. Galeani, S. Onori, A. R. Teel, and L. Zaccarian, "A magnitude and rate saturation model and its use in the soluton of a static anti-windup problem," *Systems & Control Letters, Volume: 57, Issue: 1, pp. 1-9*, 2008.

[17] A. Astolfi and R. Ortega, "Immersion and invariance: a new tool for stabilization and adaptive control of nonlinear systems," *IEEE Transactions on Automatic Control, Volume: 48, Issue: 4*, 2003.

[18] B. Zhao, B. Xian, Y. Zhang, and X. Zhang, "Nonlinear robust adaptive tracking control of a quadrotor uav via immersion and invariance methodology," *IEEE Transactions on Industrial Electronics, Volume: 62, Issue: 5, pp. 2891-2902*, 2015.

[19] T. I. Fossen, *Handbook of Marine Craft Hydrodynamics and Motion Control*. Wiley, 2011.

[20] M. E. N. Sørensen, M. Breivik, and B. O. H. Eriksen, "A ship heading and speed control concept inherently satisfying actuator constraints," *in Proceedings of the 1st IEEE Conference on Control Technology and Applications, HI, USA*, 2017.

[21] J. Bjørnø, H.-M. Heyn, R. Skjetne, A. R. Dahl, and P. Frederich, "Modeling, parameter identification and thruster-assisted position mooring of c/s inocean cat i drillship," *in Proceedings of the ASME 2017 36th International Conference on Ocean, Offshore and Arctic Engineering OMAE 2017, Trondheim, Norway*, 2017.

[22] M. E. N. Sørensen, M. Breivik, and R. Skjetne, "Comparing combinations of linear and nonlinear feedback terms for ship motion control," *submitted to IEEE Transactions on Control Systems Technology*, 2018.

[23] H. Khalil, *Nonlinear Systems*. Prentice Hall, 2002.

[24] A. Loria, "From feedback to cascade-interconnected systems: Breaking the loop," *in Proceedings of the 47th IEEE Conference on Decision and Control, Cancun, Mexico*, 2008.

[25] B.-O. H. Eriksen and M. Breivik, *Modeling, Identification and Control of High-Speed ASVs: Theory and Experiments*, pp. 407–431. Sensing and Control for Autonomous Vehicles: Applications to Land, Water and Air Vehicles, Springer International Publishing, 2017.

Appendices

Appendix A

Appendix

A.1 Lab Session 1 - Transient Plots

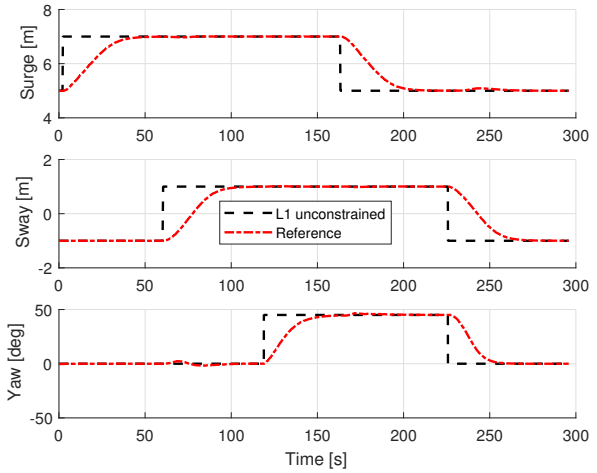

Figure A.1: $\mathcal{L}_1$ unconstrained, Pose transient plot.

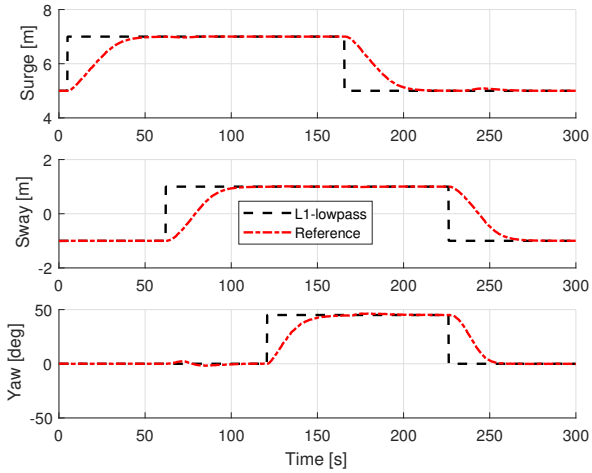

Figure A.2: $\mathcal{L}_1$ lowpass filtered, Pose transient plot.

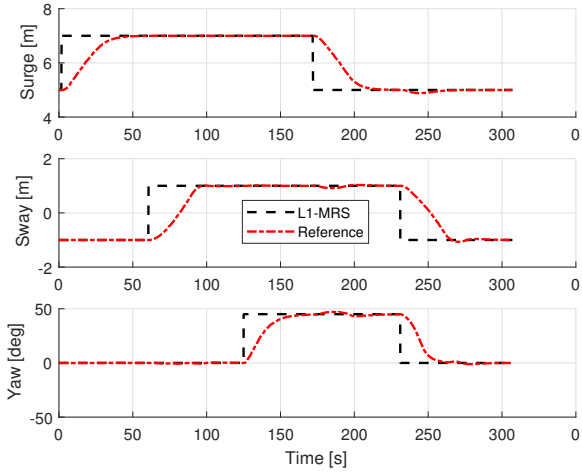

Figure A.3: $\mathcal{L}_1$ with MRS, rate limits factored 1.2, Pose transient plot.

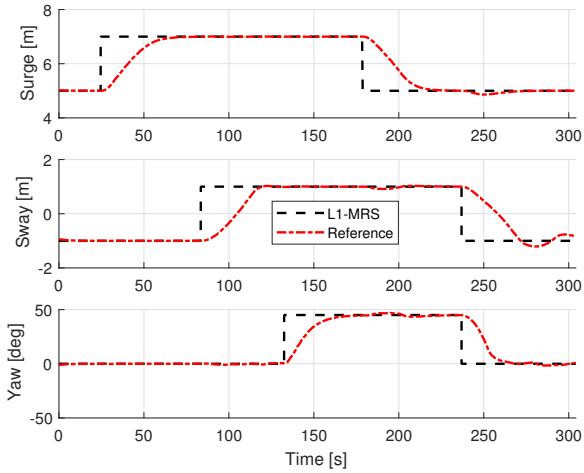

Figure A.4: $\mathcal{L}_1$ with MRS, rate limits factored 1.5, Pose transient plot.

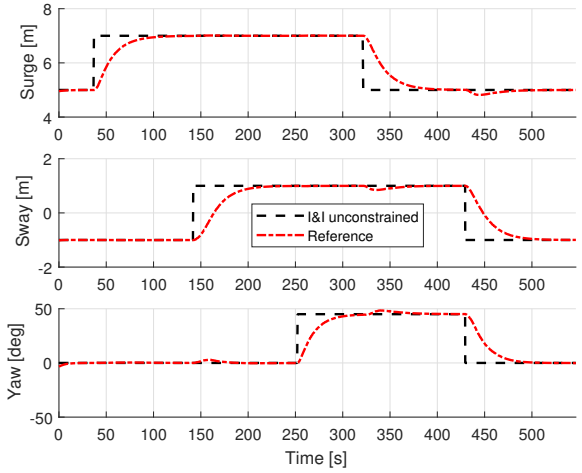

Figure A.5: I&I unconstrained, Pose transient plot.

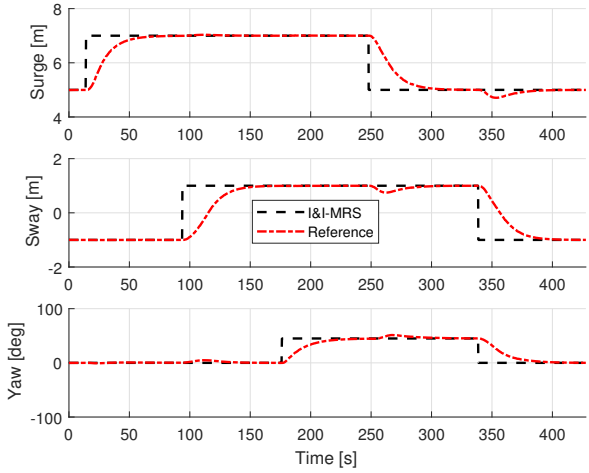

Figure A.6: I&I with MRS, Pose transient plot.

A.2 Lab Session 2 - Transient Plots

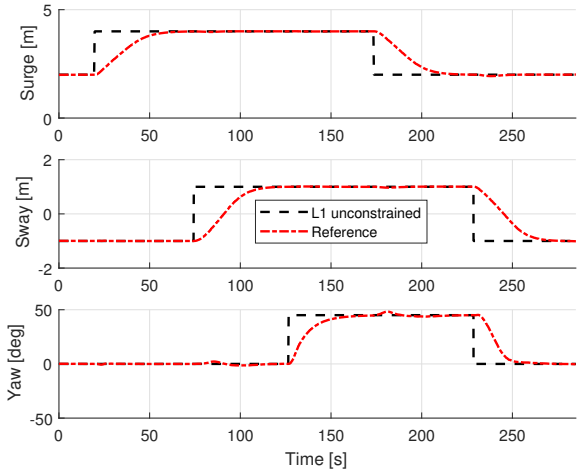

Figure A.7: $\mathcal{L}_1$ unconstrained, Pose transient plot.

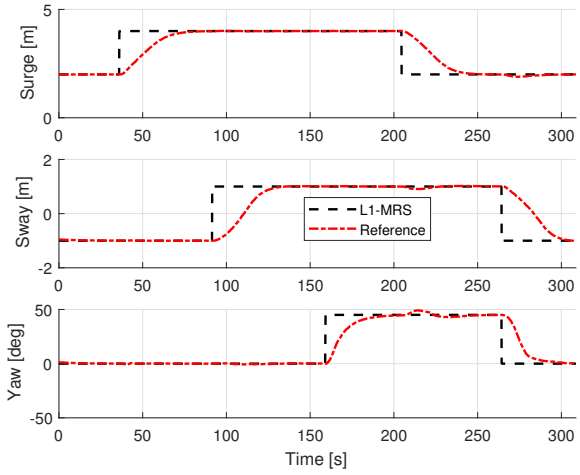

Figure A.8: $\mathcal{L}_1$ with MRS, Pose transient plot.

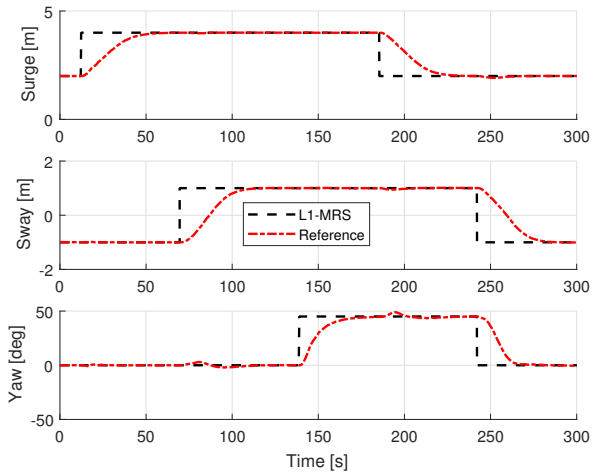

Figure A.9: $\mathcal{L}_1$ with MRS and high magnitude limits, Pose transient plot.

A.3 CSAD Full Model - MATLAB Implementation

```
function nu_dot = CSAD_full(Nu,tau,gamma,sigma,rho)
X_u    = -5.1;
X_uu   = 0;
X_uuu = -18.6312;

Y_v    = -10.16;
Y_vv = -0.8647;
Y_vvv = -665.1745;

Y_r    = -6.25;
Y_rr = -3.65;
Y_rrr = 0;

N_v    = 0;
N_vv = -0.2388;
N_vvv = 0;

N_r    = -14.55;
N_rr = -9.9597;
N_rrr = -0.3101;

N_rv = 0.08;
N_vr = 0.08;
Y_rv = -0.805;
Y_vr = -0.845;
```

```
X_ud =  -10;
Y_vd =  -105;
Y_rd =  -0.525;
N_vd =  -0.157;
N_rd =  -3.4950;

Nur = -Y_rd;
Nuv = -(Y_vd-X_ud);
Yur = -X_ud;

x_g   = 0.0375;
m     = 127.92;
I_z   = 61.967;

u  = Nu(1);
v  = Nu(2);
r  = Nu(3);

d_11 = - X_u - X_uu*abs(u) - X_uuu*u^2;
d_22 = - Y_v - Y_vv*abs(v) - Y_rv*abs(r) - Y_vvv*v^2;
d_23 = - Y_r - Y_rr*abs(r) - Y_vr*abs(v) - Y_rrr*r^2 - Yur*u;
    %With Munk moment
d_32 = - N_v - N_vv*abs(v) - N_rv*abs(r) - N_vvv*v^2 - Nuv*u;
    %With Munk moment
d_33 = - N_r - N_rr*abs(r) - N_vr*abs(v) - N_rrr*r^2 - Nur*u;
    %With Munk moment

D   = [d_11 0   0
       0    d_22 d_23
       0    d_32 d_33];

CA=[0                    0        Y_vd*v+Y_rd*r;
   0                     0            -X_ud*u;
   -Y_rd*r-Y_vd*v        X_ud*u           0];

CRB=[0         0    -m*(x_g*r+v);
    0          0     m*u;
    m*(x_g*r+v) -m*u 0];

C=CRB+CA;

M_RB_c=[m  0     0;
       0    m     m*x_g;
       0    m*x_g I_z];

M_A_c=[-X_ud 0    0;
        0   -Y_vd -Y_rd;
        0   -N_vd -N_rd];

M = M_RB_c + M_A_c;
```

```
M_real = M*gamma; %Uncertainty parametrization
C_real = C*gamma; %Uncertainty parametrization
D_real = D*sigma; %Uncertainty parametrization

nu_dot = M_real\(tau*rho- C_real*Nu - D_real*Nu);
end
```

A.4 Improvement of Ship Motion Control Using a Magnitude-Rate Saturation Model - CCTA2018 Accepted Research Paper

Improvement of Ship Motion Control Using a Magnitude-Rate Saturation Model

Ole Nikolai Lyngstadaas, Tore Egil Sæterdal, Mikkel Eske Nørgaard Sørensen, Morten Breivik

***Abstract*— Motion control concepts for ships have traditionally not focused on handling actuator constraints. This paper investigates the effects on performance of a pair of nonlinear control schemes by developing and implementing a magnitude-rate saturation (MRS) model. The effects of using the MRS model is tested in experiments with a model ship in an ocean basin. Performance metrics are used to evaluate performance in terms of control error, energy efficiency, and actuator wear and tear.**

***Index Terms*— Ship motion control, Magnitude-rate saturation model, Constraint handling, Nonlinear control, Model-scale experiments, Wear and tear**

I. INTRODUCTION

In traditional control theory, an ideal controller might achieve perfect reference tracking in simulations, having no or non-sufficient limitations on the control input. However, in real-life applications it would not be feasible due to limitations in physical output and wear and tear of the actuators.

Several ways of handling actuator constraints have been investigated throughout the years. In [1], model predictive control for systems with actuator magnitude and rate constraints is presented. A solution using a modified dynamic window approach to handle actuator constraints is investigated in [2], and further expanded in [3].

To easily include magnitude and rate saturation (MRS) effects into a control system, a possible low-level approach is to limit the output of the control signal within the limits of the actuators. However, this may lead to an under-damped closed-loop system. To avoid this, effort has been put into implementing a model for combining MRS to smoothen the control output within allowed actuator limits. In [4], an MRS model is derived to address the issue of anti-windup, and the MRS model used in this paper is based on this approach.

In particular, the magnitude and rate saturations in this paper are set at lower limits than the actual actuator constraints. The main purpose is to investigate how limiting the actuator's magnitude and rate outputs will impact the overall performance of the motion control system. The MRS model, depending on how it is tuned, can be implemented in a simulation scenario, where the purpose is to mimic the actual constraints of the system, or be used to limit actuator outputs in laboratory experiments and on-board actual vessels.

O. N. Lyngstadaas and T. E. Sæterdal are M.Sc. students at the Department of Engineering Cybernetics, Norwegian University of Science and Technology (NTNU), NO-7491 Trondheim, Norway. M. E. N. Sørensen and M. Breivik are with the Centre for Autonomous Marine Operations and Systems, Department of Engineering Cybernetics, Norwegian University of Science and Technology (NTNU), NO-7491 Trondheim, Norway. Email: {mikkel.e.n.sorensen, morten.breivik}@ieee.org

The main contribution of this paper are the experimental results from scale testing on a 1:90 ship model. The MRS model from [4] is adapted to a three degrees of freedom (DOF) ship model and experimentally tested at the Marine Cybernetics Laboratory (MC-Lab) at the Norwegian University of Science and Technology (NTNU) in Trondheim, Norway. Furthermore, the positive effects of employing MRS to a pair of nonlinear feedback control schemes from [5] have been investigated.

The rest of this paper is organized as follows: Section II presents a mathematical ship model; Section III defines the control objective and the 4-corner test, derivation of the MRS model, and also presents a pair of nonlinear controllers from [5]; Section IV presents the experimental results from model-scale testing in the MC-Lab, while Section V concludes the paper.

II. SHIP MODEL

The motion of a ship can be represented by the pose vector $\boldsymbol{\eta} = [x, y, \psi]^\top \in \mathbb{R}^2 \times \mathbb{S}$ and the velocity vector $\boldsymbol{\nu} = [u, v, r]^\top \in \mathbb{R}^3$. Here, (x, y) represents the Cartesian position in the local earth-fixed reference frame, ψ is the yaw angle, (u, v) represents the body-fixed linear velocities and r is the yaw rate. The 3-DOF dynamics of a ship can then be stated as in [6]:

$$\dot{\boldsymbol{\eta}} = \boldsymbol{R}(\psi)\boldsymbol{\nu} \tag{1}$$

$$\boldsymbol{M}\dot{\boldsymbol{\nu}} + \boldsymbol{C}(\boldsymbol{\nu})\boldsymbol{\nu} + \boldsymbol{D}(\boldsymbol{\nu})\boldsymbol{\nu} = \boldsymbol{\tau}, \tag{2}$$

where $\boldsymbol{M} \in \mathbb{R}^{3\times3}$, $\boldsymbol{C}(\boldsymbol{\nu}) \in \mathbb{R}^{3\times3}$, $\boldsymbol{D}(\boldsymbol{\nu}) \in \mathbb{R}^{3\times3}$ and $\boldsymbol{\tau} = [\tau_1, \tau_2, \tau_3]^\top$ represent the inertia matrix, Coriolis and centripetal matrix, damping matrix and control input vector, respectively. The rotation matrix $\boldsymbol{R}(\psi) \in SO(3)$ is given by

$$\boldsymbol{R}(\psi) = \begin{bmatrix} \cos(\psi) & -\sin(\psi) & 0 \\ \sin(\psi) & \cos(\psi) & 0 \\ 0 & 0 & 1 \end{bmatrix}. \tag{3}$$

The system matrices are assumed to satisfy the properties $\boldsymbol{M} = \boldsymbol{M}^\top > 0$, $\boldsymbol{C}(\boldsymbol{\nu}) = -\boldsymbol{C}(\boldsymbol{\nu})^\top$ and $\boldsymbol{D}(\boldsymbol{\nu}) > 0$.

A. Nominal model

The model and parameters of the model-scale ship C/S Inocean Cat I Drillship (CSAD) [7], as shown in Fig. 1, will be used in this paper. CSAD is a 1:90 scale replica of a supply ship, with a length of $L = 2.578$ m. The inertia matrix is given as

$$\boldsymbol{M} = \boldsymbol{M}_{RB} + \boldsymbol{M}_A, \tag{4}$$

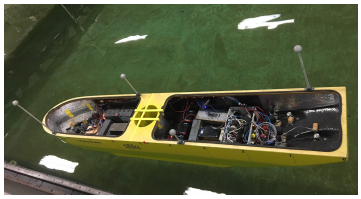

Fig. 1: C/S Inocean Cat I Drillship in the MC-lab.

where

$$\boldsymbol{M}_{RB} = \begin{bmatrix} m & 0 & 0 \\ 0 & m & mx_g \\ 0 & mx_g & I_z \end{bmatrix} \tag{5}$$

$$\boldsymbol{M}_{A} = \begin{bmatrix} -X_{\dot{u}} & 0 & 0 \\ 0 & -Y_{\dot{v}} & -Y_{\dot{r}} \\ 0 & -N_{\dot{v}} & -N_{\dot{r}} \end{bmatrix}. \tag{6}$$

The mass of CSAD is $m = 127.92$ kg, while $x_g = 0.00375$ m is the distance along the x-axis in the body frame from the centre of gravity, and $I_z = 61.987\ \mathrm{kg\,m^2}$ is the moment of inertia about the z-axis in the body frame. Other parameter values are listed in Table I, which are updated values from [7], where a few changes to the numerical values and signs have been done to better fit the actual laboratory performance of CSAD.

CSAD has six azimuth thrusters, which in the experiments presented here are fixed to the angles $\boldsymbol{\delta} = [\pi, \pi/4, -\pi/4, 0, 5\pi/4, 3\pi/4]^\top$ rad, in the body-fixed coordinate system, giving a fully actuated vessel [3].

The Coriolis and centripetal matrix is

$$\boldsymbol{C}(\boldsymbol{\nu}) = \boldsymbol{C}_{RB}(\boldsymbol{\nu}) + \boldsymbol{C}_{A}(\boldsymbol{\nu}), \tag{7}$$

with

$$\boldsymbol{C}_{RB}(\boldsymbol{\nu}) = \begin{bmatrix} 0 & 0 & -m(x_g r + v) \\ 0 & 0 & mu \\ m(x_g r + v) & -mu & 0 \end{bmatrix} \tag{8}$$

$$\boldsymbol{C}_{A}(\boldsymbol{\nu}) = \begin{bmatrix} 0 & 0 & -c_{A,13}(\boldsymbol{\nu}) \\ 0 & 0 & c_{A,23}(\boldsymbol{\nu}) \\ c_{A,13}(\boldsymbol{\nu}) & -c_{A,23}(\boldsymbol{\nu}) & 0 \end{bmatrix}, \tag{9}$$

where

$$c_{A,13}(\boldsymbol{\nu}) = -Y_{\dot{r}} r - Y_{\dot{v}} v \tag{10}$$

$$c_{A,23}(\boldsymbol{\nu}) = -X_{\dot{u}} u. \tag{11}$$

Finally, the damping matrix $\boldsymbol{D}(\boldsymbol{\nu})$ is given as

$$\boldsymbol{D}(\boldsymbol{\nu}) = \boldsymbol{D}_{L} + \boldsymbol{D}_{NL}(\boldsymbol{\nu}), \tag{12}$$

where

$$\boldsymbol{D}_{L} = \begin{bmatrix} -X_u & 0 & 0 \\ 0 & -Y_v & -Y_r \\ 0 & -N_v & -N_r \end{bmatrix} \tag{13}$$

TABLE I: Parameters for CSAD, updated from [7].

Parameter	Value	Parameter	Value
$X_{\dot{u}}$	-3.262	$Y_{\|r\|r}$	-3.450
$Y_{\dot{v}}$	-28.890	Y_{rrr}	0
$Y_{\dot{r}}$	-0.525	N_r	-6.916
$N_{\dot{v}}$	-0.157	$N_{\|r\|r}$	-4.734
$N_{\dot{r}}$	-13.980	N_{rrr}	-0.147
X_u	-2.332	N_v	0
$X_{\|u\|u}$	0	$N_{\|v\|v}$	-0.209
X_{uuu}	-8.557	N_{vvv}	0
Y_v	-4.673	$N_{\|r\|v}$	0.080
$Y_{\|v\|v}$	-0.398	$N_{\|v\|r}$	0.080
Y_{vvv}	-313.300	$Y_{\|r\|v}$	-0.805
Y_r	-7.250	$Y_{\|v\|r}$	-0.845

$$\boldsymbol{D}_{NL}(\boldsymbol{\nu}) = \begin{bmatrix} d_{NL,11}(\boldsymbol{\nu}) & 0 & 0 \\ 0 & d_{NL,22}(\boldsymbol{\nu}) & d_{NL,23}(\boldsymbol{\nu}) \\ 0 & d_{NL,32}(\boldsymbol{\nu}) & d_{NL,33}(\boldsymbol{\nu}) \end{bmatrix}, \tag{14}$$

with

$$d_{NL,11}(\boldsymbol{\nu}) = -X_{|u|u}|u| - X_{uuu}u^2 \tag{15}$$

$$d_{NL,22}(\boldsymbol{\nu}) = -Y_{|v|v}|v| - Y_{|r|v}|v| - Y_{vvv}v^2 \tag{16}$$

$$d_{NL,23}(\boldsymbol{\nu}) = -Y_{|r|r}|r| - Y_{|v|r}|v| - Y_{rrr}v^2 - Y_{ur}u \tag{17}$$

$$d_{NL,32}(\boldsymbol{\nu}) = -N_{|v|v}|v| - N_{|r|v}|r| - N_{vvv}v^2 - N_{uv}u \tag{18}$$

$$d_{NL,33}(\boldsymbol{\nu}) = -N_{|r|r}|v| - N_{|v|r}|v| - N_{rrr}r^2 - N_{ur}u, \tag{19}$$

where

$$Y_{ur} = X_{\dot{u}} \tag{20}$$

$$N_{uv} = -(Y_{\dot{v}} - X_{\dot{u}}) \tag{21}$$

$$N_{ur} = Y_{\dot{r}}, \tag{22}$$

which are damping terms which are linearly increasing with the forward speed. These are added to compensate for the Munk moment, and to get a more physically realistic model behavior [2], [8].

III. CONTROL DESIGN

A. Control objective and 4-corner test

The main control objective is to make $\tilde{\boldsymbol{\eta}}(t) \triangleq \boldsymbol{\eta}(t) - \boldsymbol{\eta}_t(t) \to \boldsymbol{0}$ $t \to \infty$, where $\boldsymbol{\eta}_t(t) = [x_t(t), y_t(t), \psi_t(t)]^\top \in \mathbb{R}^2 \times \mathbb{S}$ represents the pose associated with a target point. The motion of the target is typically defined by a human or generated by a guidance system. For notational simplicity, time t will mostly be omitted for the rest of the paper.

It is desirable to investigate the effect of the magnitude-rate saturation model during different ship maneuvers. For this reason, a 4-corner maneuvering test is used, as shown in Fig. 2. For comparison, the experiments will be conducted with and without using the MRS model to identify notable effects on performance.

The 4-corner maneuvering test is proposed in [9] as a way to compare ship performance of dynamic positioning control algorithms. The ship is first initialized in dynamic positioning to point straight North at heading $0\,(deg)$. Then the following setpoint changes are commanded:

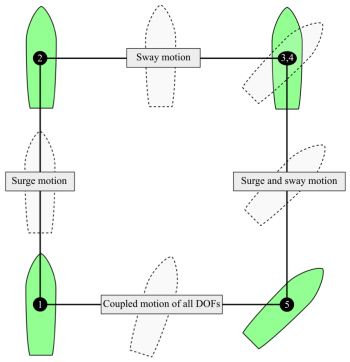

Fig. 2: The 4-corner dynamic positioning test. Modified from [9].

- Position change $2\,(m)$ straight North: tests a pure surge movement ahead.
- Position change $2\,(m)$ straight East: tests a pure sway movement in the starboard direction.
- Heading change $45\,(deg)$ clockwise: tests a pure yaw motion while keeping position steady.
- Position change $2\,(m)$ straight South: tests a combined surge-sway movement while keeping heading steady.
- Position change $2\,(m)$ straight West and heading change $45\,(deg)$ counterclockwise: tests a combined surge-sway-yaw movement.

B. Magnitude-rate saturation model design

Modelling the vessel's actuator constraints is important to ensure that the controller output remains inside a feasible range of values. Both magnitude and rate constraints will impact a vessel's ability to maneuver, and should be handled in the control system.

1) Saturation modeling: A generalized saturation block for an actuator can be modeled as

$$\tau_{s,i}(\tau_i) = \begin{cases} \tau_{i,min} & \text{if } \tau_i \leq \tau_{i,min} \\ \tau_i & \text{if } \tau_{i,min} < \tau_i < \tau_{i,max}, \quad \forall i \in \{1,2,3\}, \\ \tau_{i,max} & \text{if } \tau_i \geq \tau_{i,max} \end{cases} \tag{23}$$

where τ_i is the commanded control input without saturation with $i \in \{1,2,3\}$ to control surge, sway and yaw forces and moment, respectively. The saturation limits are represented by $\boldsymbol{\tau}_{min} = [\tau_{1,min}, \tau_{2,min}, \tau_{3,min}]^\top$ and $\boldsymbol{\tau}_{max} = [\tau_{1,max}, \tau_{2,max}, \tau_{3,max}]^\top$ with negative and positive bounded elements, respectively.

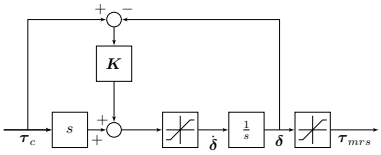

Fig. 3: Block diagram for the MRS model (24).

2) Magnitude-rate saturation model: An approach to model the MRS effects is given by

$$\dot{\boldsymbol{\delta}} = sat_{\boldsymbol{r}}(\dot{\boldsymbol{\tau}}_c + \boldsymbol{K}(\boldsymbol{\tau_c} - \boldsymbol{\delta})) \tag{24}$$

$$\boldsymbol{\tau}_{mrs} = sat_{\boldsymbol{m}}(\boldsymbol{\delta}), \tag{25}$$

where $\boldsymbol{\tau}_c$, $\boldsymbol{\delta}$ and $\boldsymbol{\tau}_{mrs}$ are the input, state and output of the MRS model, respectively, and where $\boldsymbol{K} > 0$ is a diagonal tuning matrix. The matrix is introduced in order to avoid an unstable cancellation between the derivative operator s and the integrator in Fig. 3, where the block diagram for the MRS model is shown. Because of this, an important observation is that neither of the elements of the matrix $\boldsymbol{K}$ can be equal to 1, and thus also $\boldsymbol{K} \neq \boldsymbol{I}$. The gain matrix $\boldsymbol{K}$ affects the speed of the inner-loop in the MRS model, and should be chosen based on the desired tracking performance. The derivative of the input, $\dot{\boldsymbol{\tau}}_c$, is supposed to exist and can be calculated using numerical derivation. The saturation limits $sat_{\boldsymbol{r}}$ and $sat_{\boldsymbol{m}}$ are modeled as the saturation block above, and contain the vessel's rate and magnitude constraints, respectively. See [4] for further details.

In this setup, the rate is limited first and the magnitude next, meaning that the MRS model state $\boldsymbol{\delta}$ can exceed the magnitude-bounds vector $\boldsymbol{m}$, although the output $\boldsymbol{\tau}_{mrs}$ never does. It should also be noted that this model can be further extended to effectively solve anti-windup problems, should such effects be needed to be accounted for.

C. Nonlinear control design

The MRS model will be tested with two types of feedback controllers in order to investigate the impact on performance for both linear and nonlinear feedback terms.

1) Nonlinear pose and linear velocity feedbacks: Using a control scheme based on a combination of nonlinear feedback of pose and linear feedback of velocity from [5], the control input can be chosen as

$$\boldsymbol{\tau} = \boldsymbol{M}\dot{\boldsymbol{\alpha}} + \boldsymbol{C}(\boldsymbol{\nu})\boldsymbol{\alpha} + \boldsymbol{D}(\boldsymbol{\nu})\boldsymbol{\alpha} - \boldsymbol{\Gamma}_2\boldsymbol{z}_2, \tag{26}$$

where

$$\dot{\boldsymbol{\alpha}} = \boldsymbol{R}^\top(\psi)\ddot{\boldsymbol{\eta}}_t + \boldsymbol{S}(r)^\top\boldsymbol{R}^\top(\psi)\dot{\boldsymbol{\eta}}_t - \dot{\boldsymbol{K}}_1(\cdot)\boldsymbol{z}_1 - \boldsymbol{K}_1(\cdot)\dot{\boldsymbol{z}}_1, \tag{27}$$

with $\boldsymbol{\Gamma}_2 > 0$ and where

$$\boldsymbol{S}(r) = \begin{bmatrix} 0 & -r & 0 \\ r & 0 & 0 \\ 0 & 0 & 0 \end{bmatrix}. \tag{28}$$

Here, the error variables $\boldsymbol{z}_1 = [z_{1,x}, z_{1,y}, z_{1,\psi}]^\top$ and $\boldsymbol{z}_2 = [z_{2,u}, z_{2,v}, z_{2,r}]^\top$ are defined as

$$\boldsymbol{z}_1 \triangleq \boldsymbol{R}(\psi)(\boldsymbol{\eta} - \boldsymbol{\eta}_t) \tag{29}$$

$$\boldsymbol{z}_2 \triangleq \boldsymbol{\nu} - \boldsymbol{\alpha}, \tag{30}$$

where $\boldsymbol{\alpha} \in \mathbb{R}^3$ is a vector of stabilizing functions, which can be interpreted as a desired velocity. As in [5], $\boldsymbol{\alpha}$ can be chosen as

$$\boldsymbol{\alpha} = \boldsymbol{R}^\top(\psi)\dot{\boldsymbol{\eta}}_{\boldsymbol{t}} - \boldsymbol{K}_1(\cdot)\boldsymbol{z}_1, \tag{31}$$

with the nonlinear feedback term $\boldsymbol{K}_1(\cdot)$ chosen as

$$\boldsymbol{K_1}(\cdot) = \boldsymbol{\Gamma}_1 \begin{bmatrix} \dfrac{1}{\sqrt{\boldsymbol{z}_{1,\tilde{p}}^\top \boldsymbol{z}_{1,\tilde{p}} + \Delta_{\tilde{p}}^2}} \boldsymbol{I}_{2\times 2} & \boldsymbol{0}_{2\times 1} \\ \boldsymbol{0}_{1\times 2} & \dfrac{1}{\sqrt{z_{1,\tilde{\psi}}^2 + \Delta_{\tilde{\psi}}^2}} \end{bmatrix}, \tag{32}$$

where $\boldsymbol{z}_{1,\tilde{p}} = [z_{1,x}, z_{1,y}]^\top$, $\boldsymbol{\Gamma}_1 > 0$ and $\Delta_i > 0$ are tuning parameters. Furthermore, $\dot{\boldsymbol{K}}_1(\cdot)$ is given by

$$\dot{\boldsymbol{K}}_1(\cdot) = -\boldsymbol{\Gamma}_1 \begin{bmatrix} \dfrac{\boldsymbol{z}_{1,\tilde{p}}^\top \dot{\boldsymbol{z}}_{1,\tilde{p}}}{(\boldsymbol{z}_{1,\tilde{p}}^\top \boldsymbol{z}_{1,\tilde{p}} + \Delta_{\tilde{p}}^2)^{\frac{3}{2}}} \boldsymbol{I}_{2\times 2} & \boldsymbol{0}_{2\times 1} \\ \boldsymbol{0}_{1\times 2} & \dfrac{z_{1,\tilde{\psi}}\dot{z}_{1,\tilde{\psi}}}{(z_{1,\tilde{\psi}}^2 + \Delta_{\tilde{\psi}}^2)^{\frac{3}{2}}} \end{bmatrix}. \tag{33}$$

2) Nonlinear pose and velocity feedbacks: The other control scheme from [5] augments (26) with a nonlinear velocity feedback term, giving the control input

$$\boldsymbol{\tau} = \boldsymbol{M}\dot{\boldsymbol{\alpha}} + \boldsymbol{C}(\boldsymbol{\nu})\boldsymbol{\alpha} + \boldsymbol{D}(\boldsymbol{\nu})\boldsymbol{\alpha} - \boldsymbol{K}_2(\cdot)\boldsymbol{z}_2, \tag{34}$$

where $\dot{\boldsymbol{\alpha}}$ and $\boldsymbol{\alpha}$ are given by (27) and (31), respectively, and with the nonlinear feedback term $\boldsymbol{K}_2(\cdot)$ chosen as

$$\boldsymbol{K_2}(\cdot) = \boldsymbol{\Gamma}_2 \begin{bmatrix} \dfrac{1}{\sqrt{\boldsymbol{z}_{2,\tilde{r}}{}^\top \boldsymbol{z}_{2,\tilde{v}} + \Delta_{\tilde{v}}^2}} \boldsymbol{I}_{2\times 2} & \boldsymbol{0}_{2\times 1} \\ \boldsymbol{0}_{1\times 2} & \dfrac{1}{\sqrt{z_{2,\tilde{r}^2} + \Delta_{\tilde{r}}^2}} \end{bmatrix}, \tag{35}$$

where $\boldsymbol{z}_{2,\tilde{v}} = [z_{2,u}, z_{2,v}]^\top$ and $\Delta_i > 0$ are tuning parameters. The feedback gain $\boldsymbol{\Gamma}_2$ is the same matrix as in (26).

The nonlinear pose and linear velocity feedback controller and the nonlinear pose and velocity feedback controller will be abbreviated NP-LV and NP-NV, respectively, throughout the rest of this paper.

TABLE II: Control gains.

	NP-LV	**NP-NV**
$\boldsymbol{\Gamma}_1$	diag($[0.08, 0.08, 0.0698]$)	$-\|\|-$
$\boldsymbol{\Gamma}_2$	diag($[0.2, 0.2, 0.1745]$)$\boldsymbol{M}$	$-\|\|-$
$\Delta_{\tilde{p}}$	0.5	$-\|\|-$
$\Delta_{\tilde{\psi}}$	0.5	$-\|\|-$
$\Delta_{\tilde{v}}$	–	0.7
$\Delta_{\tilde{r}}$	–	1
$\boldsymbol{K}$	diag($[4, 3, 2]$)	$-\|\|-$

3) Stability: Based on the theorems and stability proofs in [10], we can conclude that the two controllers have the following stability properties: The origin $(\boldsymbol{z}_1, \boldsymbol{z}_2) = (\boldsymbol{0}, \boldsymbol{0})$ is uniformly globally asymptotically stable (UGAS) and on each compact set $B \subset \mathbb{R}^6$ containing the origin, it is uniformly exponentially stable (UES) [10]. The MRS model is a nonlinear filter, and it is proven in [4] that the output will be an $\mathcal{L}_2$ signal if the input is an $\mathcal{L}_2$ signal, so it can be concluded that the MRS model does not alter the stability properties of the system.

4) Parameter tuning: The experiments are conducted with the gain parameters shown in Table II. The choice of the gain parameters for the two controllers are based on the tuning rules described in [10]. Here, the goal is to make the kinetic subsystem faster than the kinematic subsystem, which means that the kinetic subsystem needs to have smaller time constants than the kinematic subsystem in the linear region. The Δ-values scale the linear feedback gains and therefore the resulting time constants of the linear region, and must therefore be chosen such that they do not make the kinematic subsystem faster than the kinetic subsystem.

The actuator saturation limits are chosen by the following set of suggested tuning rules as well [11]. Here, the magnitude saturation limits are set lower than the actual limitations in order to save energy, and chosen as $\boldsymbol{m} = [2, 1.5, 1]$. The rate saturation limits are chosen by $\boldsymbol{r} = [m_1/t_{mrs,1}, m_2/t_{mrs,2}, m_3/t_{mrs,3}]^\top$, where m_1, m_2 and m_3 are the magnitude saturation limits given by $\boldsymbol{m}$, and where $t_{mrs,1}$, $t_{mrs,2}$ and $t_{mrs,3}$ are the desired transition times for the actuators to go from zero to max thrust in surge, sway and yaw, respectively. Here, suitable values for the rate saturation limits were found to be $\boldsymbol{r} = [1.9, 1.1, 0.8]$. Then, the gain matrix $\boldsymbol{K}$ can be chosen by $\boldsymbol{K} = \text{diag}([K_{1,1}, \frac{m_2}{m_1}K_{1,1}, \frac{m_3}{m_1}K_{1,1}])$, where under normal operations it is desired to have all the diagonal elements $\boldsymbol{K}_{i,i} > 1$, $\forall i \in \{1, 2, 3\}$. Here, $K_{1,1} = 4$ to ensure a fast tracking of the target signal in all three degrees of freedom. The block diagram for the full control system is shown in Fig. 4.

IV. EXPERIMENTAL RESULTS AND PERFORMANCE EVALUATION

A. Marine Cybernetics Laboratory

As already mentioned, the MC-Lab is a small ocean basin at NTNU. Due to its relatively small size and advanced instrumentation package, the facility is especially suited for

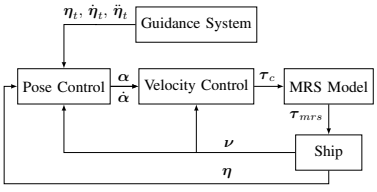

Fig. 4: Block diagram for the ship control system.

tests of motion control systems for marine vessel models, but is also suitable for more specialized hydrodynamic tests due to the advanced towing carriage, which has capability for precise movement of models up to six degrees of freedom [12].

The experiments will be conducted under the following conditions: In the experiments, the actual model ship's $\boldsymbol{M}$, $\boldsymbol{C}$ and $\boldsymbol{D}$ matrices will differ somewhat from those used in the controllers. Also, measurement noise is present in the Qualisys motion tracking system used in the laboratory.

B. Performance metrics

Performance metrics are used to objectively compare the performance of different control schemes. In this paper, the error variable is defined as the scaled norm of the pose control error $\boldsymbol{z}_1$, such that

$$e = \sqrt{\tilde{\boldsymbol{z}}_1^\top \tilde{\boldsymbol{z}}_1}, \tag{36}$$

where

$$\tilde{\boldsymbol{z}}_1 = [\frac{z_{1,x}}{4}, \frac{z_{1,y}}{4}, \frac{z_{1,\psi}}{\pi/2}]^\top. \tag{37}$$

Since the position and yaw angle in pose have different units, we have defined the normalized pose error signals $\tilde{z}_{1,x}$, $\tilde{z}_{1,y}$ and $\tilde{z}_{1,\psi}$ on the intervals $[-0.5, 0.5]$ in the expected operational space of the ship [13]. To get this interval, the position errors are divided by 4 and the yaw error is divided by $\frac{\pi}{2}$, since the position errors are in the intervals $[-2, 2]$ and the yaw error is in the interval $[-\frac{\pi}{4}, \frac{\pi}{4}]$, resulting in the normalized control error e.

Three different performance metrics are used in this paper, namely IAE, IAEW and IADC. The IAE (integral of the absolute error) metric is defined as an unweighted integral over time:

$$IAE(t) = \int_0^t |e(\gamma)|\, d\gamma. \tag{38}$$

The IAEW (integral of the absolute error multiplied by energy consumption) metric scales IAE by the energy consumption

$$IAEW(t) = \int_0^t |e(\gamma)|\, d\gamma \int_0^t P(\gamma) d\gamma, \tag{39}$$

where $P = \left|\boldsymbol{\nu}^\top \boldsymbol{\tau}\right|$, thus yielding a measure of energy efficiency.

Since the aim of the MRS model is also to reduce actuator wear and tear, it is interesting to investigate the dynamic behavior of the control signal. The IADC (integral of absolute differentiated control) metric is defined as in [13]:

$$IADC(t) = \int_{t_0}^t |\dot{\bar{\tau}}(\gamma)|\, d\gamma, \tag{40}$$

with $\bar{\tau}(t) = \sqrt{\boldsymbol{\tau}^\top \boldsymbol{\tau}}$, and where $\dot{\bar{\tau}}$ is computed using numerical derivation.

C. Experimental results

In the experiments, the target pose changes between setpoints for the 4-corner test. The system is implemented such that the target will automatically change to the next setpoint when the ship is within 0.003 m from the target in both x and y direction and 0.2 deg from the target heading. When the 4-corner test is completed, the ship will have returned accurately to its initial position and heading, ready for a new test at the same pose and along the same track.

While CSAD has a length of $L = 2.578$ m, its outline has been scaled by 1:6 in the 4-corner plots in Fig. 5 and 8, to better display the ship behaviour. By the plotted values of the performance metrics in Fig. 6 and 9, the effects of the MRS model on control performance can be examined. Fig. 5 shows the 4-corner track and the actual trajectory for the CSAD with and without the MRS model applied to the NP-LV controller. The results show no remarkable difference in the trajectory.

The performance metrics are plotted in Fig. 6. The metrics show that the while MRS does not reduce the overall tracking error by the IAE metric, both energy consumption (IAEW) and actuator wear and tear (IADC) are reduced by 6.8% and 38.8%, respectively.

In Fig. 7, the commanded thrust signals are shown for the 4-corner test. It can be seen that the MRS contributes to a smoother and amplitude-wise smaller control signal, while achieving approximately the same tracking performance. The spikes that can be seen in the control signal, especially during transients, are caused by noise related to the velocity estimation.

Fig. 8 displays the 4-corner trajectory for the NP-NV controller. Even though the NP-NV-controlled vessel with MRS effects takes a wider arch in the coupled motion ($5 \rightarrow 1$) in Fig. 2, the overall tracking error is not increased, as seen in Table III.

Furthermore, Fig. 9 shows improvement in energy efficiency, shown by the IAEW metric, and lower actuator wear and tear through the IADC metric. The reduction is greater for the NP-NV controller than the NP-LV controller, which is due to the fact the NP-NV is inherently a more aggressive controller, and thus benefits more from using an MRS model. For the NP-NV controller, the reduction is 12.2% and 46.4% for IAEW and IADC, respectively.

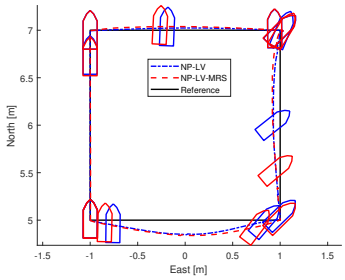

Fig. 5: Vessel performing the 4-corner manoeuver using the NP-LV controller.

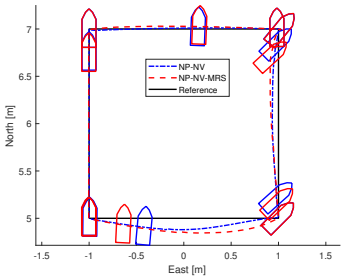

Fig. 8: Vessel performing the 4-corner maneuver using the NP-NV controller.

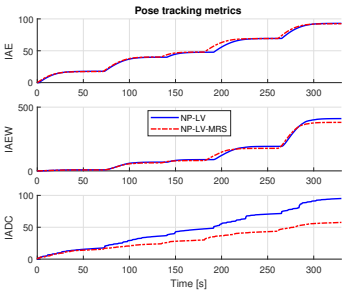

Fig. 6: Performance metrics for NP-LV.

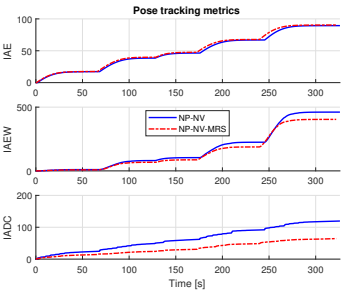

Fig. 9: Performance metrics for NP-NV.

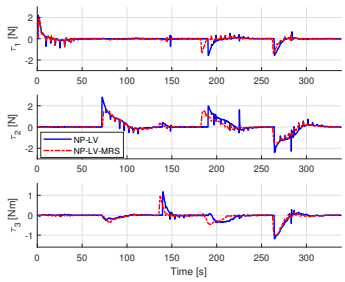

Fig. 7: Commanded control input for NP-LV.

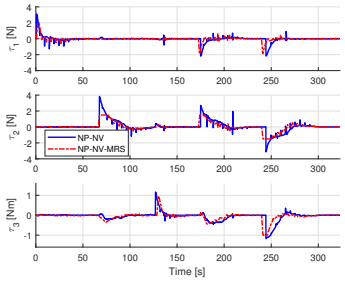

Fig. 10: Commanded control input for NP-NV.

TABLE III: Performance metrics final values.

	NP-LV	NP-LV MRS	NP-NV	NP-NV MRS
IAE final	92.99	**92.85**	**89.49**	90.38
IAEW final	410.12	**382.23**	460.08	**403.79**
IADC final	95.99	**58.73**	118.26	**63.34**

Fig. 10 shows the commanded control inputs for the NP-NV controller. Similar to NP-LV, a smoothing effect can be observed, although less significant. This is likely due to the nature of the pure nonlinear feedback, giving overall better tracking performance, which has previously been discussed in [5].

A significant effect of the MRS model, which can be seen in the performance metrics in Fig. 6 and 9, is that it results in a significantly reduced rate of change in the commanded control input.

The final values for the performance metrics are displayed in Table III, where the best performing controller for the different metrics is noted in bold.

V. CONCLUSION

Depending on the type of controller that is being used, including an MRS model to limit the actuator magnitude and rate outputs can contribute positively in several ways. As seen in both cases presented, an MRS model can effectively reduce actuator twitching, and thus wear and tear, without the degradation of performance in ship control. In addition, it has the potential to improve overall energy efficiency and pose tracking abilities, as can be seen from the performance metrics and trajectory plots, and can thus have positive effects on ship performance in setpoint navigation. These effects are especially important for vessels which must operate for long times at sea, and can be particularly useful for ships in DP operations, effectively contributing to the longevity of the operation with a reduced need for maintenance and repairs.

Future work includes optimizing the MRS model to further improve performance. This includes, through experimental tests in a laboratory, further tuning of the gain matrix $\boldsymbol{K}$ and the desired magnitude and rate saturation effects to obtain optimal ship control for the wanted ship operational environment.

ACKNOWLEDGEMENTS

This work was supported by the Research Council of Norway through the Centres of Excellence funding scheme, project number 223254. The authors gratefully acknowledge senior engineer Torgeir Wahl and Ph.D. candidate Andreas R. Dahl at NTNU's Department of Marine Technology for valuable support during the experiments.

REFERENCES

[1] V. Kapila and S. Valluri, "Model predictive control of systems with actuator amplitude and rate saturation," *in Proceedings of the 37th IEEE Conference on Decision and Control, pp. 1396-1401*, 1998.

[2] M. E. N. Sørensen, M. Breivik, and B.-O. H. Eriksen, "A ship heading and speed control concept inherently satisfying actuator constraints," *in Proceedings of the 1st IEEE Conference on Control Technology and Applications, HI, USA*, 2017.

[3] M. E. N. Sørensen, O. N. Lyngstadaas, B.-O. H. Eriksen, and M. Breivik, "A dynamic window-based controller for dynamic positioning satisfying actuator magnitude constraints," *in Proceedings of the 11th IFAC Conference on Control Applications in Marine Systems, Robotics, and Vehicles, Opatija, Croatia*, 2018.

[4] S. Galeani, S. Onori, A. R. Teel, and L. Zaccarian, "A magnitude and rate saturation model and its use in the soluton of a static anti-windup problem," *Systems & Control Letters, Volume 57, Issue 1, pp. 1-9*, 2008.

[5] M. E. N. Sørensen and M. Breivik, "Comparing combinations of linear and nonlinear feedback terms for motion control of marine surface vessels," *in Proceedings of the 10th IFAC Conference on Control Applications in Marine Systems, Trondheim, Norway*, 2016.

[6] T. I. Fossen, *Handbook of Marine Craft Hydrodynamics and Motion Control*. Wiley, 2011.

[7] J. Bjørnø, *Thruster-Assisted Position Mooring of C/S Inocean Cat I Drillship*. Master thesis, Norwegian University of Science and Technology, Trondheim, Norway, 2016.

[8] J. E. Refsnes, *Nonlinear Model-Based Control of Slender Body AUVs*. PhD thesis, Norwegian University of Science and Technology, Trondheim, Norway, 2008.

[9] R. Skjetne, M. E. N. Sørensen, M. Breivik, S. A. T. Værnø, A. H. Brodtkorb, A. J. Sørensen, Ø. K. Kjerstad, V. Calabrò, and B. O. Vinje, "AMOS DP research cruise 2016: Academic full-scale testing of experimental dynamic positioning control algorithms onboard R/V Gunnerus," *in Proceedings of the 36th International Conference on Ocean, Offshore and Arctic Engineering*, 2017.

[10] M. E. N. Sørensen, M. Breivik, and R. Skjetne, "Comparing combinations of linear and nonlinear feedback terms for ship motion control," *submitted to IEEE Transactions on Control Systems Technology*, 2018.

[11] O. N. Lyngstadaas, *Ship Motion Control Concepts Considering Actuator Constraints*. Master thesis, Norwegian University of Science and Technology, Trondheim, Norway, 2018.

[12] "Marine cybernetics laboratory." https://www.ntnu.edu/imt/lab/cybernetics. Accessed: 2018-01-30.

[13] B.-O. H. Eriksen and M. Breivik, *Modeling, Identification and Control of High-Speed ASVs: Theory and Experiments*, pp. 407–431. Sensing and Control for Autonomous Vehicles: Applications to Land, Water and Air Vehicles, Springer International Publishing, 2017.